REPORT DOCUMENTATION PAGE	2	Form Approved OMB NO. 0704-0188

1. REPORT DATE (DD-MM-YYYY)	2. REPORT TYPE	3. DATES COVERED (From - To)
12-06-2014	Ph.D. Dissertation	-

4. TITLE AND SUBTITLE
Novel Devices and Components for THz Systems

5a. CONTRACT NUMBER
W911NF-12-1-0496

5b. GRANT NUMBER

5c. PROGRAM ELEMENT NUMBER
611102

6. AUTHORS
John Middendorf

5d. PROJECT NUMBER

5e. TASK NUMBER

5f. WORK UNIT NUMBER

7. PERFORMING ORGANIZATION NAMES AND ADDRESSES
Wright State University
Wright State University
3640 Colonel Glenn Highway
Dayton, OH 45435 -0001

8. PERFORMING ORGANIZATION REPORT NUMBER

9. SPONSORING/MONITORING AGENCY NAME(S) AND ADDRESS (ES)
U.S. Army Research Office
P.O. Box 12211
Research Triangle Park, NC 27709-2211

10. SPONSOR/MONITOR'S ACRONYM(S)
ARO

11. SPONSOR/MONITOR'S REPORT NUMBER(S)
62602-EL.10

12. DISTRIBUTION AVAILIBILITY STATEMENT
Approved for public release; distribution is unlimited.

13. SUPPLEMENTARY NOTES
The views, opinions and/or findings contained in this report are those of the author(s) and should not contrued as an official Department of the Army position, policy or decision, unless so designated by other documentation.

14. ABSTRACT
Middendorf, John R Ph.D., Engineering Ph.D. program, Wright State University, 2014.
Novel Devices and Components for THz Systems

Since the first demonstration of the generation of terahertz (THz) pulses from photoconductive (PC) antennas, research has pushed toward the development of smaller, cost efficient, and faster THz systems. This dissertation presents the work accomplished in order to realize these more practical terahertz (THz) photoconductive (PC)

15. SUBJECT TERMS
THz, ultrafast extrinsic photoconductivity, structured-surface plasmons, PC switch, polarizer, Fabry-Perot, spectrum analyzer

16. SECURITY CLASSIFICATION OF:			17. LIMITATION OF ABSTRACT	15. NUMBER OF PAGES	19a. NAME OF RESPONSIBLE PERSON
a. REPORT	b. ABSTRACT	c. THIS PAGE			Elliott Brown
UU	UU	UU	UU		19b. TELEPHONE NUMBER 937-775-4903

Novel Devices and Components for THz Systems

ABSTRACT

Middendorf, John R Ph.D., Engineering Ph.D. program, Wright State University, 2014.
Novel Devices and Components for THz Systems

Since the first demonstration of the generation of terahertz (THz) pulses from photoconductive (PC) antennas, research has pushed toward the development of smaller, cost efficient, and faster THz systems. This dissertation presents the work accomplished in order to realize these more practical terahertz (THz) photoconductive (PC) systems.

First, this work will present a novel ErAs:GaAs photoconductive switch used to make a THz source excited by 1550 nm laser pulses. It will be shown that the excitation process taking place in the material relies on extrinsic (rather than intrinsic) photoconductivity. Then, several experiments will be presented that aim to improve the efficiency of the device and further the understanding of the underlying physical mechanisms. The erbium composition of the photoconductive layer will be varied and the effects of these variations on THz generation will be investigated. Then the wavelength of the drive laser used to excite the extrinsic photoconductive mechanism will be varied, while recording the photocurrent responsivity. This wavelength study will be used to find the optimal drive wavelength for maximum THz power. In conclusion, the results of these experiments will show that extrinsic PC THz generation is practical, cost effective, and capable of producing an average THz power of more than 100 μW. Coinciding with this high power level, the bandwidth of this new source was found to be ~350 GHz, corresponding to a photocarrier recombination time of 450 fs. The work presented in this section will provide a path to develop superior THz PC sources that have a higher THz-power-to-cost ratio than the current state of the art.

Photoconductive antennas are mostly used to conduct spectroscopy measurements, either in time domain systems (TDS) or in frequency domain systems (FDS). Currently, both techniques can reach high-frequencies (>1 THz) but struggle to do so while making fast, high-resolution measurements (<2 GHz). In addition, both methods can be time consuming to set up and perform. A superior spectrum analysis technique would greatly facilitate THz application development by making results easier and less expensive to obtain. Therefore, the second part of this dissertation addresses the need for quicker and more precise THz spectrum analysis by demonstrating a new type of THz spectrum analyzer based on a high-speed, tunable, Fabry-Perot interferometer. This new and unique spectrum analyzer reduces the time required to obtain a THz spectrum (a few seconds), while producing a more precise result (<2 GHz resolution). After the presentation of this concept, the various experimental design iterations will be shown, while explaining the improvements gained from each. Then experimental demonstrations of the new spectrum analyzer will be presented, and possible future improvements will bediscussed.

While the Fabry-Perot based spectrum analyzer is an improvement for THz spectroscopy, it can suffer from two issues: mirror reflectivity that changes with frequency, and the inability to easily tune the mirror reflectivity to optimize the system for different applications. These issues make it challenging to obtain an accurate and useful THz spectrum. Therefore the third part of this dissertation is motivated by these problems and presents a solution; the use of structured-surface-plasmon (SSP) enhanced polarizers as Fabry-Perot mirrors. The SSP polarizers used in this work are composed of metal wire-grids with sub-wavelength feature sizes and high metal fill-factors. It will be shown that high fill-factor SSP polarizers can achieve superior THz performance, compared to traditional THz polarizers, with an extinction ratio exceeding 60 dB. With the use of these polarizers as mirrors, the Fabry-Perot can achieve variable mirror reflectivity by changing the polarizer orientation angle. This will allow the spectrum analyzer to compensate for any reflectivity-vs.-frequency changes that occur on the Fabry-Perot mirrors during a spectral scan. Changing the polarizer orientation makes it possible to optimize the spectrum analyzer for different applications; by choosing maximum frequency selectivity (with low power transmission), maximum power transmission (with low frequency selectivity), or somewhere in between. The SSP enhanced THz polarizers are inexpensive, can provide a significant upgrade to the Fabry-Perot spectrum analyzer, and help to achieve a better physical understanding of plasmonic design in the THz field. After the new extrinsic ErAs:GaAs PC sources, Fabry-Perot spectrum analyzer, and SSP polarizers have been presented, this dissertation will finish with a demonstration of a new polarizing Fabry-Perot spectrum analyzer and then suggestions for future research.

NOVEL DEVICES AND COMPONENTS FOR THZ SYSTEMS

A dissertation submitted in partial fulfillment of the
requirements for the degree of
Doctor of Philosophy

By

John R. Middendorf
B.S., Wright State University, 2010

2014

Wright State University

WRIGHT STATE UNIVERSITY

GRADUATE SCHOOL

April 25, 2014

I HEREBY RECOMMEND THAT THE DISSERTATION PREPARED UNDER MY SUPERVISION BY John M. Middendorf, ENTITLED Novel Devices and Components for THz Systems BE ACCEPTABLE IN PARTIAL FULFILLMENT OF THE REQUIREMENTS FOR THE DEGREE OF Doctor of Philosophy.

Elliott Brown, Ph.D.
Dissertation Director

Ramana Grandhi, Ph.D.
Director, Ph.D. in Engineering Program

Robert E. W. Fyffe, Ph.D.
Vice President of Research and
Dean of the Graduate School

Committee on Final Examination

Elliott Brown, Ph.D.

Douglas Petkie, Ph.D.

Jason Deibel, Ph.D.

Daniel LeMaster, Ph.D.

Julie Jackson, Ph.D.

ABSTRACT

Middendorf, John R Ph.D., Engineering Ph.D. program, Wright State University, 2014.
Novel Devices and Components for THz Systems

Since the first demonstration of the generation of terahertz (THz) pulses from photoconductive (PC) antennas, research has pushed toward the development of smaller, cost efficient, and faster THz systems. This dissertation presents the work accomplished in order to realize these more practical terahertz (THz) photoconductive (PC) systems.

First, this work will present a novel ErAs:GaAs photoconductive switch used to make a THz source excited by 1550 nm laser pulses. It will be shown that the excitation process taking place in the material relies on extrinsic (rather than intrinsic) photoconductivity. Then, several experiments will be presented that aim to improve the efficiency of the device and further the understanding of the underlying physical mechanisms. The erbium composition of the photoconductive layer will be varied and the effects of these variations on THz generation will be investigated. Then the wavelength of the drive laser used to excite the extrinsic photoconductive mechanism will be varied, while recording the photocurrent responsivity. This wavelength study will be used to find the optimal drive wavelength for maximum THz power. In conclusion, the results of these experiments will show that extrinsic PC THz generation is practical,

cost effective, and capable of producing an average THz power of more than 100 μW. Coinciding with this high power level, the bandwidth of this new source was found to be ~350 GHz, corresponding to a photocarrier recombination time of 450 fs. The work presented in this section will provide a path to develop superior THz PC sources that have a higher THz-power-to-cost ratio than the current state of the art.

Photoconductive antennas are mostly used to conduct spectroscopy measurements, either in time domain systems (TDS) or in frequency domain systems (FDS). Currently, both techniques can reach high-frequencies (>1 THz) but struggle to do so while making fast, high-resolution measurements (<2 GHz). In addition, both methods can be time consuming to set up and perform. A superior spectrum analysis technique would greatly facilitate THz application development by making results easier and less expensive to obtain. Therefore, the second part of this dissertation addresses the need for quicker and more precise THz spectrum analysis by demonstrating a new type of THz spectrum analyzer based on a high-speed, tunable, Fabry-Perot interferometer. This new and unique spectrum analyzer reduces the time required to obtain a THz spectrum (a few seconds), while producing a more precise result (<2 GHz resolution). After the presentation of this concept, the various experimental design iterations will be shown, while explaining the improvements gained from each. Then experimental demonstrations of the new spectrum analyzer will be presented, and possible future improvements will be discussed.

While the Fabry-Perot based spectrum analyzer is an improvement for THz spectroscopy, it can suffer from two issues: mirror reflectivity that changes with

frequency, and the inability to easily tune the mirror reflectivity to optimize the system for different applications. These issues make it challenging to obtain an accurate and useful THz spectrum. Therefore the third part of this dissertation is motivated by these problems and presents a solution; the use of structured-surface-plasmon (SSP) enhanced polarizers as Fabry-Perot mirrors. The SSP polarizers used in this work are composed of metal wire-grids with sub-wavelength feature sizes and high metal fill-factors. It will be shown that high fill-factor SSP polarizers can achieve superior THz performance, compared to traditional THz polarizers, with an extinction ratio exceeding 60 dB. With the use of these polarizers as mirrors, the Fabry-Perot can achieve variable mirror reflectivity by changing the polarizer orientation angle. This will allow the spectrum analyzer to compensate for any reflectivity-vs.-frequency changes that occur on the Fabry-Perot mirrors during a spectral scan. Changing the polarizer orientation makes it possible to optimize the spectrum analyzer for different applications; by choosing maximum frequency selectivity (with low power transmission), maximum power transmission (with low frequency selectivity), or somewhere in between. The SSP enhanced THz polarizers are inexpensive, can provide a significant upgrade to the Fabry-Perot spectrum analyzer, and help to achieve a better physical understanding of plasmonic design in the THz field. After the new extrinsic ErAs:GaAs PC sources, Fabry-Perot spectrum analyzer, and SSP polarizers have been presented, this dissertation will finish with a demonstration of a new polarizing Fabry-Perot spectrum analyzer and then suggestions for future research.

Table of Contents

LIST OF FIGURES

For my Grandmother Rita
She always wanted a doctor in the family

Acknowledgments

I must give my deepest gratitude to the Lord, Jesus Christ, for blessing me with the ability to complete this work. I am very fortunate.

To my parents, Matthew and Barbara Middendorf, thank you for your love, support, and guidance through the years. My siblings, Katie, Matt, and Paul, you have all given me someone to look up to, each in your own way. I have a great number of friends and family members who have also inspired me through the years, and thank you Mr. Steele for stirring my interest in physics. I hope I have made you all proud.

I also want to give my thanks to Dr. Gary Farlow and Dr. Daniel LeMaster. You each took chances on me and believed in me. You provided me with opportunities I probably did not deserve. I could not have done this without that help.

My advisor, Dr. Elliott Brown, also deserves a great deal of gratitude. He has taught me more than I could have imagined. Thank you Dr. Brown for teaching me how to be a scientist, and bestowing so much time and knowledge upon me.

To my fellow graduate students, John Cetnar, Jack Owsley, and Leamon Viveros, thank you for your friendship and all of the fruitful discussions we have had. I also am grateful for Dr. Matthieu Martin who was almost like a second advisor, and also a great friend. I also want to thank my other committee members for helping me through this process: Drs. Jason Deibel, Doug Petkie, and Julie Jackson

Finally, I want to thank my wonderful girlfriend, Yen Ngo. You have always maintained a certain cheerfulness that made this process so much easier. Thank you for all of your encouragement. This is for you, and for our future.

1. INTRODUCTION

This work was done with the purpose of improving terahertz (THz) generation and control capabilities for THz spectroscopy, through the development of more practical photoconductive THz sources and novel components.

THz spectroscopy has recently received a tremendous amount of attention for security applications because of the unique ability to measure spectral signatures of targets, such as illicit drugs and explosives [7], [8], concealed by opaque materials such as common plastics used in suitcases and other containers [9], [10]. The ability to propagate through visibly opaque materials is a trait shared with radio-frequency systems, and the ability to measure spectral signatures is a trait shared with infrared systems. In this way THz radiation essentially shares beneficial aspects of the two electromagnetic regions on either side of it. However there are significant challenges presented with THz systems, chiefly related to producing and measuring THz radiation with cost effective, fast, and affordable systems. This dissertation was completed to meet this challenge.

The work done for this dissertation starts with a brief introduction to THz systems, namely what a THz system comprises. Then, THz spectroscopy will be introduced to build some familiarity with this application. The challenges that are present in THz systems will then be introduced so that the importance of this work will be obvious. The first novel device will then be presented, a new broadband pulsed THz

source that produces large amounts of THz power, while being activated by a 1550 nm pulsed laser. Several experiments will then be described that were done to thoroughly characterize the performance of the new source, improve the physical understanding of how it works, and provide a path for future improvements.

The new THz source was discovered during the development of a novel THz spectrum analyzer and the measurements performed on this source highlighted the need for this new system. After the presentation of the new THz source, the spectrum analyzer concept will be introduced which is based on a Fabry-Perot interferometer. It will be shown to be easy to construct and use, while also proving capable of taking high-speed and high resolution THz measurements. The spectrum analyzer theory, design iterations, software, and initial measurements will be discussed as well.

As part of the design of the new spectrum analyzer, surface-plasmon-like techniques were utilized and improved upon for controlling and routing THz radiation. The so-called structured-surface-plasmon techniques were applied to a substrate-based linear THz polarizer, and eventually to the new spectrum analyzer. During this procedure, the performance of the THz linear polarizer was greatly enhanced compared to conventional, free standing wire-grid polarizers. This was shown through characterization of the polarizer performance. Finally, the new enhanced polarizers were used in the new Fabry-Perot spectrum analyzer design, and the first proof-of-concept measurements were taken on the new broadband 1550-nm-driven THz sources.

1.1. What is a THz system?

In 1886, using a simple spark gap, Heinrich Hertz successfully completed the first transmission of a free-space electromagnetic signal. This feat triggered an explosion in research and development for "wireless" systems and today electromagnetic systems (such as the cell phone) are essential in nearly every aspect of life. Early systems were very low in frequency. For example, Hertz's breakthrough system operated around 75 MHz (4 m wavelength) and many common frequency bands (such as AM radio) have frequencies in the kHz. In later decades, "wireless" technology advanced considerably and the frequencies of radio systems began to increase. In the 1940s, systems reached up to 3000 MHz using simple wire based antennas [11], and today more complex solid-state microwave sources exist as high in frequency as 100 GHz (3 mm wavelength). Some techniques have even been developed to achieve higher frequencies (Gunn oscillators, IMPATT diodes, Gyrotrons, and others), but 100 GHz represents a challenging barrier on what can be achieved with solid-state oscillating electronic sources, because of speed limitations present in electronic circuits [12].

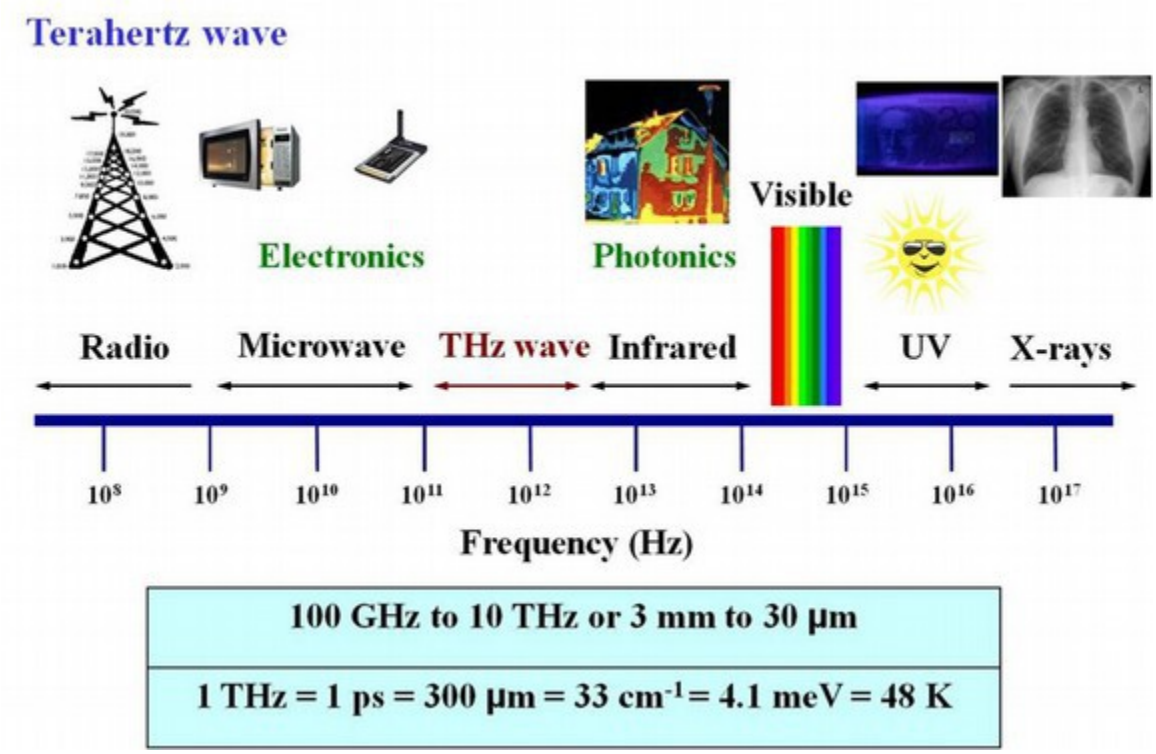

Figure 1. The electromagnetic spectrum. Shown here is the THz band that is defined by the upper and lower limits of the microwave and infrared regions.

In parallel to radio and microwaves, another part of the electromagnetic spectrum that saw rapid growth and development was the optical spectrum. In 1873, prior to Hertz's work, James Clerk Maxwell published the defining set of equations that govern electromagnetic radiation, and he proved that visible light was a part of the electromagnetic spectrum. The frequencies that make up the visible light spectrum (430-750 THz) are much higher than radio- and micro-waves, and light waves tend to be generated with very different techniques, including thermal blackbody radiation (the sun, halogen light bulbs) and stimulated or spontaneous photon emission (lasers, LEDs) [13], [14]. Optical technologies advanced quickly, going from simple black and white photography to advanced camera systems that could see light invisible to the human eye (such as infrared and ultra-violet light). Optical technologies continued to evolve and

eventually the low-frequency limits of optical systems were realized. Due to a drop-off in black-body radiative emission, poor atmospheric transmission, and difficulty of detection, the lower limit of the optical spectrum (known as the far-infrared) is about 10 THz. This low-frequency limit, combined with the RF system high-frequency limits, define boundaries of the THz region (Fig. 1). The THz spectrum, or the "THz gap", can therefore be defined as the electromagnetic spectral region from approximately 100 to 10000 GHz.

With this explanation in place, a THz system can now be broadly defined as a system or set of components that detects, controls, and (possibly) produces electromagnetic radiation in the THz gap. There are two primary classifications of a THz system, active (Fig. 2(a)) and passive (Fig. 2(b)). An active THz system is simply one in which the THz radiation being controlled and detected is also produced by the system, while a passive THz system receives its THz radiation from some other source. Passive THz systems are used primarily in astronomy, as there is usually insufficient background THz in the earth's atmosphere for passive THz systems; a stark contrast to infrared radiation which is plentiful in the earth's atmosphere. The main focus of this work was the development of sources and devices intended for use in active THz systems used for practical terrestrial applications.

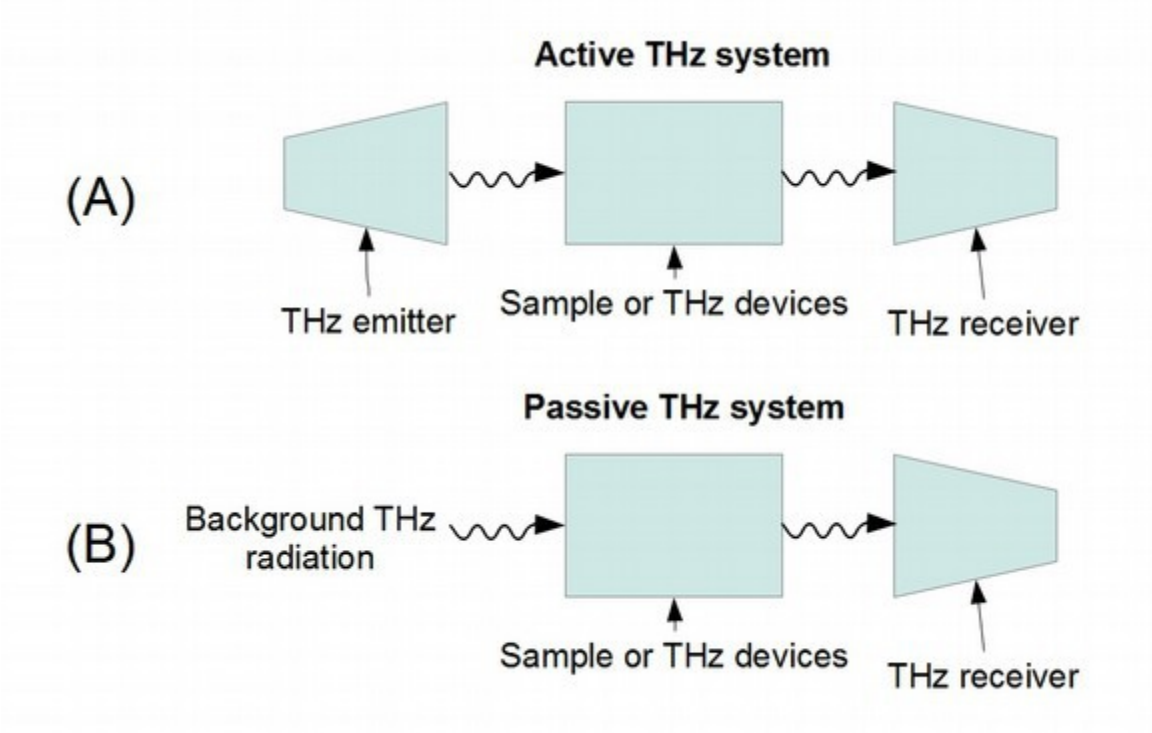

Figure 2. (A) A simple active THz system. (B) A simple Passive THz system. In both system types the Sample or THz devices are optional components.

1.2. THz Spectroscopy – the motivation

The unique attributes present in THz radiation, briefly introduced in the previous section, allow for a diverse and exciting set of applications that are in high demand. One of the most popular applications to date is the imaging of concealed objects [10], [15]–[18]. Similarly, imaging with THz radiation has also found uses in structural analysis, food quality analysis [10], [19], [20], and biomedical sensing applications [21]–[24]. Another THz application receiving much attention is the identification of high-interest targets (such as illicit drugs or explosives) using spectral signatures [7], [8], [24]–[26]. THz spectroscopy has a unique advantage over imaging techniques because rather than just creating an image of a concealed object, the spectral signatures collected from

spectroscopy allow a system to uniquely identify what the object is as well. By comparing the spectral absorption signatures of a scanned target to a database of known signatures, targets can be identified. An example of such a THz signature is shown in Fig 3 [27].

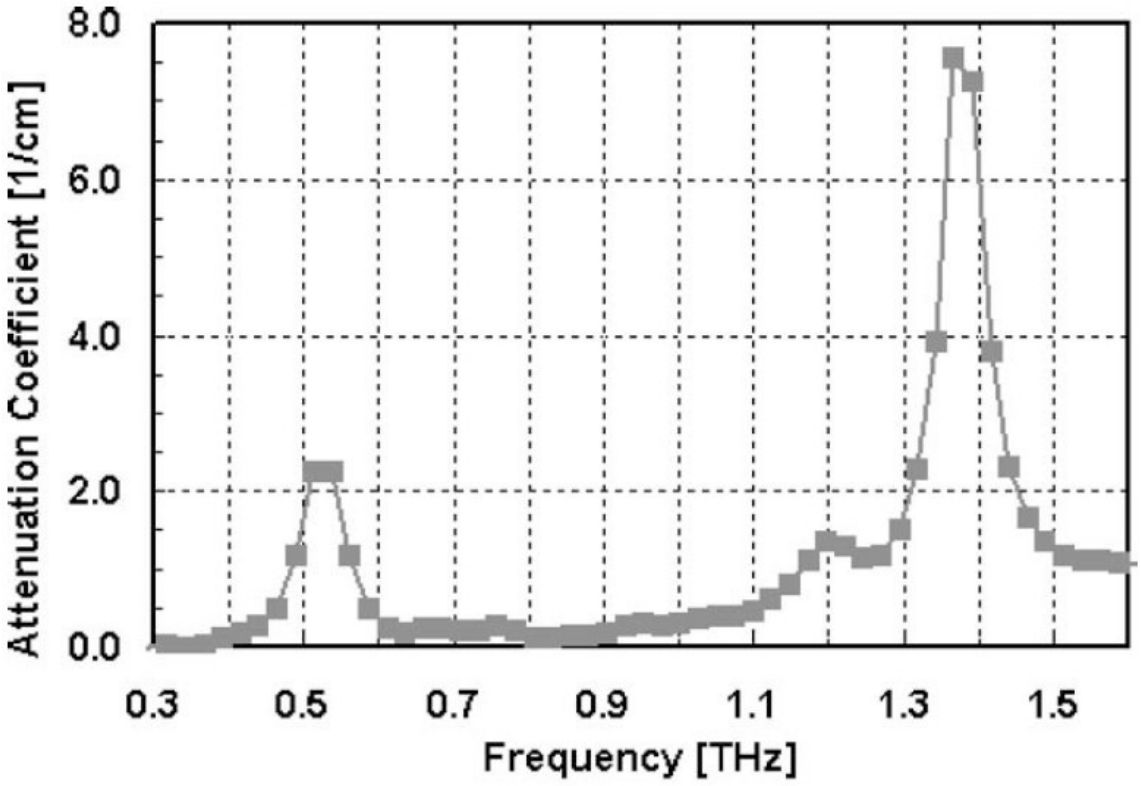

Figure 3: Example THz spectral signatures. The sharp spikes in absorption here are uniquely associated with transmission through alpha-lactose monohydrate [27].

Recent years have brought a great deal of research into spectroscopy for security and biomedical purposes as well [7], [8]. Yet, THz spectroscopy still hasn't seen widespread use in industry, despite the abilities described here. This is because of the lack of practical spectroscopy systems. The major problem with THz spectroscopy systems is that most are currently designed for use in transmission mode. This means

that a sample or object must be carefully extracted and placed inside of the system, which for many real world applications (such as security scanning in an airport) isn't practical. For example, if an explosive, say TNT [28], is concealed underneath a persons clothing it can not be detected by a transmission system. THz radiation can not propagate through water, and hence the human body. So, the only way to detect the TNT package would be using a *reflective* spectroscopy system. However in order make a reflective spectroscopy system several challenges must be overcome. These challenges include reflective signature identification (reflective signatures will have a different profile than transmissive ones), creating enough THz power for stand-off detection (power is at a premium in the THz region, so stand-off distance must be small), and developing a spectrum analyzer that can be easily used in reflection.

The work done for this dissertation is focused on solving these problems, particularly improving high-power THz source technology and developing a better spectroscopy system that can be easily used in reflection mode. But while reflective THz spectroscopy serves as the primary motivation of this dissertation, the components developed and demonstrated will be useful for transmission mode spectroscopy and other applications as well.

2. Novel THz photoconductive sources

THz spectroscopy relies heavily on photoconductive (PC) THz sources because of their ability to radiate over very large frequency ranges (0.1 to ~6 THz). Other types of THz sources (such as very high-frequency RF sources and quantum-cascade-lasers) can not achieve comparable bandwidths [29], [30]. Consequently, as the push for better THz technology continues, much of it focuses on PC sources. There are two primary types of PC THz sources: the photoconductive switch (PC switch) and the photoconductive mixer (photomixer). PC switches and photomixers are operationally very different devices, despite having a very similar appearance. Photomixers are coherent, continuous-wave (CW), single (tunable) frequency electro-optic THz sources activated by the optical heterodyne conversion of two CW lasers [31]. While PC switches (sometimes called Auston switches) are pulsed, broadband electro-optic THz sources [32], [33]. The photomixer is commonly used in frequency-domain spectroscopy applications, where spectral intensity data is recorded as the frequency is swept. PC switches, alternatively, are more commonly used in the THz field because they are ideal for use in time-domain spectroscopy (TDS) and imaging applications; TDS systems are very popular because they can collect data very quickly (a few seconds), and PC switches are better for imaging because they produce more total THz power [21], [22]. The new spectroscopy technique described in Chapters III and IV relies on the PC switch, so the focus of the present Chapter will be the PC switch, but it is worth mentioning that the advances

presented in this chapter may be applied to photomixers as well (see page 51).

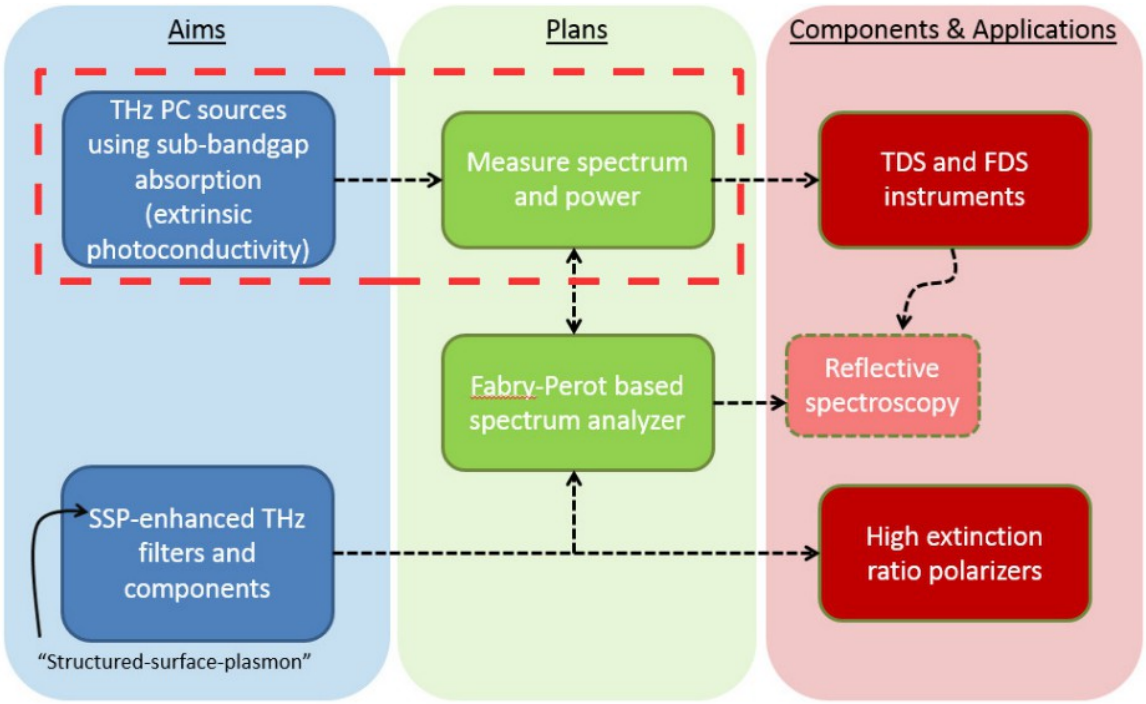

Figure 4: Research plan for this work. Chapter II covers an exciting new discovery: an extrinsic photoconductive switch, that could have a large impact on the field of THz spectroscopy.

The dashed box shown in Fig. 4 is a visual illustration of what this chapter will cover. First there will be a discussion of PC switch basics, how they operate, and the current state of the art. Next a new and promising technique for generating THz radiation with PC switches will be introduced that uses ultrafast extrinsic photoconductivity. This new source takes advantage of previously unknown capabilities of a common ultra-fast semiconductor. After the new THz source is introduced, experiments will be shown that were conducted to study, understand, and possibly improve the new source. The results from these experiments will be shown, discussed, and a future path for research on the new extrinsic PC switch will be presented.

2.1. Photoconductive switch fundamentals

The PC switch arose from a simple-but-difficult problem: switching an antenna between on and off states on the sub-picosecond time scale (necessary to achieve high-frequency, high power pulses). In the past, room-temperature non-optically driven electronic switching methods were not able to realize switching speeds on the sub-picosecond scale [34]. This deficiency in switching capabilities from non-optically driven systems is directly cited as the motivation for the invention of the first PC switch [33], [34], where at that time the best semiconductor plasma based (non-optical) switches worked on the nanosecond scale. Today, sub-picosecond switching speeds are still a tremendous challenge for non-optically driven, pulsed sources, especially as the push for higher frequency, higher power THz sources continues. PC switches still possess the greatest ability to produce short, sub-picosecond electromagnetic pulses [7].

The reason such short electromagnetic pulses are desired lies in the innate dependence of frequency-bandwidth on time-domain pulse width. It is well known that the shorter an electromagnetic pulse is in the time-domain (s), the greater the frequency (1/s) bandwidth (the Fourier transform of a Dirac-delta function is a classic example). So determining the temporal pulse length necessary for THz operation is easily done by taking the inverse of the desired bandwidth ($\tau = 1/\omega$). For example, to achieve a 3-dB frequency-bandwidth of 100 GHz the temporal pulse width (typically FWHM) emitted from the PC switch must be 1.59 ps, and for 1 THz bandwidth the pulse width must be 0.159 ps. PC switches are capable of achieving these extremely short pulse widths because they are actuated by extremely short optical laser pulses. Mode-locked-(pulsed)-

laser (MLL) technology has advanced to the point where sub-fs optical pulses can be created [35]. Therefore, laser technology has surpassed the pulse width needs of THz PC switches, and ultra-fast (sub-picosecond scale) fiber-optic lasers emitting 0.1 ps pulses are readily available [36]. With the availability of such ultra-fast lasers, the limit on PC switch bandwidth (and power) lies elsewhere, in the antenna design and semiconductor choice. However, before explaining how the antenna and semiconductor affect PC switch performance, it is important to have a basic understanding of how a PC switch operates.

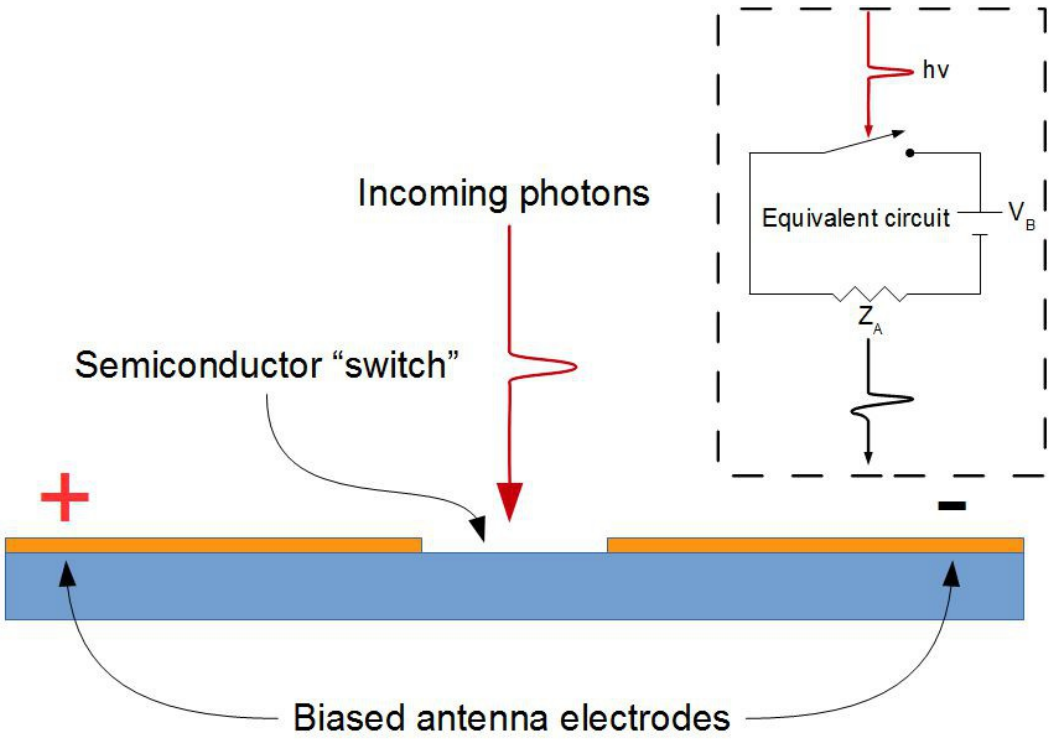

Figure 5: Simple PC switch diagram. The antenna arms are biased so that when incoming photons switch the semiconductor to a conducting state current can flow through the antenna.

In concept, PC switches are simple electro-optical RF-to-THz devices, a variant of which was first devised in the 1970s by Johnson and Auston [33]. There are typically only two primary physical components: an antenna and an ultra-fast photoconductor. A

cross-sectional-view of a simple PC switch is shown in Fig 5. The antenna in a PC switch has two arms or electrodes (Fig. 7 shows a small selection of the antenna designs that have been developed). The two antenna arms have a DC bias applied and form an open circuit with the ultra-fast semiconductor "switch" at the center of the arms, in the absence of laser power. However, when a pulse of high power photons from a MLL are incident, they convert the semiconductor into a conductor temporarily, and a pulse of current flows through the antenna[1]. This results in a pulse of radiation that is emitted from the antenna and as explained previously, the frequency bandwidth of that pulse is defined by the temporal width of the pulse. A simple experimental block diagram of a PC switch setup can be seen in figure 6.

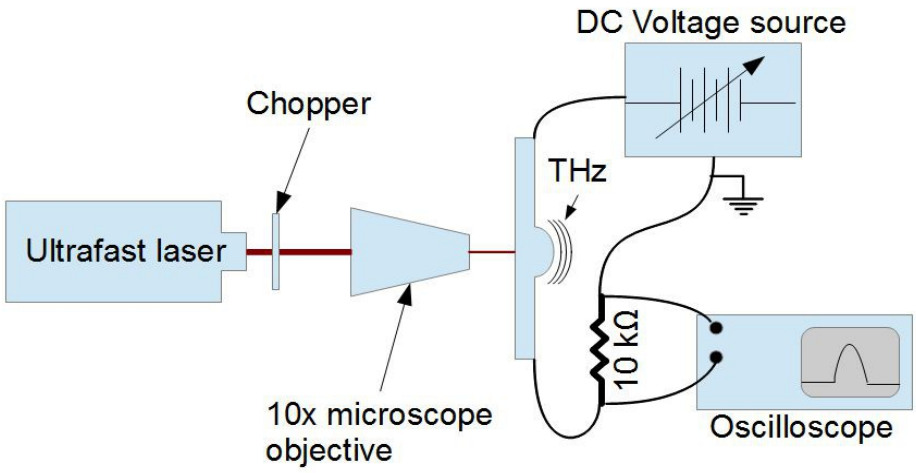

Figure 6: A basic PC switch setup. The ultrafast laser is chopped so the power can be easily detected, then focused onto the PC switch. The PC switch is biased with a DC source. When the laser pulse hits the PC switch THz power is emitted. An oscilloscope is used to monitor current flow in the antenna.

1 It is important to note that the photon energy of the laser must be larger than the bandgap of the photoconductor. For example, with GaAs photoconductors 800 nm photons are used (E = 1.55 eV and GaAs E_g = 1.42 eV).

2.1.1. Photoconductive switch antennas

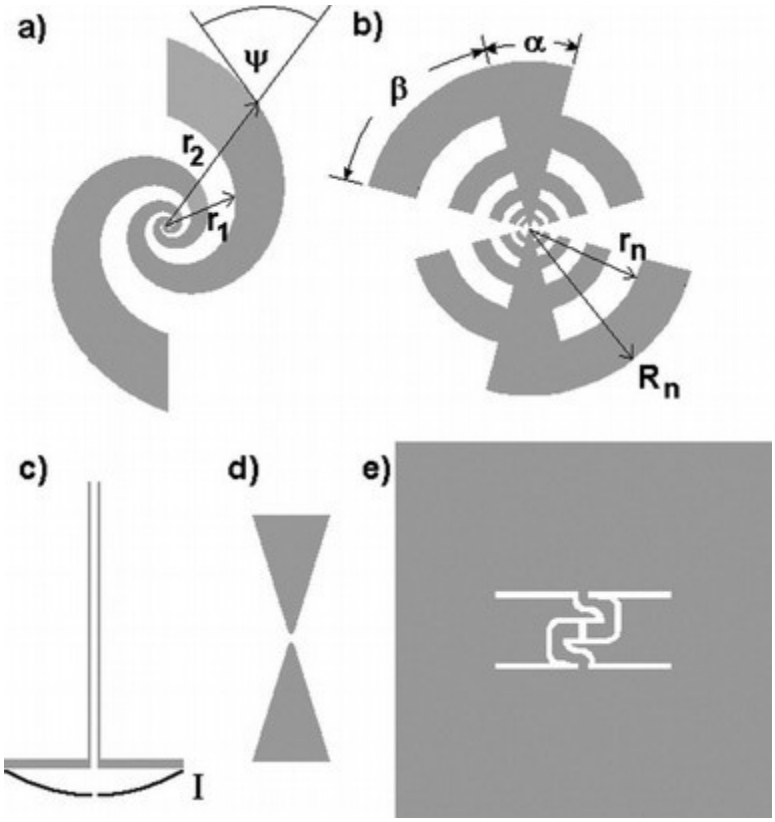

Figure 7: Common antennas designs used in PC switches (overhead view). Spiral antennas (a) are often preferred because of high power, circularly polarizer output [60].

The antenna chosen to radiate the electromagnetic pulse generated by the PC switch is an important design consideration, mostly because of the effect the antenna has on total output power. But while the antenna design does not have a large effect on the temporal pulse width, there is still some effect on the THz bandwidth. This is because the antenna must have feature sizes suitable for coupling frequencies across the THz spectrum [37]. Because of this many antennas, such as those in figure 7 (a, b, d), have tapered arms. The larger features have higher coupling efficiency for low frequencies (~100 GHz), while the small features in the center of the antennas couple the higher THz

frequencies more effectively. Simpler antennas such as dipoles (Fig. 7 (c)) will still work for PC switch use, but their bandwidth will be diminished by their resonant nature.

Another antenna design consideration is directivity. Since THz power is always at a premium, a high gain, frequency independent antenna design is also desirable. Designs such as the dipole and bow-tie are famous for their low directivity and strongly frequency dependent radiation pattern [11], which further reduces their usefulness. Alternatively, self-complimentary, spiral-based designs have higher directivity and the beam pattern is completely frequency independent. With these antenna designs most radiation propagates perpendicularly to the plane of the antenna, and with the considerably higher dielectric constant of GaAs (12.8) (compared to air), most of the THz radiation from these antennas is coupled into the GaAs (rather than the air) side of the antenna. The high dielectric constant of GaAs creates a very low critical angle for total internal reflection (16.7^{o}), so to couple the radiation out of the GaAs substrate, hemispherical Silicon lenses are often abutted to the substrate. The Silicon dielectric constant is closely matched to GaAs, allowing the radiation to effectively couple into the silicon lens, and then into free-space. Directivity of nearly 30 dB has been reported in such spiral-based antenna designs [37].

$$P = \eta I^2 R_A(f) \tag{1}$$

As stated above, total THz output power is the larger issue that drives antenna choice for PC switches. Shown in Eq. 1 is THz power output vs. photocurrent in the antenna where η is the coupling efficiency (and is a number between 0 and 1), I is photocurrent, and $R_A(f)$ is the antenna radiation resistance [37]. Coupling efficiency is

simply a ratio of absorbed photons vs. incident photons, so this factor is antenna independent. So only one variable in this equation is primarily determined by the antenna design: R_A. As mentioned in the bandwidth discussion, an antenna should be chosen so that R_A remains high across the THz spectrum of interest.

Designs such as the dipole (Fig. 7 (c)) have R_A values that vary greatly across the spectrum. Because of this, R_A can be lower than 10 Ω away from the center frequency [11]. The bow-tie (or triangular dipole) antenna is less frequency dependent than the dipole but still has limited power because of lower R_A. However, spiral or log-spiral (Fig. 7 (a)), and log-periodic (Fig. 7 (b)) antennas are designed with special symmetry properties that allow them to have nearly frequency independent R_A. The spiral and log-periodic designs also have the benefit of being self-complementary designs which allows R_A to approach high and constant value. R_A in self-complementary designs approaches the modified form of Booker's relation for air-to-dielectric interfaces (Eq. 2) where η_o is the characteristic impedance of free space and ε_{eff} is the effective permitivitty of the PC switch semiconductor substrate (typically GaAs). Using this relation R_A reaches a flat value 72 Ω for most self-complimentary THz PC switches [6], [11], [37], [38].

$$R_A = 2\eta_o\sqrt{(\epsilon_{eff})} \tag{2}$$

Spiral, log-spiral, and log-periodic antennas have represented the state-of-the-art in THz PC switch antenna design for many years because of their large bandwidth and frequency independent radiation pattern, but a newer antenna type has been proven capable of producing more powerful THz signals in recent years, particularly between 0.1 and 1 THz [6], [37], [38]. This new antenna can be seen in Fig. 8 and is a self-

complementary square-spiral antenna. In appearance, this design is similar to the spiral design, but the key difference is that each straight section of the square spiral acts as it's own dipole. Each dipole section, from the center out, is designed for a progressively longer wavelength and because of this the square spiral has much broader bandwidth than a regular dipole antenna. This design is advantageous because dipoles have a much greater R_A than the self-complementary set of antennas. However dipole antennas are normally hindered by a very small bandwidth – R_A falls off quite quickly away from the dipole center frequency [11]. So by effectively having many different sized dipoles (with different center frequencies) this design keeps a much higher R_A across much of the THz spectrum, fluctuating between 100 and 250 Ω [37]. This level of resistance is very convenient, aside from being a higher value than other self-complementary designs, it also more closely matches the resistance of the photoconductive switch in the middle of the antenna (when the switch is turned on). Therefore, the square spiral design also benefits from lower impedance mismatch losses between the antenna and PC switch and the self-complementary nature of this design also maintains a frequency-independent radiation pattern. With this antenna design a PC switch was fabricated and tested that is currently the worlds most powerful, producing 1.6 mW of broadband, average THz power [7].

The square spiral antenna is arguably the state-of-the art at this moment in time but it is worth mentioning that other techniques may enhance the performance even further. Excellent research is being conducted on enhancing PC switch performance by increasing laser-to-THz power coupling efficiency with plasmonics [39]. However at

the present time, the antenna design in figure 8 is more well known and readily available, so this design was chosen for the present work. In any case, the advances in PC switch technology presented in this dissertation are most related to the ultrafast semiconductor material used for the switch, the role of which is explained in the following section.

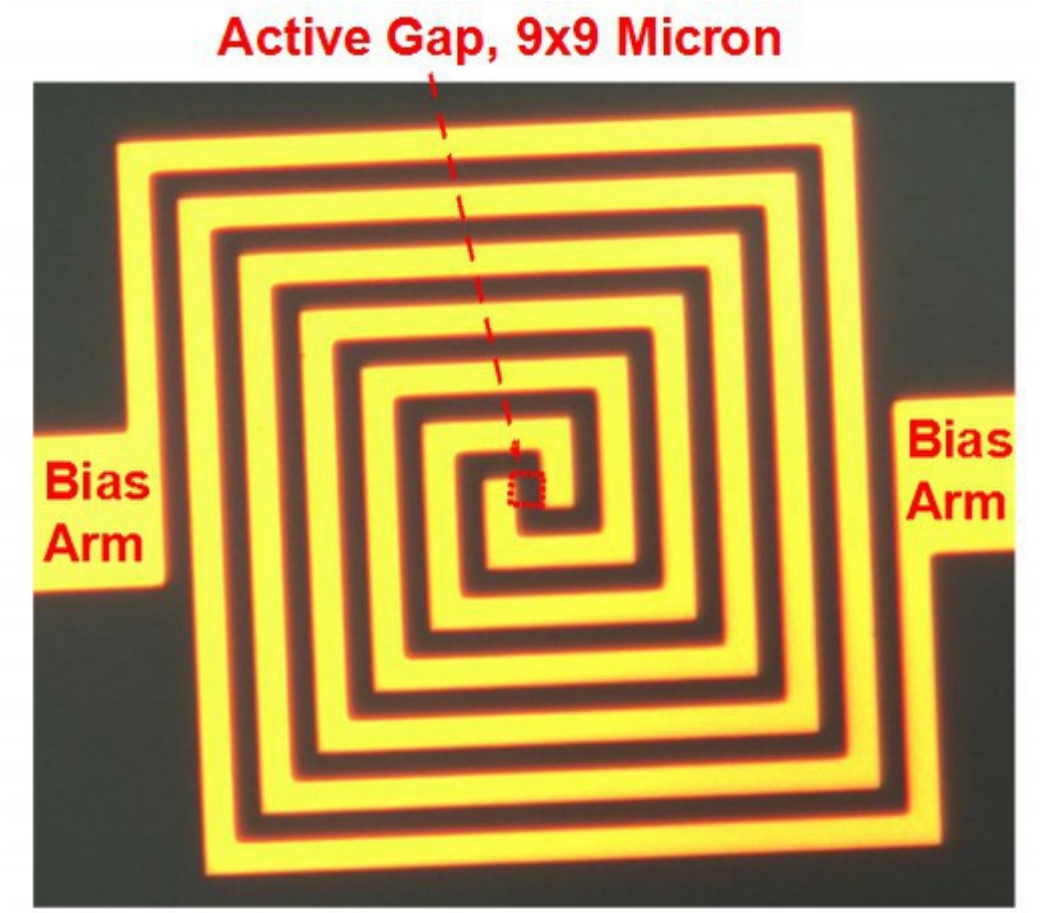

Figure 8: The square spiral antenna, the state of the art in THz photo-antenna design. The highest ever THz power levels (up to 1.6 mW) have been measured from PC switches coupled to this antenna. The active gap is the point at which the laser photons are focused, this gap is the switch.

2.1.2. Photoconductive switch materials: Ultrafast photoconductor properties

The most important aspect of a PC switch is undoubtedly the ultrafast photoconductor. This aspect plays the largest role in defining the PC switch's bandwidth and output power capabilities. As a consequence, PC device (PC switches, photomixers, and photodiodes) research is often focused around creating new or superior photoconductive materials. To create a high-power, broadband THz PC switch, it is necessary to have a photoconductor that is highly conductive in its "on" state, reliably supports high power levels, and is also capable of switching off very quickly to maximize bandwidth (through shorter pulse width). In order to choose or create a photoconductor that possesses these attributes, there are several semiconductor properties to keep track of. The most critical of these properties include the photocarrier lifetime (in picoseconds), photocarrier mobility (cm^2/V-s), dark resistivity (Ω-cm), and the critical breakdown field E_B (V/cm) [2]. The drive wavelength (λ) is also an important consideration because it can greatly affect the cost of generating THz power with a PC switch [40]. The next several pages will describe these properties, so if the reader already understands them, skip to page 27.

Photo-carrier lifetime (often called recombination or relaxation time) is the chief factor in determining the PC switch bandwidth. Photo-carrier lifetime is the amount of time required for the photoconductor to return from a conducting state to a non-conducting state, which naturally happens after the laser pulse has ended. This is because excited electrons (or holes) must relax from the conduction band (or valence band) back into the valence band (or conduction band). So if the lifetime is short, the pulse width of the THz signal can also be short (and the bandwidth high). Another way of illustrating

the effect of photo-carrier lifetime is by spectral analysis; the THz power spectrum from a PC switch typically fits the single-pole Lorentzian function shown in Eq. 3 where τ is lifetime, A is a constant, and f is frequency [5]. Using this equation it is evident that a smaller τ will lead to higher power regardless of frequency.

$$S(f) = A[1 + (2\pi f \tau)^2]^{-1} \quad (3)$$

The carrier mobility is an important semiconductor property because it directly affects the on-resistance and therefore the output power. Mobility can be simply described as the ease with which carriers (electrons or holes) can drift in a material [2], but the importance of having high mobility in the photoconductor is best shown by semiconductor physics. For example, an expression for current from Ohms law is show in Eq. 4, which is dependent on the conductivity (σ), Electric field in some direction x (E_x), and the area over which the current is flowing (A). Also shown in this equation is an expression for the on-state conductivity that is dependent on the electron (μ_n) or hole (μ_p) mobility, the photocarrier density created by the laser pulse (Δn), the charge per carrier (q), and the dark conductivity (σ_o). From this expression, it is obvious that the mobility has a direct affect on the on-state conductivity and thus the current [1], [2]. Applying this information to equation 1, the THz power transmitted from the antenna, one can see the quadratic[2] effect electron or hole mobility (and electric field, described later) has on transmitted THz power[3].

2 The actual increase is slightly less than quadratic at high E_x values due to current saturation effects [1].

3 The area (A) of the photoconductive gap also has a quadratic effect on total THz power, however usually A is kept small to maintain a low RC time constant in the PC switch circuit (C is directly related to A).

$$I_x = \sigma E_x A \; where \; \sigma = \sigma_o + q \Delta n (\mu_e + \mu_p) \quad (4)$$

Like mobility, it is also important to have a high dark resistivity (ρ_o) and critical breakdown field (E_B) in the photoconductive material. High dark resistivity is useful because it lessens the amount of leakage current (or "dark current") in the photoconductive layer during the off-state, which in turn lessens the effects of Joule heating (Joule heating is known to contribute to device failure). A lower dark current level also enables a more powerful THz pulse because there will be a greater difference between peak pulse current in the on state and the DC baseline current in the off state. Photoconductive materials with high dark resistivity also tend to have high E_B. This is an important fact because, as alluded to in the previous paragraph, the THz power from a PC switch scales nearly quadratically with bias voltage [5]. Therefore choosing a photoconductive material with a high E_B allows the PC switch to be used with a higher bias voltage.

Another important consideration is the wavelength of the laser (drive wavelength), which is (usually) entirely dependent on the band-gap of the PC material. Typically ~800 nm lasers are used to drive the current state-of-the-art GaAs-based PC switches, but there is a strong push to create comparable PC switches driven by 1550 nm lasers. 1550 nm lasers are typically much less expensive and more readily available, as are the components used for controlling 1550 nm light (stemming from their widespread use in the fiber-optic telecomm industry) [40]. However this design choice presents a trade-off because previous research has shown that E_B tends to scale super-linearly with band-gap [41]. Therefore materials that have the proper band-gap for 1550 nm photons

suffer from low maximum power output because they must have a low bias voltage, compared to their 800 nm counterparts.

2.1.3. Photoconductive switch materials: State-of-the-art

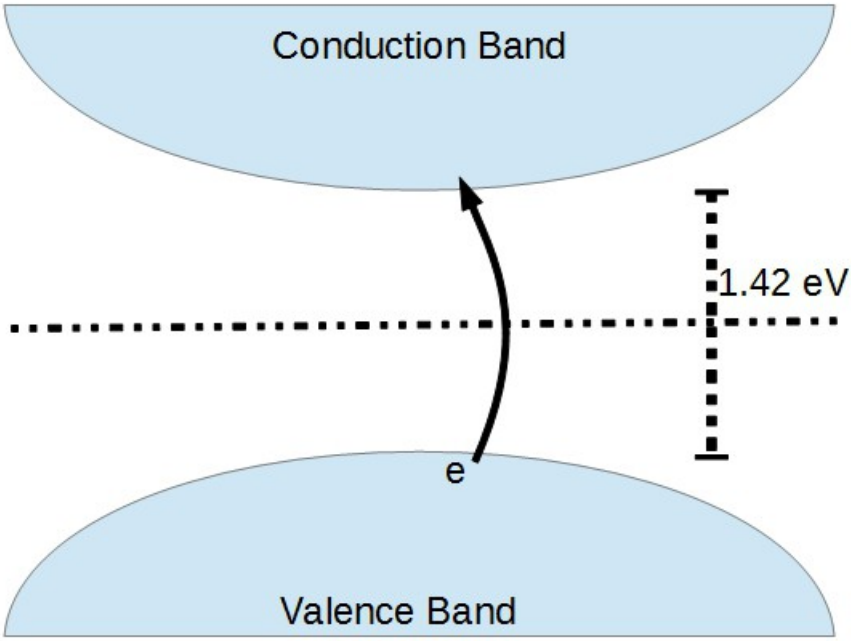

Figure 9: The intrinsic photoconductive process in LT-GaAs or ErAs:GaAs. Incoming photons excite electrons from the valence band into the conduction band, thus creating a conductive state in the semiconductor.

The operation of current state-of-the-art PC switches is based on the simple intrinsic photoconductive process, shown in Figs. 9 and 10. If the incoming photons emitted from the ultrafast laser have more energy than the semiconductor band-gap-energy (photon energy calculated by $E = hc/\lambda$ where h is Planck's constant, c is the speed of light, and λ is the wavelength) then they can transfer their energy to bound electrons in the valence band, exciting them across the bandgap and into the conduction band of the semiconductor. This process causes the PC material to reach a conductive state that will

continue as long as the photons are incident on the semiconductor. When the laser pulse ends carrier excitation stops and the electrons in the conduction band eventually recombine with the holes that were created when they left the valence band (electrons and holes are always created in pairs by the intrinsic process, so holes must be available). For the GaAs band-gap of 1.42 eV, shown in Figs. 9 and 10, the wavelength of light must be shorter than ~876 nm for the photon energy to be high enough to excite an electron across the bandgap and create a conductive state. So for GaAs based PC switches ~800 nm lasers are typically used because this wavelength is readily available in multiple laser types [40], [42].

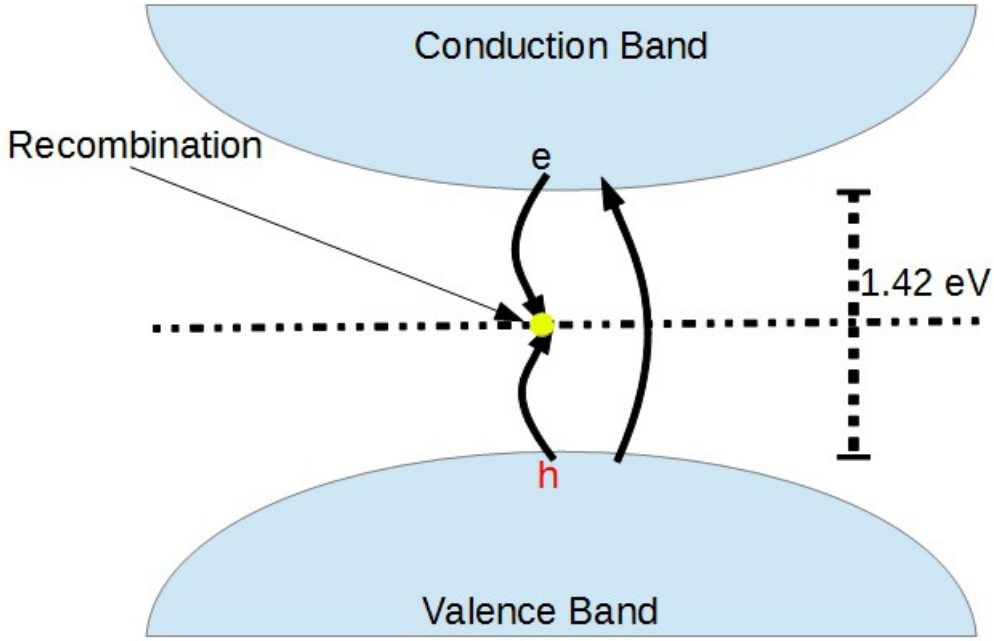

Figure 10: The recombination process that returns a photoconductive material from a conducting state to a non-conducting state. Many ultrafast materials contain impurities or defects in the crytsal lattice, because the impurities act as recombination or donor levels and help decrease carrier lifetime [31], [43], [44].

As explained in the previous section, it is desirable for the electron-hole

recombination process to happen as quickly as possible in a PC switch. This will enable the semiconductor to switch off faster and the THz pulse will be shorter in the time-domain. One of the breakthrough methods of shortening recombination time was deliberately creating PC materials with defects in the crystal structure. Early on this was done by bombarding the material with high-energy ions [43], [44]. These defects (such as atomic interstitials or substitutions) in the crystal lattice create mid-band-gap energy levels that tend to be ultrafast recombination centers for electron-hole pairs (as seen in Fig. 10) [1]. Using materials with such defects (like ion-implanted silicon) substantially decreases carrier lifetime, but they also have a negative effect on carrier-mobility which lowers overall current generation (eq. 4) [31], [43]. Despite the poor current generation capability of these early materials, the thought process behind them lead to one of the major breakthroughs in THz PC materials, low-temperature-grown (with molecular beam epitaxy) Gallium Arsenide (LT-GaAs).

LT-GaAs was first utilized in photoconductive devices in the early 1990s and it was vastly superior to the PC materials that preceded it. Growing GaAs at low-temperature (<200 ^{o}C) created a large number of structural defects (mostly As atoms substituting for Ga atoms, or as metallic As precipitates), similar to what was seen with ion bombardment in previous materials. A very high density of mid-gap energy levels are created from these defects, and thus a high density of ultrafast recombination centers. These allow LT-GaAs to have very short carrier lifetime (~0.27 ps) [31]. In addition there are two key practical differences between LT-GaAs and previously used materials. First, LT-GaAs has considerably higher mobility, partially because GaAs inherently has

higher mobility than silicon [1], [2], [43]. Second, LT-GaAs has a high breakdown field E_B (and dark resistivity) due to it's large bandgap (and high bulk resistivity), 1.42 eV for GaAs vs. 1.1 eV for silicon, 1.35 eV for InP (10^5 Ω-cm). With these advantages LT-GaAs was capable of producing power levels at least ten times greater than other PC materials of the time [44]. This made LT-GaAs the best ultrafast PC THz material when it was introduced, in fact LT-GaAs was so good that it still sees wide-spread use today. Only one other material has surpassed LT-GaAs in THz power generation, erbium doped GaAs (ErAs:GaAs), and consequently ErAs:GaAs represents the current state-of-the-art in PC switch materials [3], [6].

ErAs:GaAs is a GaAs MBE layer grown at normal temperatures, much higher than LT-GaAs (> 500 ºC vs. 200 ºC for LT-GaAs). As the epitaxial layer is grown, it is doped with the rare-earth metal erbium (Er), a process that is described in Refs. [45], [46]. The effect of the Er doping is very similar to what is seen in LT-GaAs; the material has a large number of substitutional impurities (Er replacing Ga) that act as mid-band-gap energy levels, and

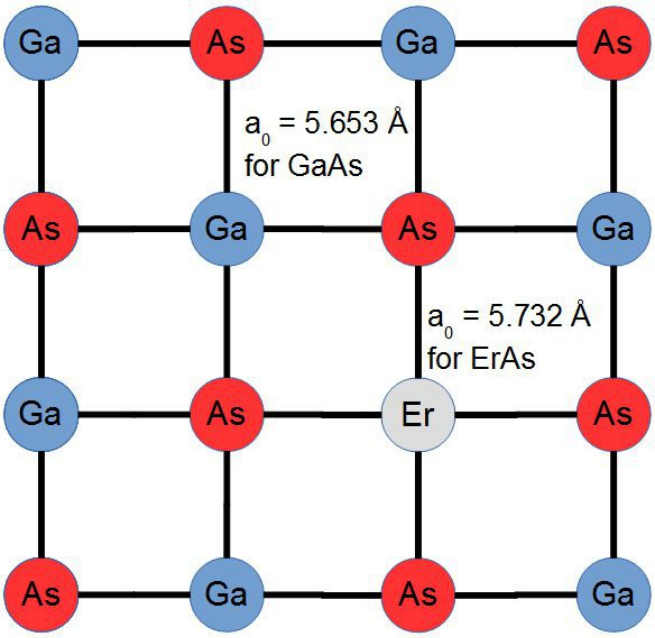

Figure 11: A ErAs particle in the GaAs lattice. Er atoms added to GaAs during growth become substitutional defects because they have a closely matched lattice constant, what little difference there is can be accounted for elastically. Higher mobility values in ErAs:GaAs compared to LT-GaAs have been attributed to the close lattice match shown here.

again, these help shorten carrier lifetime by acting as ultrafast recombination centers. The key difference is that ErAs:GaAs also provides superior mobility; a fact that is attributed to the excellent lattice matching between ErAs sub-lattice and the GaAs sub-lattice. The ErAs and GaAs have lattice constants within 1.5% of each other (shown in Fig. 11). Because of the closely matched lattice constant the Er atoms can be (but don't have to be[4]) almost exclusively arranged as homogenous substitution defects, while causing very little strain in the crystal lattice [45]–[47]. Therefore the physical structure of the crystal lattice is nearly defect-free and excited carriers can drift between atoms with fewer scattering events (therefore increasing the mean-free-time and hence the mobility[5]). The mid-gap energy levels in ErAs:GaAs also have additional advantages that relate to the PC switch advancements made in this dissertation, which is discussed in Chapter II, page 27.

While LT-GaAs and ErAs:GaAs are currently the best materials for THz generation, they usually require the use of 800 nm ultrafast lasers. As mentioned previously, it is desirable to create THz sources that use 1550 nm fiber-optic lasers and components, and progress towards this goal has been steady. So far the physical mechanism used to create 1550 nm PC switches has been the same, cross-gap (intrinsic) photoconductivity. For intrinsic operation at 1550 nm, the ultrafast material must have a

4 ErAs molecules can also be clumped together into nanoparticles or "islands," this is achieved using different parameters during the MBE growing process [2]. However this technique is thought to be inferior because the large nanoparticles have a larger capture cross-section then homogeneously distributed ErAs particles. Following Shockley-Reed-Hall theory, larger capture cross-section slows down recombination time [3].

5 Lattice defects impede electron transport by shortening the mean-free-time, or the average time the carrier travels before running into some particle. A simple mobility equation shows the effect of mean-free-time on mobility: $\mu_n = q\bar{t}/m_n^*$ $\bar{t}$ is the mean-free-time, q is the charge of an electron, and m_n^* is the conductivity effective mass [4].

small band-gap to compensate for the low photon energy (0.80 eV). At the present time the best materials for this task are InGaAs or InGaAsP epitaxial layers on InP substrates. Ultrafast carrier lifetimes have been achieved in these materials with a variety of different methods of implanting metallic nanoparticles or creating deep level lattice defects. Some of the most promising materials include Be-doped LT-InGaAs [48], Fe-implanted InGaAs [49], ErAs:InGaAs [50], Br-irradiated InGaAs [51], Be-doped InGaAs/InAlAs [52], cold-implanted InGaAsP [53], and standard InGaAs with intervening InAlAs layers [54]. All of these materials have a carrier lifetime of 1 ps or less, and many of them have higher mobility than GaAs. However the problem with all of these materials is that they still suffer from low E_B due to their small band-gap [41]. Because of this the DC bias voltage must be considerably lower and power generated (Eq. 1) is significantly lower than what is seen in GaAs based PC switches. So there is still a strong push for a 1550 nm PC switch with power output comparable to 800 nm PC switches. The rest of this chapter is dedicated to an exciting, powerful, and novel method of generating THz power on GaAs PC switches with 1550 nm photons.

2.2. Investigating ErAs:GaAs

Further analysis of semiconductor physics reveals that other photoconductive mechanisms (besides intrinsic) could work for photocurrent generation. Mid-band-gap energy levels (abundantly present in most ultrafast materials), in addition to aiding recombination, can also be used for photo-carrier generation [1], [2], [4]. Usually this type of carrier generation is characteristic of extrinsic photoconductivity (Fig. 12b),

where the carrier transition (hole or electron) is from a mid-gap level to one of the bands (valence or conduction). This current generation process is linear with incident optical power, one photon will excite one carrier, and therefore extrinsic photoconductivity would be characterized by a linear increase in conductivity with laser power. This is shown in Eq. 5, where g is the photoconductive gain, e is the charge of an electron, P is the incident light power, h is Planck's constant, and ν is the light frequency. The reason this photoconductive mechanism could be useful is that less photon energy is needed to excite a carrier from a mid-bandgap energy level, compared to cross-gap photoconductivity. This means that a longer wavelength can be used to generate photocurrent, possibly including 1550 nm. Extrinsic photoconductivity previously had been shown to work for generating high power signals on the 10 ps scale with a semi-insulating-GaAs PC switch and a 1550 nm laser [55], but it had not yet been tried with ErAs:GaAs.

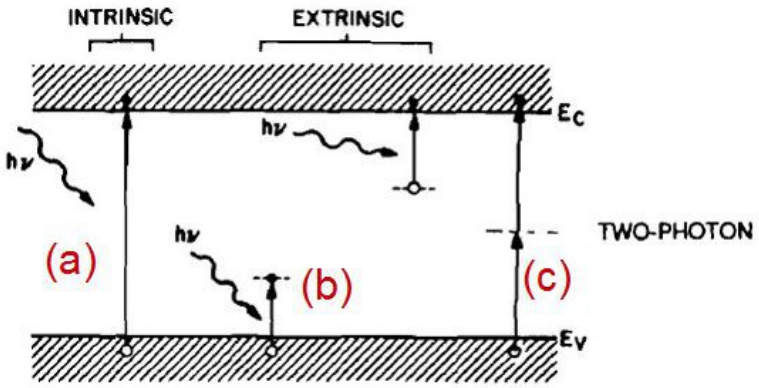

Figure 12: Photoconductive mechanisms. (a) Intrinsic (or cross-gap) photoconductivity. This is traditionally how PC switches are used. (b) Extrinsic photoconductivity. (c) Two-photon photoconductive process. (b) and (c) represent sub-band-gap processes [56].

$$I = \frac{geP}{h\nu} \tag{5}$$

In another study, THz light creation was attempted using a different sub-band-gap photoconductive mechanism: two-photon absorption (TPA) (Fig. 12(c),13) [56]. In this process, the carrier must absorb two photons in immediate succession to gain enough energy for a cross-gap transition. This mechanism is a nonlinear process and requires that the incoming photon energy be near the half band-gap energy level of the photoconductor, as is the case with 1550 nm lasers and GaAs (0.8 eV vs. 0.71 eV). The characteristic behavior of TPA is illustrated by Eqs. 6 and 7, which show the two-photon transition rate from the valence band to the conduction band (6), and the absorption of light intensity at some distance (z) into the semiconductor (7). The Hamiltonians in 6 will be constant, h is Plancks constant, ν is the incoming light frequency, E is energy and c,v, and i correspond to the conduction, valence, and intermediate bands. The equation for W_2 shows that as the photon energy moves away from the center of the bandgap the pump rate should decrease quadratically, so getting

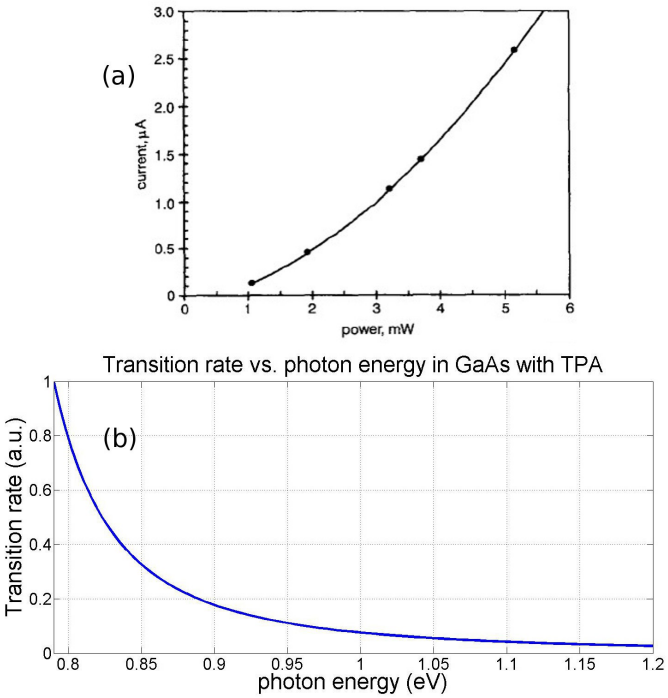

Figure 13: Two-photon absorption (TPA) characteristics. (a) The change in photocurrent with laser intensity [57]. (b) The decrease in pumping rate as photon energy deviates farther from the mid-band-gap.

close to the middle of the bandgap is crucial (Fig. 13(b)). In Eq. 7, the two-photon absorption coefficient (β) is proportional to the incoming light intensity (I). So the photocurrent generation should increase quadratically with intensity, this is exactly what is observed experimentally in Fig. 13(a) [57], [58]. Because it is a nonlinear process two-photon absorption has low quantum efficiency, but it was used to successfully created some THz radiation, but it was impractically weak compared to state-of-the-art 800 nm PC switches [6], [57], [59]. Nevertheless, the benefit of using both 1550 nm laser components and relatively wide-band-gap semiconductors together is still very appealing. 1550 nm components and lasers are relatively inexpensive, while wide-band-gaps can enable much higher THz power levels because of their higher E_B.

$$W_2 = \frac{1}{(2\pi)^2 h} \int \left| \frac{\sum_i \langle \Psi_c | H_{eR} | \Psi_i \rangle \langle \Psi_i | H_{eR} | \Psi_v \rangle}{E_i - E_v - h\nu} \right|^2 \delta(E_c(k) - E_v(k) - 2h\nu) d^3k \tag{6}$$

$$\frac{dI}{dz} = -(\alpha + \beta I) I \tag{7}$$

One material that appeared to meet all requirements for extrinsic photoconductivity, but had not yet been tried, is ErAs:GaAs. As described earlier, this material not only contains a high density of mid-gap energy levels, but the defects that create these energy levels don't disrupt the GaAs lattice greatly. Consequently, ErAs:GaAs is known to have very fast recombination time as well as good mobility. Furthermore, previous research has proven that ErAs:GaAs readily absorbs 1550 nm photons, as well as other sub-band-gap wavelengths (Fig. 14) [60]. So this material

should be an ideal candidate for extrinsic or two-photon photoconductivity.

Figure 14: Sub-band-gap absorption characteristics of ErAs:GaAs. While 1550 nm absorption is low compared to other wavelengths, it is still significant.

2.2.1. Discovery: THz generated with extrinsic photoconductivity in ErAs:GaAs

While conducting the work presented in Chapter III, a new fast-scanning THz spectrum analyzer, a THz PC switch was needed for taking spectral measurements. Originally an 800 nm[6] drive wavelength, ErAs:GaAs PC switch (identical to that in Fig. 8) was to be used for this experiment, but during experimental setup it was discovered that THz power could be generated with an ultrafast 1550 nm fiber-laser[7]. This discovery not only provided a usable PC switch for spectral measurements, but also represented a major breakthrough in THz PC switch technology by finally creating a practical 1550 nm

6 In literature the drive wavelength will often be quoted as 780 nm as well, either works. 800 will always be quoted here for consistency.

7 The results from this study were published in Optics Express [5].

driven PC switch.

The experimental diagram of the PC switch testing can be seen in Fig. 15. From left to right, the 1550 nm fiber-laser was a “Mercury” model erbium-doped-fiber-amplifier (EDFA) from Polaronyx Inc. [40] with a pulse width of ~0.3 ps, maximum average power of 140 mW, and a pulse repetition rate of 49MHz. The laser was output to free-space with a standard fiber-to-free-space coupler and then chopped at 8 Hz for easy THz power and photocurrent measurement. A 10x microscope objective was then used to focus the 1550 nm pulses onto the driving gap of the PC switch. The ErAs:GaAs layer used for this study consisted of a 1.0-micron thick, homogeneous 1%-Er-bearing GaAs film grown by molecular-beam epitaxy on a semi-insulating GaAs substrate. The PC switch (Fig. 8), biased by an 80 V tunable-DC-power supply, consisted of a 9×9 micron gap at the center of a 3-turn square-spiral antenna. THz radiation emanating from the spiral antenna was coupled into free space using a high-resistivity silicon hyper-hemispherical lens. For THz power detection, four different detectors were used at various stages, each of these was fed into a lock-in amplifier for data collection. At the same time, photocurrent was monitored with an oscilloscope by measuring the voltage across a known resistor in series with the PC switch.

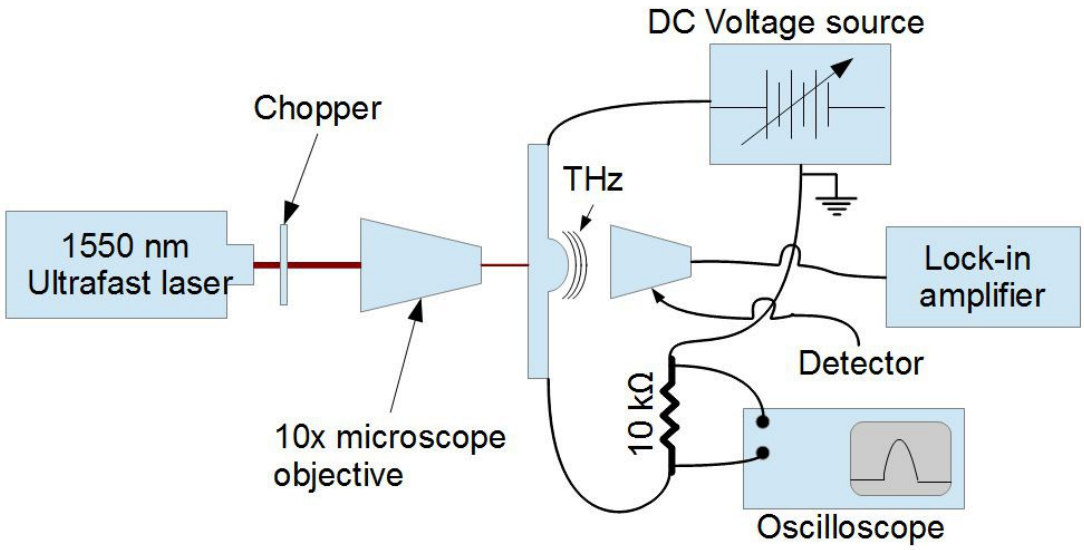

Figure 15: PC switch setup block diagram. This setup was used for the initial discovery of THz power generated with an ErAs:GaAs PC switch and a 1550 nm fiber laser.

The first step in this experiment was to illuminate the biased PC switch with the 1550 nm laser and see if any photocurrent was generated. This would be a telling step for the whole experiment; if any photocurrent was observed at all, then a sub-band-gap photoconductive process must be occurring. To start this step, the laser needed to be aligned onto the PC switch gap. This is a painstaking process; the 1550 nm photons are not visible and if the laser is focused onto the contact pads of the antenna, rather than on the antenna itself, the PC switch can experience catastrophic failure. So to start, the laser was intentionally defocused so that it illuminated the entire PC switch antenna. This way the irradiance of the laser would be reduced enough to prevent device failure if the contact pads were illuminated by mistake. Then the PC switch (mounted to an X-Y-Z stage) was moved into the beam path of the laser while the photocurrent was monitored on an oscilloscope. Immediately a very exciting result was obtained; while the laser was still defocused photocurrent was already observed on the oscilloscope. The laser was

then brought into focus so performance metrics could be recorded.

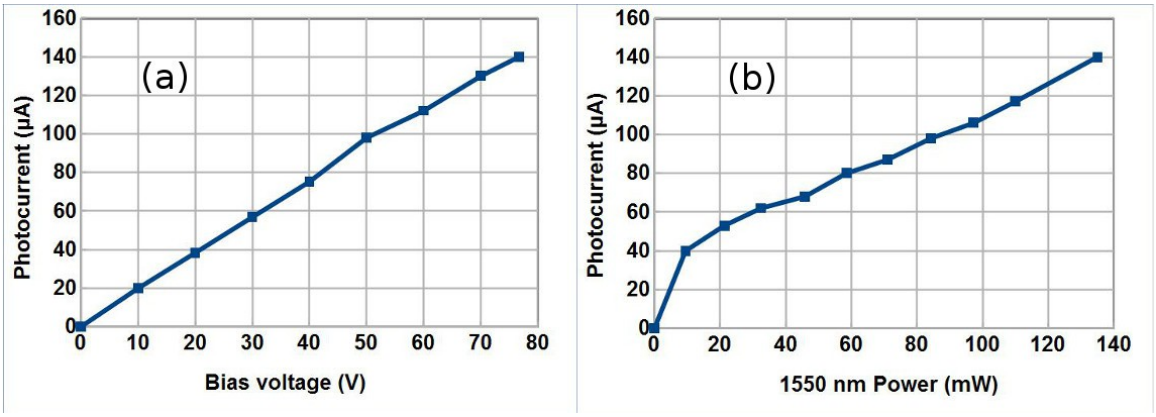

Figure 16: (a) Photocurrent vs. bias voltage with 140 mW of 1550 nm laser power. (b) Photocurrent vs. average laser power at a fixed DC V_B (77 V).

Several measurements were taken to thoroughly characterize the PC switch performance in this experiment, since later this would allow for careful examination of the physical mechanism behind the results. The first measurement taken was the DC photocurrent vs. bias voltage V_B with the laser power fixed at the maximum power of 140 mW. The results are shown in Fig. 16(a) and as expected the photocurrent goes to zero as V_B goes to zero. As V_B increases, the photocurrent increases nearly linearly, consistent with the current increasing (nearly[8]) linearly with the electric field (Eq. 4). Fig. 16(b) shows the DC photocurrent vs. average laser power at a constant V_B of 77 V (the maximum voltage of the power supply used). Here, the photocurrent curve is concave down at low laser power (<10 mW) but as laser power increases above 10 mW the photocurrent curve becomes linear. This is in contrast to the quadratic-up behavior displayed LT-GaAs PC switches driven at 1550 nm [57] and GaAs based PC switches operating at 800 nm. The photocurrent responsivity from Fig. 16(b) at the lowest laser

8 Sometimes the increase is concave up because the carrier mobility can increase slightly with bias voltage [6].

power (10 mW) is $\Re \approx 5$ μA/mW but at the highest power drops to $\Re \approx 1$ μA/mW. The responsivity at high power is only about 4 times less than what is seen with the exact same PC switch driven with an 800 nm laser, at the same V_B. The fact that so much photocurrent was measured suggests that measurable THz power should be produced. This assumes, of course, that the bandwidth associated with the new photoconductive mechanism is comparable to that of the traditional intrinsic, cross-gap effect.

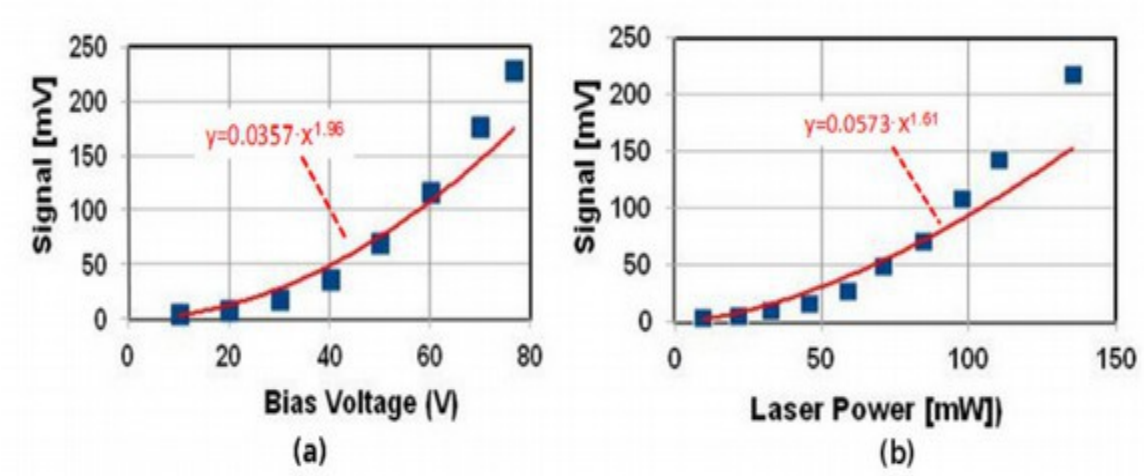

Figure 17: (a) AC signal (rms) from THz pyroelectric detector vs. bias voltage with a constant laser power of 140 mW. (b) AC signal (rms) vs. 1550 nm average laser power at a constant bias voltage of 77 V.

Next, THz power measurements were taken from the PC switch, starting with a broadband, calibrated $LiTaO_3$ pyroelectric detector. To prevent 1550 nm laser power from being detected a 0.01 inch black polyethylene window was placed in front of the pyroelectric detector. Black polyethylene will block 1550 nm and thermal IR radiation, but is ~90% transparent at ~1.0 THz. The experimental results for broadband THz power vs. V_B and laser power are shown in Figs. 17(a) and 17(b), respectively. The y-axis in both plots is the root-mean-squared (RMS) lock-in amplifier readings in Volts.

Correcting for the RMS reading, the equivalent peak-to-peak reading was 520 mV (confirmed on an oscilloscope). The pyroelectric detector used for this measurement has a calibrated, broadband external responsivity of ~5000 V/W between 0.1 and 1.0 THz; therefore, the maximum power measured from the PC switch is ~105 μW (520 mV / 5000 V/W). This is quite comparable to the broadband THz power measured from an identical PC switch (with the same ErAs:GaAs material) driven at 800 nm, with the same V_B, but driven with an average laser power of 25 mW [7]. This means that the new 1550 nm drive mechanism is about 5 times less efficient in terms of THz-to-laser power ratio (however there may be a way to compensate for this, as will be discussed shortly). The behavior of both plots in Fig. 17 is also slightly different than what is observed in an 800 nm driven switch. The bias dependence (Fig. 17(a)) is close to quadratic (see equation for curve fit) and the laser power (P_o) dependence is lower, $P_{THz} \approx P_o^{1.6}$. With 800 nm drive, the laser power has a larger effect on P_{THz}, compared to V_B; a fact that makes sense considering that in intrinsic operation the photocurrent in the PC switch increases nearly quadratically with laser power, whereas here the increase is linear.

With the pyroelectric measurements confirming that large amounts of THz power were being generated, the next step in characterizing the 1550-nm-driven PC switch was determining the bandwidth. To get a rough estimate of the bandwidth, power measurements were taken using a set of three zero-bias Schottky-diode rectifiers that were mounted in rectangular waveguides, operating in three distinct bands centered around 92 (W-band), 415, and 675 GHz. These rectifiers act as band-limited filters with very sharp low-frequency turn-on (waveguide cutoff) and more gradual high-frequency

roll-off. Because the external responsivity, noise equivalent bandwidth, and effective aperture (each detector was coupled to a diagonal feedhorn) of each Schottky was known, discrete estimates could be determined for the THz power at the center frequency of each detector. The discrete power estimates are calculated by $P_S = V_D/\Re$ and then normalized to each detectors bandwidth and effective aperture by $P_{SN} = P_S/A_{eff}/\beta$, where V_D is the detector reading, A_{eff} is the effective area of the detector, $\Re$ is the responsivity of the detector (V/W), and β is the detector bandwidth.

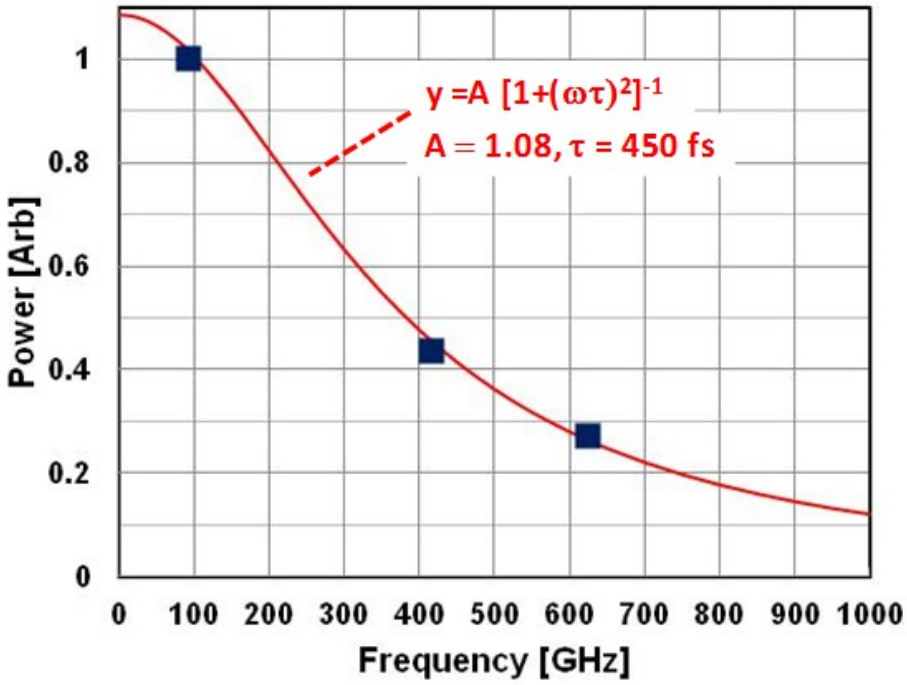

Figure 18: Bandwidth calculation using spot frequency power estimates taken with 92, 415, and 675 GHz Schottky diode rectifiers at a constant V_B of 77 V and constant 1550 nm laser power of 140 mW.

The bandwidth is then obtained by fitting the discrete power measurements to a single-pole Lorentzian function, $S(f) = A[1+(2\pi f\tau)^2]^{-1}$, where A is a fitting constant and τ is the photocarrier lifetime. This has been found to be a good fit to the THz power

spectrum of PC switches whose photocarrier lifetime is significantly longer than the RC electrical time constant – a likely condition in this case since the gap capacitance of the switch is << 1 fF. For the data in Fig. 18, the best fit occurs when A = 1.08 and τ = 0.45 ps, which corresponds to a -3 dB frequency-domain bandwidth of $B = (2\pi\tau)^{-1}$ = 354 GHz. This bandwidth is comparable to the bandwidth deduced from 800 nm time-domain measurements for an identical type of PC switch (with the same ErAs:GaAs material) [61]. However the laser pulse in this 1550 nm experiment was 300 fs, considerably longer than that used in the 800 nm experiments, so the fundamental PC switch bandwidth could be even higher than 354 GHz.

The results from this discovery are all consistent with the new photoconductive mechanism in the 1550 nm driven PC switch being *extrinsic* photoconductivity, rather than the traditional *intrinsic* photoconductivity used in PC switches up to this point. Extrinsic photoconductivity, as shown in Fig. 12(b), is a linear process (Eq. 5) distinguished by a carrier transition from a localized-impurity or defect energy level to one of the energy bands (conduction or valence), and then subsequent unipolar photocarrier transport (electron or hole) within that band [1], [2], [4]. It is well known in doped semi-insulating GaAs and has long been utilized to make high-power PC switches operating at the ~10 ps time scale [55]. Through the growth conditions discovered in Refs. [45], [46] and described earlier in this chapter, the present PC switch material contains ErAs in the form of crystalline nanoparticles and substitutional defects, and these impurities are associated with a very large density of energy levels near the middle of the GaAs bandgap. This explains the sub-ps electron-hole photocarrier recombination

time in intrinsic operation, and should explain the fast extrinsic operation through a large capture cross section for electrons and holes, as the case may be. As shown in Fig. 14, the ErAs energy levels have also been found to display sub-band-gap absorption that reaches a peak strength around $\lambda = 2.5$ μm, either through a particle-plasmon [60], or quantum dot resonance [5].

From the work presented here, the exact absorption mechanism could not be determined exactly. Nevertheless, it certainly creates abundant photocarriers, which in turn exhibit good electric transport (i.e. good mobility) and the sub-ps lifetime necessary to generate useful levels of THz radiation in PC switches. In GaAs this would suggest electrons rather than holes because of their superior band transport. In any case, the absorption coefficient is likely much weaker than the cross-gap value around 800 nm, which is typically $\sim 10^4$ cm^{-1}. This would partially explain the 4-times lower external photocurrent responsivity and 5-times lower laser-to-THz conversion efficiency of the 1550 nm driven switch. But lower absorption has a beneficial aspect which is more gradual photocarrier and thermal generation with depth than normally occurs in GaAs PC devices. This should help improve the reliability and allow for higher drive power, which are often limited by electric and/or thermal stress at the surface of planar PC devices. And the oft-stated fact remains that 1550 nm photons are much more affordable than 800 nm photons, and much easier to route and control via the wide variety of active and passive components available from the fiber-optic telecomm, industry. Because of this the lower laser power-to-THz conversion efficiency problem can be compensated for by adding more laser power (as done here) while still reducing the cost of the drive

components.

The discovery made in this work has shown that an ErAs:GaAs PC switch can produce useful levels of THz power when driven by an ultrafast 1550 nm fiber MLL. The external responsivity and THz generation efficiency are lower than those in the same PC switch driven by 800 nm sub-ps pulses, but the absolute THz power level is comparable. The likely mechanism for the 1550 nm excitation is extrinsic n-type (electron) photoconductivity from the ErAs-impurities to the conduction band, although more research is needed to prove this unequivocally. To further understand and improve upon the discovery made in this section more experiments were then planned.

2.2.2. Testing extrinsic photoconductivity in ErAs:GaAs at 1030 nm

The first additional experiment was testing the ErAs:GaAs PC switch at another common sub-band-gap telecomm wavelength, 1030 nm. Ultra-fast lasers at this wavelength are also readily available and inexpensive. The goal of this experiment was to confirm the extrinsic photoconductive effect, as opposed to other possible mechanisms, such as two-photon absorption (Fig. 12(c). Therefore, the experiment at 1550 nm was fully repeated with an ultra-fast 1030 nm laser (YDFA – ytterbium doped fiber amplifier). Assuming that the deep-level energy states lie at the middle of the GaAs bandgap, the extrinsic effect should only require half of the GaAs band-gap energy, ≈ 0.71 eV below the conduction-band edge. The 1550 nm photons used in the initial discovery provide just over half (~0.80 eV), so can be absorbed by deep-level-to-band transitions, or by cross-gap two photon absorption [57]. In contrast, the 1030 nm photons (~1.20 eV)

should still exhibit strong deep-level-to-band transitions, but weaker two photon absorption by about 30x (as seen on Fig. 13(b)).

The experimental setup for this test was exactly the same as in Fig. 15, but with an ultra-fast (190 fs pulse width) 1030 nm laser. The PC switch used was also exactly the same as the 1550 nm test. Earlier work (Fig. 14) showed that the defects created by the erbium doping process exhibit good sub-band-gap absorption with a minimum in the measured range at 1.5 μm, so sub-band absorption should be present and possibly slightly higher for the 1030 nm laser [60]. For equal comparison between the 1550 nm and 1030 nm wavelengths, the PC switch was illuminated with the same average power level of 140 mW (although the YDFA could output up to 1.1 W average power). This power limitation was also used to guard against damaging the PC switch, since the maximum laser power it could withstand was not known. Laser power measurements were taken with a standard thermopile type optical power meter.

The first test done for this experiment was generating and measuring the photocurrent in the PC switch vs. 1030 nm laser power, with a fixed bias voltage of, again, 77 V, the result from this test is shown in Fig. 19. Photocurrent was indeed excited by the 1030 nm laser and interestingly it also exhibited quasi-linear behavior at high laser power, with a maximum value of 44.9 μA. Therefore, the responsivity with 1030 nm drive is $\Re \approx 0.32$ μA/mW, about 1/3 of the responsivity at 1550 nm. This linearity and magnitude of this photocurrent curve supports the interpretation of this new photoconductive effect as extrinsic photoconductivity. The current responsivity is ~10× higher than predicted by TPA theory. However, with the 1030 nm drive laser no THz

power could be measured from the calibrated THz pyroelectric detector, or from the Schottky diode detectors, suggesting that the photocarrier lifetime associated with the extrinsic photoconductivity is very sensitive to laser drive wavelength.

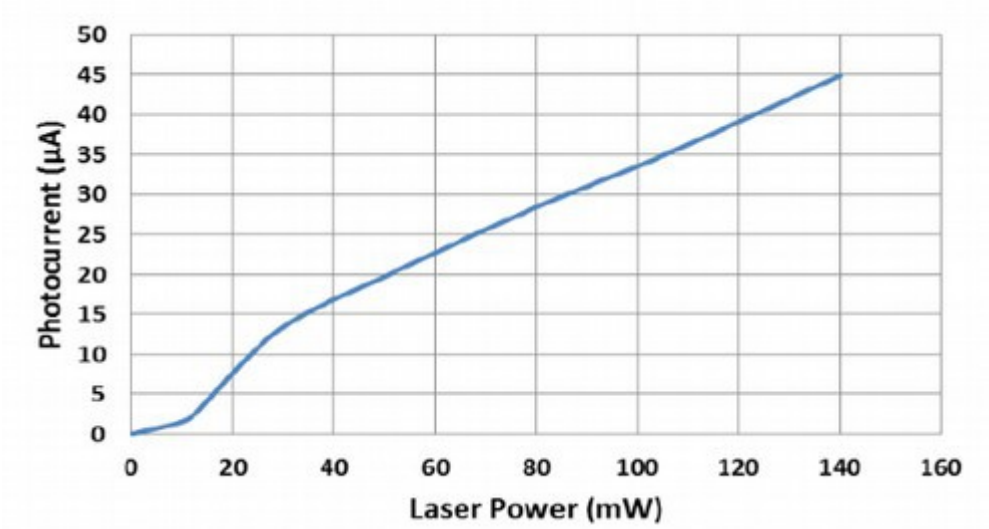

Figure 19: DC photocurrent vs. average 1030 nm laser power at a fixed bias voltage of 77 V, in an ErAs:GaAs PC switch.

This result confirmed that a strong photoconductive effect occurs in an ErAs:GaAs PC switch at both 1550 nm and 1030 nm sub-band-gap wavelengths. Although the effect is somewhat weaker at 1030 nm, the DC photocurrent that was produced in the PC switch was large enough to produce measurable THz power, assuming the carrier lifetime is well under 1 ps. However, no THz power could be measured from the PC switch when driven at 1030 nm. This suggests that the 1030 nm drive PC switch yields a much slower extrinsic photoconductivity, perhaps because the 1030 nm photon energy creates photocarriers well above (or below) the band edge. This lengthens the photocarrier lifetime and therefore hinders THz generation. The reason that photocarrier lifetime would be lengthened by excess photon energy can be seen

graphically in Fig. 20. The carrier must first lose the excess energy given to it by scattering in the crystal lattice, until it nears a band edge [2]. The results from this work were presented to the THz community [62].

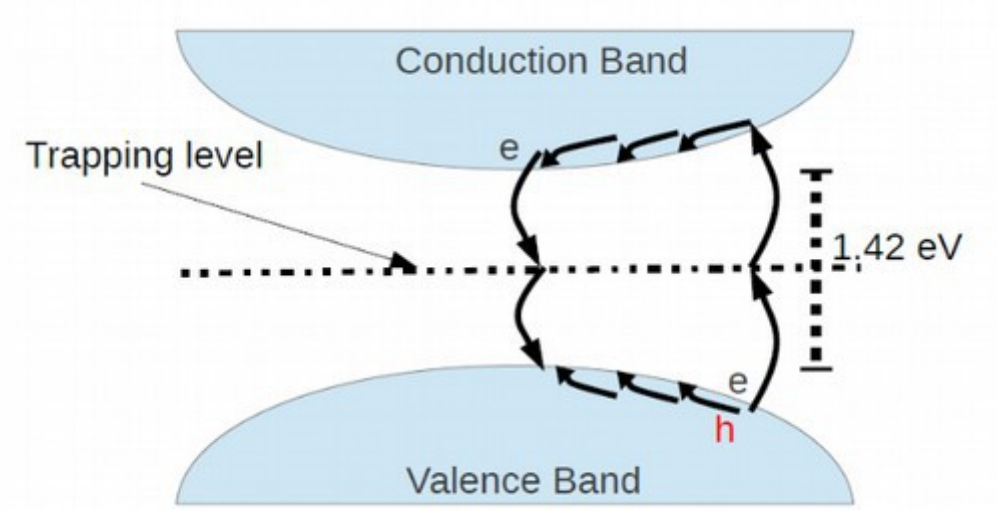

Figure 20: An extrinsic photoconductive process with excess energy given to the carriers. Before recombination can take place the carriers must relax back to the band edge. The top half of the diagram would be n-type, the bottom half would be p-type.

2.2.3. The effect of Erbium doping concentration

The next experiment was done with the aim of optimizing the performance of the 1550 nm extrinsic ErAs:GaAs PC switch. In the initial discovery and the 1030 nm tests, the ErAs:GaAs epitaxial layer was 1% Er bearing, as estimated by the MBE growers. For this experiment, PC switches with identical square spiral antennas were built on a new epitaxial layer that was 2% Er bearing. Having a different concentration of erbium in the photoconductive layer could have several effects. For example, a higher concentration of energy levels in the bandgap could increase the on-state conductivity of

the photoconductive layer, by increasing the number of carriers added by the laser pulse (Δn in Eq. 4). Another possibility is that the additional ErAs defects could begin to disrupt the GaAs crystalline structure, thus shorting the mean-free-time (5) and reducing carrier mobility. This outcome would reduce the THz power produced by the PC switch. Yet another option is that the additional ErAs nanoparticles could increase the number of mid-band recombination centers, which should aid in decreasing carrier lifetime [2]. Since little was known about the new extrinsic operation of ErAs:GaAs, this observational study would increase the understanding of the material, but it was believed that the additional Er doping would increase the on-state carrier concentration (Δn) of the photoconductor, and thus the photocurrent in the PC switch.

To conduct this study, the two PC switch types were inserted into the exact same experimental setup, this way experimental bias would be minimized. The experimental setup is again identical to that seen in Fig. 15, but this time a different 1550 nm ultrafast laser was used with an optical pulse width of 130 fs, a maximum average power of 90 mW, and a 56 MHz pulse repetition rate. To test the THz performance of the PC switches, broadband power measurements were taken and the same three band-limited zero-bias Schottky detectors (92, 415, and 625 GHz) were used to estimate the frequency bandwidth. Once again, the collected signals were amplified with a 30 dB LNA and then detected with a low-noise lock-in amplifier.

The first measurement to compare is the broadband power from each PC switch. This measurement, like every THz power measurement in this experiment, was taken with the maximum average laser power (90 mW) and 77 V bias. In this measurement,

the 2% Er bearing PC switch was producing more broadband power than the 1% Er bearing device, 40 μW vs. 30 μW. Next, the bandwidth estimation was performed using the Schottky detectors (Fig. 21), calculated identically to the initial discovery on page 37. The fitting procedure yielded estimates for the -3 dB bandwidth of $B = (2\pi\tau)^{-1} = 145$ GHz for the 1% Er PC switch and $B = (2\pi\tau)^{-1} = 200$ GHz for the 2% Er PC switch. These values were lower than expected, but could be a result of experimental conditions (inferior laser performance, PC switch degradation, or misalignment of the beam on the PC switch antenna). In any case, they were repeatable and the broadband power levels were very comparable to many contemporary PC switches. The average power of this laser was quite a bit lower than the laser used in the initial discovery as well (90 mW vs. 140 mW), so it is possible that bandwidth could improve as laser power increases, and the broadband power would certainly increase greatly.

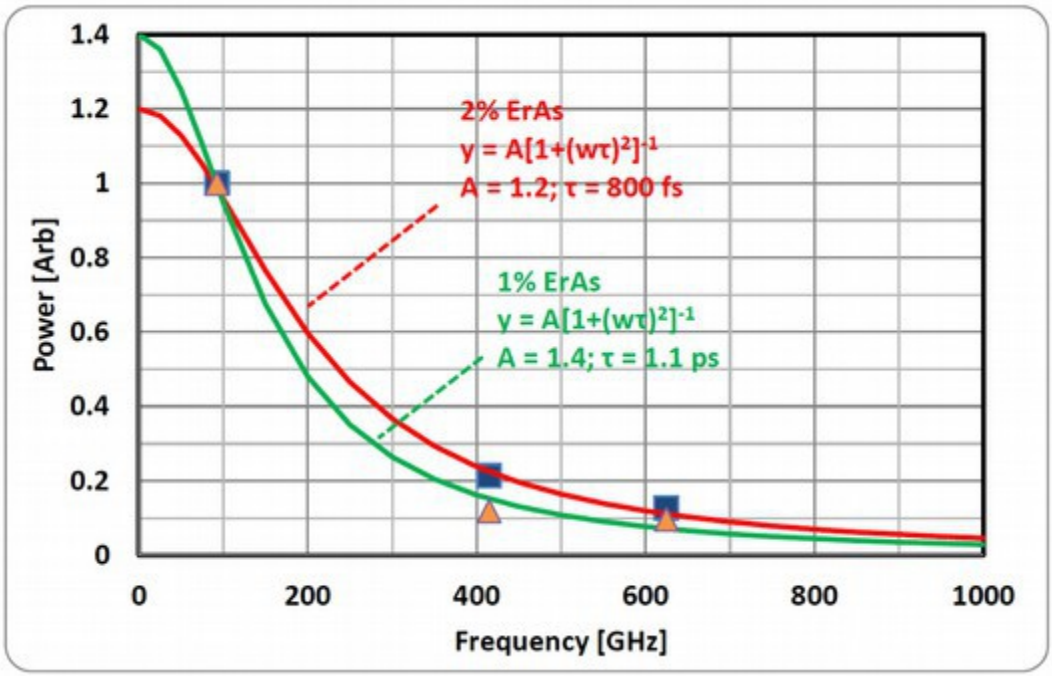

Figure 21: The estimated power spectrum from both the 1% and 2% Er doped ErAs:GaAs PC switches. The 2% switch had a broader bandwidth in this experiment. Note that both power curves are normalized to the 92 GHz values.

The results from this experiment suggest that the PC switch with higher Er concentration (2%) is a superior device. The broadband power collected with the pyroelectric detector is higher and the photocarrier lifetime is slightly shorter, enabling superior bandwidth. This suggests that increasing the Er concentration in the photoconductive layer had not degraded the quality of the crystal structure in any significant way. At the same time, the carrier-lifetime had been shortened, likely a cause of a higher density of trapping levels deep in the GaAs band-gap. It is also likely that the change in carriers between the off- and on-states increased (more were available), thereby increasing the on-state conductivity, and improving THz-to-laser power efficiency. The results from this study were important because they provided further proof that extrinsic photoconductivity is a practical method of THz generation, and improved on it. As such,

this work was presented to the THz community at the International Conference on Millimeter THz and Infrared waves [63].

2.2.4. Measuring ErAs:GaAs responsivity vs. wavelength

Next, to understand where the mid-band-gap energy levels were located within the band-gap, and to find which wavelength might be the most efficient for extrinsic photoconductive ErAs:GaAs excitation, another experiment was performed. This testing would measure the photocurrent responsivity at many more wavelengths compared to the previous experiment conducted with the 1030 nm ultra-fast laser, a combined wavelength range ~950 nm would be tested in total. For this experiment, a broadly tunable wavelength laser was needed, so a discretely tunable (1 nm step size) optical parametric oscillator (OPO) was used. The wavelengths generated from this laser included 1535 to 1793 nm and 2516 to 3293 nm; which corresponds to photon energies of 0.69 to 0.81 eV (0.48 to 0.57 U_G) and 0.37 to 0.49 eV (0.26 to 0.35 U_G). The two different Er concentrations (1% and 2%) were both tested in this experiment, to determine if there are any significant band differences between the two photoconductive layers.

The setup had to be slightly different here, compared to the previous experiments (Fig. 22). The width of the OPO pulses was very long (> 1 ns), which forces the antenna pulse width to be at least this large, and hence the bandwidth would be well below the THz region. So THz detectors were not needed, but the photocurrent response vs. wavelength could still be measured in a sub-band-gap wavelength range that was previously unexplored. A 1047 nm notch filter was also included in the experimental

setup to block leakage from the OPO pump laser. Aside from these two changes the experimental set up was identical to Fig. 15, and the laser power was again measured with a thermopile power meter for each wavelength. The laser pulses from the tunable OPO also had an extremely large peak power. Because of this the PC switches were destroyed if the laser was focused completely onto the PC switch gap. To combat this the laser simply wasn't focused. This prevented absolute photocurrent measurements (hence the normalized curves in Figs. 23, 24), but the qualitative photocurrent responsivity difference between wavelengths could still be determined.

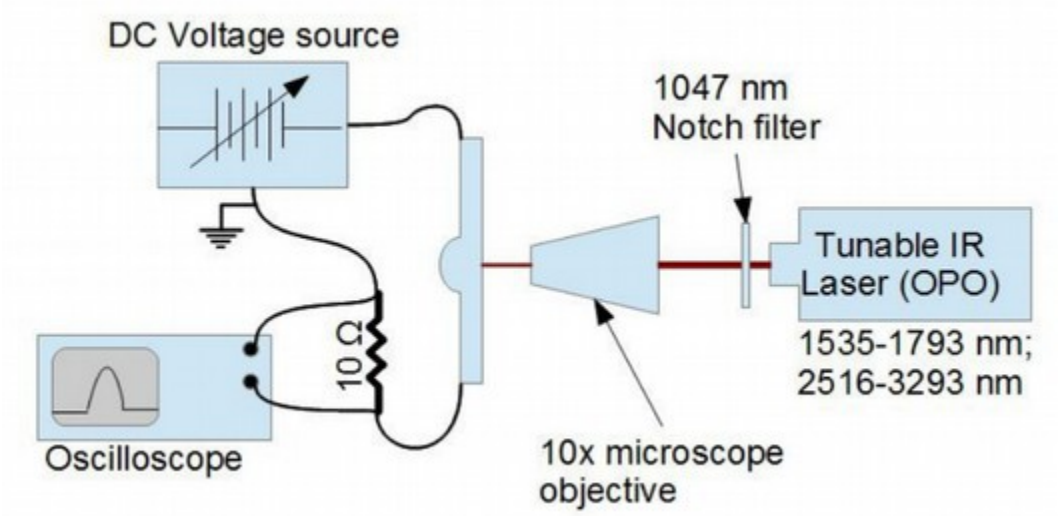

Figure 22: The experimental setup for measuring the extrinsic photocurrent response vs. wavelength in two ErAs:GaAs PC switches. The 1047 nm notch filter was present to block any leakage from the OPO pump laser.

The results for both the 1% and 2% Er bearing PC switches are shown in Fig 23. Very interesting behavior is immediately noticeable, where several peaks in the photocurrent can be observed across the high-energy wavelength range (1535-1793 nm). These peaks were attributed to ErAs nanoparticles, sitting at slightly different energy levels, behaving like quantum dots [45]. Another compelling result is that the peak of the

photocurrent was not seen in the available wavelength range (unless it happens to be at 1535 nm). However, because of the known lower responsivity measured in the 1030 nm experiment, there must be a responsivity peak somewhere between 1030 and 1535 nm.

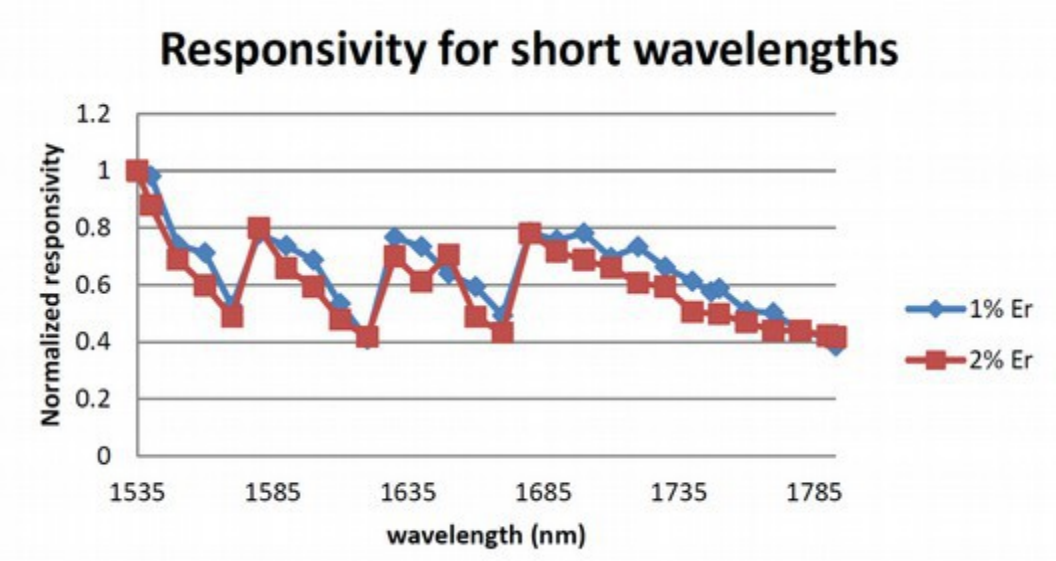

Figure 23: The normalized photocurrent responsivity vs. wavelength for both the 1% and 2% Er bearing PC switches in the 1535 to 1793 nm wavelength range.

Another interesting result illustrated in Fig. 23 is that the two responsivity curves have nearly an identical shape. This means that the ErAs nanoparticles are likely arranging themselves in the GaAs crystal lattice similarly at both doping concentrations, and it also means that the higher doping concentration is not causing degradation of the GaAs crystalline structure. The responsivity for the low-energy wavelengths (2516-3293 nm) is shown in Fig. 24. The photocurrent response at these wavelengths was flat and very low. In fact, any response that was measured is likely caused by 1047 nm light leaking through the notch filter. This was an expected result because the photon energy from these long wavelengths is very small, and probably too small to cause defect-to-band carrier transitions.

The results from this experiment suggest that the most of the ErAs energy level defects do not sit directly in the middle of the GaAs band-gap, but somewhere on either side (likely closer to the conduction band) because the peak responsivity levels are not at the mid-band wavelength (1747 nm). However the energy levels are still deep in the band-gap, because the longer wavelengths did not create photocurrent. Interestingly the results do not seem to change significantly between the two Er concentrations that were measured. This means that ErAs nanoparticles are likely being formed in a similar way in both devices. These results, combined with the results of the 1% vs. 2% Er THz performance study in the previous section, mean that even higher Er concentrations might be a pragmatic step for extrinsic photoconductivity in ErAs:GaAs PC switches, because performance only improved at 2% Er doping (assuming the GaAs crystalline quality is maintained). These results further confirm that this is extrinsic photoconductivity because responsivity did not increase at the half-band-gap wavelength, and also helped to further the knowledge of extrinsic photoconductivity in the THz field. As such, they were presented to the THz community at the International Conference on Millimeter THz and Infrared waves [64].

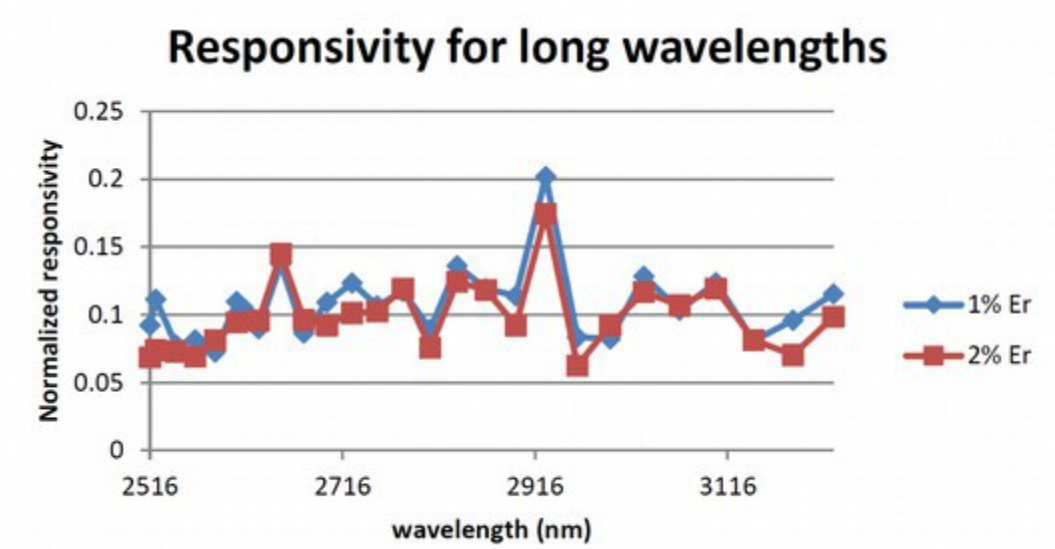

Figure 24: The normalized photocurrent responsivity vs. wavelength for both the 1% and 2% Er bearing PC switches in the 2515 to 3216 nm wavelength range.

2.2.5. The first photomixing experiments on ErAs:GaAs at 1550 nm

The last experiment presented in this section was done for two primary reasons: (1) to help verify that the sub-band-gap process in ErAs:GaAs is indeed extrinsic photoconductivity and not two-photon absorption, and (2) to take the first steps towards developing a new 1550-nm-driven frequency domain spectrometer. For this experiment, a photomixer was built on the same (2% Er) ErAs:GaAs material and initial tests were conducted to see if continuous-wave (CW) 1550-nm photons could generate photocurrent in the photomixer. The design of a photomixer is essentially identical to a PC switch, but smaller "fingers" are fabricated in the drive gap of the PC switch. An entire chapter could be written on photomixer design but that is not the focus of this work. The important factor here is if CW radiation can create photocurrent in the device. This is

important because two-photon absorption is a non-linear process and as such it requires very high peak laser power, such as seen in mode-locked lasers [59]. On the other hand, extrinsic photoconductivity is a linear process and should respond with the photocurrent proportional to CW laser power. So, if photocurrent is indeed generated, then the photoconductive mechanism must be extrinsic.

The experimental setup here is exactly the same as Fig. 22, except the PC switch is replaced with a photomixer, and the OPO is replaced by a CW 1550 nm laser, delivering a maximum average power of 60 mW. To create an AC signal that could be easily detected the CW laser beam was electronically chopped with a fiber-optic modulator at 4 kHz. Photomixers can not withstand V_B levels as high as a PC switch, so in this work the maximum V_B was 20 V.

First, the laser was focused in on the photomixer (with the same precautionary procedure described on page 31) while it was biased, and immediately an positive result was obtained; photocurrent was observed. This result was gratifying, because it proved the extrinsic photoconductive effect. The next step was characterizing the photocurrent generation as a function of laser power and V_B. Fig. 25 shows the result from this test and the photocurrent increases linearly with bias voltage, just as it did in the PC switch experiments. Again, this is consistent with Eq. 4 In that the photocurrent should increase linearly with electric field.

Next, the photocurrent was measured as a function of input laser power and again the increase in photocurrent was linear (Fig. 26), just as in the PC switches, and suggesting extrinsic photoconductivity. The only noticeable difference in behavior is that

the low laser power measurements are also linear, instead of concave.

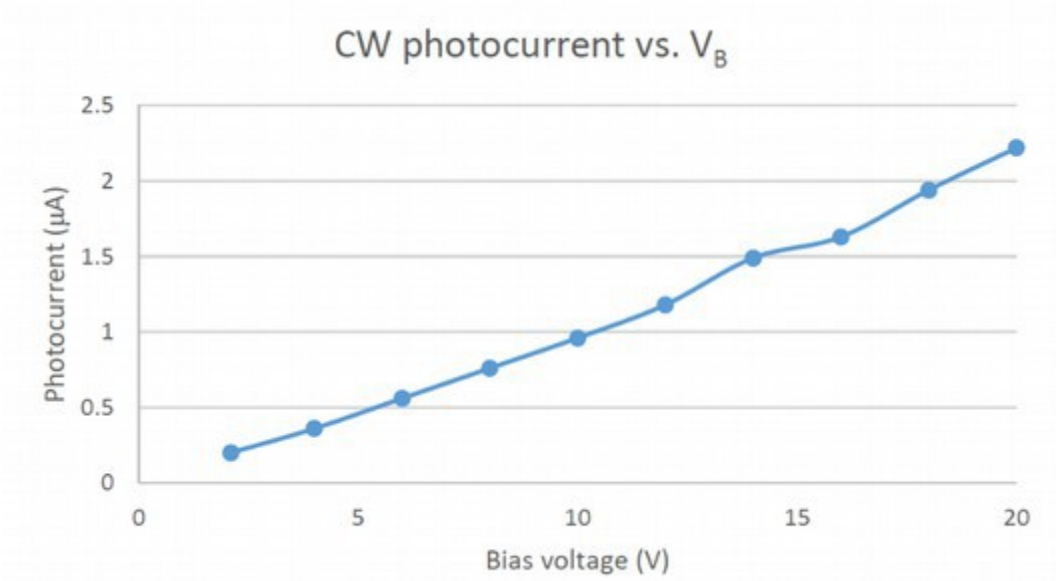

Figure 25: The measured photocurrent vs. bias voltage in a 2% Er bearing photomixer.

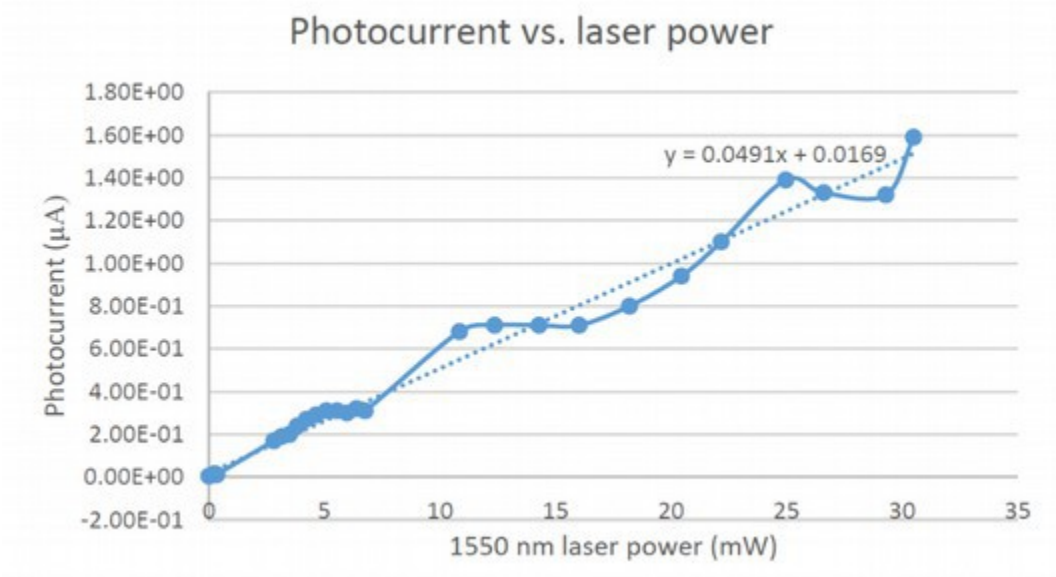

Figure 26: The measured photocurrent vs. 1550 nm laser power in a 2% Er bearing photomixer.

The results from this experiment confirm that the sub-band-gap photoconductivity discovered in this work in ErAs:GaAs is extrinsic, and is easily strong enough to generate useful THz power. Here only one laser was used to drive the photomixer, just to measure the responsivity. Because this experiment was successful, a 1550 nm photomixing, fiber-based frequency-domain spectrometer could be built with these photomixers. This is likely another Ph. D. dissertation worth of work in and of itself, so is an excellent project for future work. The first photocurrent generation in ErAs:GaAs at 1550 nm is a new discovery and as such is imminently publishable in a peer-reviewed journal once the first photomixing results have been obtained.

2.3. A summary of ErAs:GaAs based extrinsic photoconductive THz sources

A new technique of generating THz power was presented here and is very promising. The results show that it can produce THz power levels and bandwidths comparable to current PC switches at both 800 and 1550 nm drive wavelengths [5], [6], [48], [50], [53]. This technique could be a superior choice from a pure performance standpoint with further advancement. An example may be increasing the Er concentration past 2%. One of the key reasons that extrinsic photoconductivity has so much promise is that GaAs has a much higher critical breakdown field, compared to other 1550 nm driven PC layers such as InGaAs, by about 5x. At this point, the maximum safe driving conditions have not yet been determined either. It is likely that the ErAs:GaAs PC switches could be reliably biased at 100 V and the maximum laser power

that could be used is unknown, but certainly at least as high as 140 mW. The OPO experiments suggest that a very high repetition rate laser should be used as well, so that the peak laser power is lower (eq. 8 where P_{ave} is the average laser power, f_r is the pulse repetition frequency, and t_p is the pulse width). This way, the PC switches will not be destroyed by extremely high peak powers. It is also known that ErAs:GaAs does not absorb 1550 nm photons as efficiently as it absorbs 800 nm photons. Therefore, techniques that increase the number of passes of photons through the material (e.g. vertical optical cavities) will increase absorption and could enhance PC switch performance. This has been demonstrated previously for 800 nm wavelengths so it is likely possible [6].

$$P_{peak} \approx P_{ave} / (f_r * t_p) \tag{8}$$

From a more practical viewpoint, operating ErAs:GaAs PC switches with extrinsic photoconductivity is also superior because the 1550 nm lasers and components are less expensive and more readily available than their 800 nm counterparts. For example, the 140 mW 1550 nm laser used in the initial discovery cost ~$15000; to create 800 nm photons this laser had to be frequency doubled with a non-linear crystal, a component that increases the price by 50% or more [40]. Taking advantage of fiber-optic components should also reduce setup time and sensitivity of THz systems as well, since fewer free-space optical components will be necessary.

This discovery represents a significant, important, and new advancement for the THz field. However, the work done here, particularly on THz spectrum measurement, highlighted the need for a better THz spectrum analyzer as well (i.e. the difference

between spectral measurement in the initial discovery, and during the 1% vs. 2% Er experiment). As stated at the beginning of this chapter, the extrinsic PC switch discovery was made during the process of designing a new THz spectrum analyzer. This spectrum analyzer is different in operating principle from all contemporary designs in the THz region and is explained in depth in the next chapter. Eventually, in Chapter V, the final iteration of the new spectrum analyzer design is demonstrated experimentally via spectral measurements on the new ErAs:GaAs PC switch.

3. THz spectral analysis using a Fabry-Perot interferometer

Chapter II covered the advancements made in this research on THz sources. This discovery is certainly an important step for advancing the science and practicality of reflective THz spectroscopy because it lowers the cost of creating and controlling THz photons. The use of extrinsic PC switches can lead to new discoveries (and has already [54]) and improvements as well, but this discovery serves as a perfect illustration for another need: an inexpensive, yet accurate THz spectrum analyzer. The method used (in Chapter II) to determine the THz spectrum, while useful, has some deficiencies, as do other spectral analysis methods. So to more accurately measure the THz spectrum (and the output of new sources like the extrinsic PC switch) Chapter III addresses a new type of spectrum analyzer based on the Fabry-Perot interferometer [65]. This falls in line with the research plan (Fig. 27) shown first in Chapter II, and below.

The dashed box in Fig. 27 presents a visual illustration of what this chapter will cover. First will be a short description of commonly used methods of THz spectral analysis, the advantages and disadvantages of each. Then a novel Fabry-Perot-based spectrum analyzer (FPSA) will be presented – it is a promising component that may reduce the cost and difficulty of measuring the THz spectrum, especially in stand-off configuration (see Fig. 30). Several design iterations will be shown, and the motivation for each design will be explained. Then some proof-of-concept results will be presented.

Several iterations of software were written to control this component and that will also be discussed. Next will be an overview of the initial FPSA designs and results. Finally, Chapter III will end with the introduction of a new design concept of the FPSA that uses polarizing mirrors.

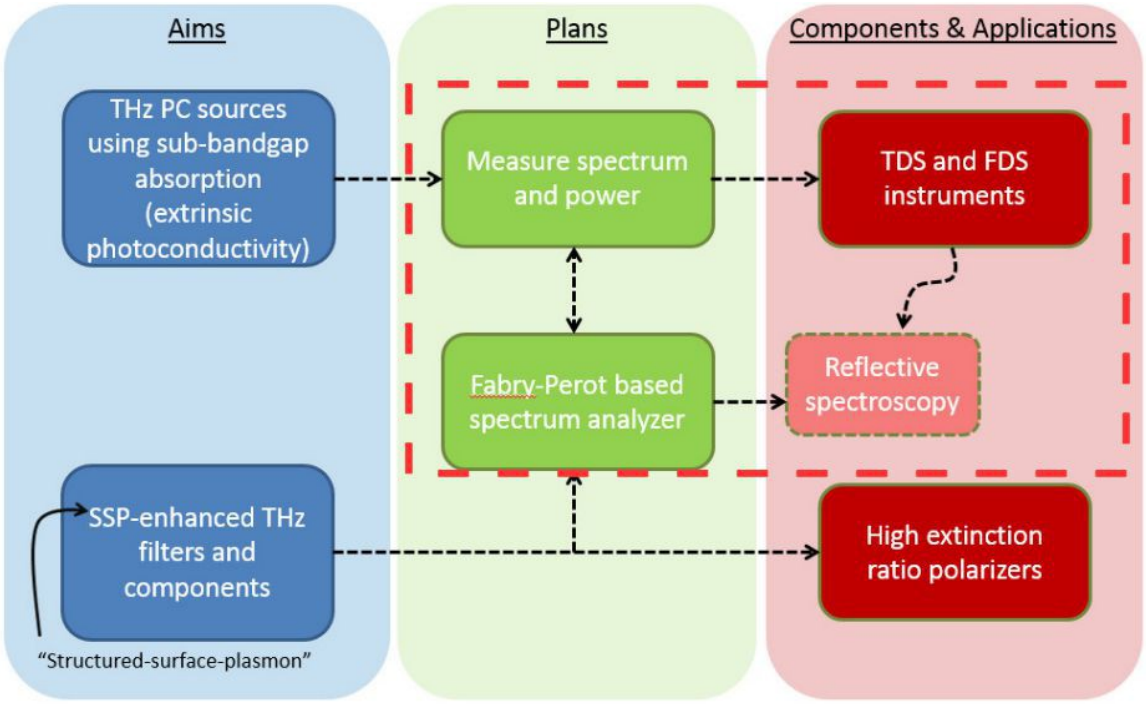

Figure 27: Research outline for this work. Chapter II covered the advances in THz PC switches, now this work will present a novel method of measuring the THz spectrum. This new method could then be applied to current instruments, devices, and applications.

3.1. Contemporary THz spectrum analysis techniques and their limitations

The quest for practical THz sources and components for stand-off reflective spectroscopy is ongoing and steady progress has been made. Since the invention of the LT-GaAs photoconductive antenna, the THz power available from photoconductive (PC) switches has risen from mere nW's to over 1 mW [7], [31]. This huge advancement in

available power has lead to the creation of many commercial THz spectroscopy and/or imaging systems, a small sample of which can be found in refs. [66], [67]. The PC switch advances made in this dissertation will push stand-off THz systems even closer to practical commercial use through the use of 1550 nm drive lasers. As explained in Chapter II, 1550 nm technology is considerably less expensive than 800 nm technology.

Nevertheless, despite the system improvements, there has always been difficulty in characterizing new THz sources, detectors, and systems. This difficulty is evident in the THz bandwidth calculations of Chapter II where measurements taken on identical PC switches differed by as much as 50%. These results suggest that the spot frequency method used is good for general spectral estimations, but not for final specification. The difficulty in spectral characterization stems from the brevity of THz pulses. No detectors in the world have the rise and fall time needed to measure individual sub-ps scale time-domain pulses, so other methods must be used. The problems presented by current THz spectral analysis methods have motivated research into a new type of THz spectrum analyzer based on a well-known optical device, the Fabry-Perot interferometer. This new, low-cost, fast spectrum analyzer could improve the efficiency of THz source and detector research by simplifying spectral measurements. The FPSA could be placed in line with any source or system and measurements can be taken in minutes (the timescales of most human activity). A bonus of the FPSA design is that it will be a far more practical device for use in stand-off reflective spectroscopy; such a configuration is required for real-world use when the target may not be perfectly still.

3.2. An innovative spectrum analyzer: The THz Fabry-Perot interferometer

TDS systems, FTIR, and spot frequency measurements approach a single problem (spectral analysis of a PC switch) in different ways: the TDS and FTIR systems measure THz pulse intensity vs. time, while spot frequency measurements are intensity vs. frequency. These time-domain and frequency-domain approaches are often viewed by researchers in a proverbial box, where they are completely separate entities. Yet, some enticing possibilities could exist if ideas from these two approaches were used in a complementary fashion. The new spectrum analyzer concept uses exactly this type of "mixed" frequency- and time-domain approach to the problem, by using a tunable band-pass filter to measure nearly discrete frequencies from broadband pulses typically associated with time-domain systems, while the band-pass center frequency is scanned.

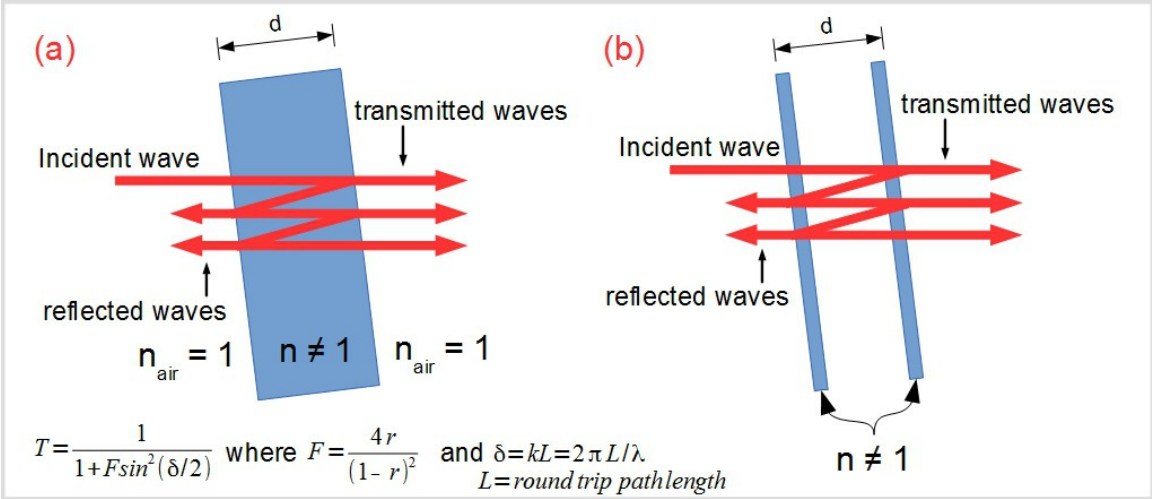

Figure 28: Fabry Perot interferometers. (a) The etalon, the parallel plates in this type of Fabry-Perot are fixed in position because they are opposite sides of a single plate. Reflections occur at the air-to-plate interfaces. (b) The parallel plate Fabry-Perot. The principle with this Fabry-Perot is the same, but two separate plates compose the reflective interfaces. This adds flexibility to the design [65], [68].

The Fabry-Perot interferometer (FPI) is a simple, common optical interferometer composed of two parallel and partially reflective interfaces (mirrors where $n \neq n_{air}$). It is similar to an etalon (Fig. 28(a)) but the separation between the two separate reflectors can be varied (Fig. 28(b)). However, both rely on the same underlying physics. The difference in refractive index between the FPI mirrors and air will create some level of reflectivity (r) for incoming radiation, based on Eq. 9. Light waves that enter the FPI will then propagate back and forth between the plates, and any wavelengths that are an integral multiple of the round trip path length ($L = m\lambda$) will constructively interfere and pass through the second mirror with nearly unity transmission. At the same time, other wavelengths can be strongly rejected by means of destructive interference (especially when $L = m\lambda/2$). The equations for transmission (T) are shown in fig. 28 [65], [68].

$$r = \left| \left(\frac{n - n_{air}}{n + n_{air}} \right) \right| \tag{9}$$

An important attribute of band-pass filters is how strongly out-of-band wavelengths are rejected, for the FPI this is entirely dependent on the reflectivity of the mirrors (more reflective mirrors reject out-of-band signal more strongly). More reflective FPI mirrors also pass a narrower selection of wavelengths (narrower line-width) and have more wavelengths rejected between pass-bands (broader free-spectral range). A common metric used to describe the number of wavelengths a FPI can resolve is finesse (Eq. 10), the ratio of free-spectral range to line-width [68]. Higher finesse values mean that the FPI mirrors have higher reflectivity, an example of the effect finesse has on transmittance vs. wavelength is shown in fig. 29.

$$\mathcal{F} = \frac{\lambda_{FSR}}{\lambda_{LW}} = \pi\left(\frac{\sqrt{(R)}}{1-R}\right) \tag{10}$$

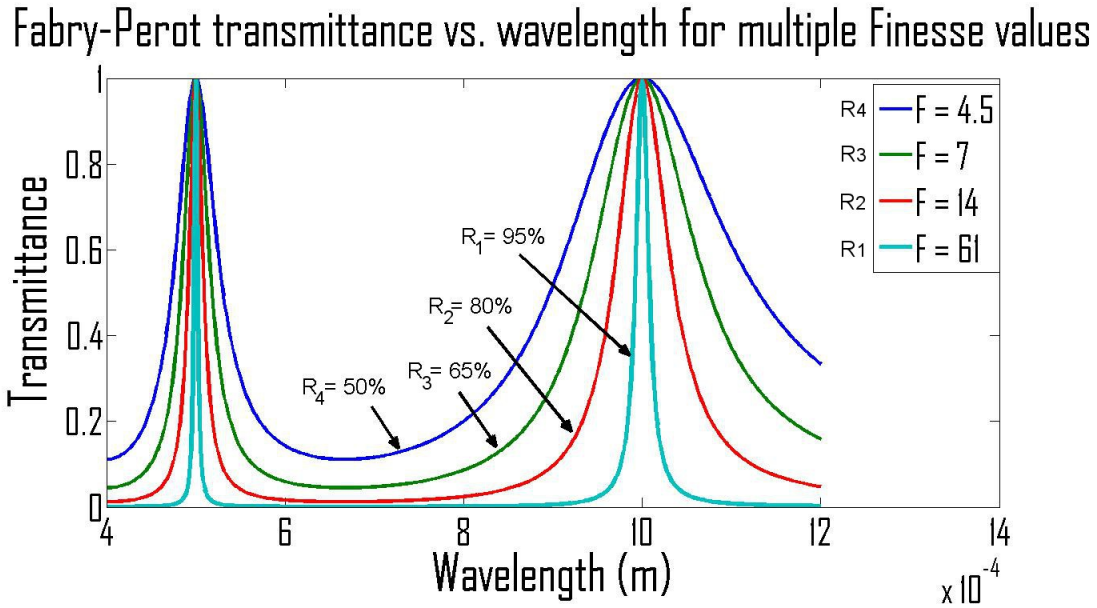

Figure 29: Higher FP mirror reflectance creates higher finesse. As seen here higher finesse values create much narrower band-pass features in a FP.

The transmittance vs. wavelength plot (Fig. 29), for several finesse values, shows how an FPI can act effectively as a (multiple) band-pass filter. Analyzing the transmission equation in fig. 28 it becomes apparent that the first band-pass feature occurs when L = λ (the plate separation d = λ/2) and every additional band-pass feature becomes narrower when plotted against wavelength, this is visible in fig 29 where L= λ is the right-most feature. The fundamental mode presents an interesting, useful possibility; as wavelengths longer than L as mostly rejected by the FPI. If the incoming radiation is broadband (like from a PC switch), and the detector is broadband (like a pyroelectric detector [69]), the total power detected will be mostly from the fundamental band-pass mode. This is because in PC switches the power output rolls off with frequency. For example, the power drop-off between 1 and 0.5 mm wavelengths (band-pass centers in

Fig 29) from the extrinsic ErAs:GaAs PC switch spectrum measured in chapter II, is >2x. Therefore, for experimental purposes, it might be possible to assume that the power detected with a pyroelectric detector is entirely contained in the fundamental mode. To enhance the result bandpass filters could also be used to eliminate unwanted modes.

An example of how the tunable THz FPI could be used for spectroscopy with the PC switches from Chapter II is shown in Fig. 30. First the broadband THz pulses are generated with the PC switch, then they are reflected off of some sample (or through the sample in transmission mode). Next the THz frequencies will be filtered by the tunable FPI and the signal vs. frequency measurements will be collected with a broadband pyroelectric detector. In this schematic a static band-pass filter is also shown, these could possibly be added to ensure that undesired frequencies are not being measured. In the case $\lambda >> d$ radiation can pass through the Fabry-Perot without destructive interference, and would show up as false signal, then requiring a short-wavelength pass filter.

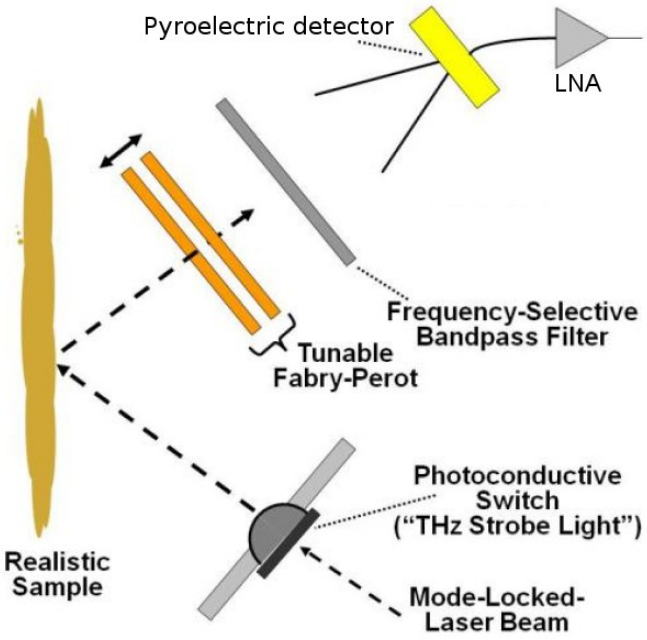

Figure 30: A prototypical setup for the FP spectrum analyzer, in reflection. This setup includes a band-pass filter. This could be added, if desired, to increase SNR.

The next part of this chapter covers the design of the THz FPI, for results the reader can advance to page 74.

3.3. Design and initial results of the Fabry-Perot interferometer

When this work started, a tunable high-speed THz Fabry-Perot spectrum analyzer of this type had never been created. The goal was to use the beneficial properties of the FPI described in the previous section and improved on them by making a THz FPI that could scan a broad range of frequencies at high speed [70]. To accomplish this advancement the tunable FPI was created by using the parallel plate design in Fig. 28b, while fixing one of the mirrors, and attaching the other mirror to a linear actuator so the mirror separation could be changed. Next, a new type of FPI mirror was needed; to achieve high frequency-selectivity (Finesse) the reflectivity of the mirrors must be very high, such as F=61 in Fig. 29. In optics, materials such as glass or plastic are usually used for the mirrors, but these will not work for this application. Glass is opaque at THz frequencies, and the reflectivity of plastics simply isn't high enough. For example, one common optical THz material is Teflon ($n \approx 1.5$), the reflectivity is only 20%. The Finesse using Teflon would be 1.75, lower than any curve plotted in Fig. 29 and frequency discrimination would be impossible. Therefore other materials had to be considered for the mirrors, a solution came from Radio-Frequency technology.

The properties of metal-wire meshes is well known in the RF region and they are often used to reflect RF radiation, or create Faraday cages, this concept can be applied to the FPI mirrors. Wire meshes will simulate solid conductors to incoming radiation as long as the incident wavelength is much larger than the mesh unit cell [71], with this condition met all incident waves are reflected by the mesh. As the mesh becomes closer in size to the incident wavelength some radiation begins to leak through. So by carefully

choosing the wire mesh size (unit cell period and wire diameter) it should be possible to create highly reflective (> 90%) mesh FPI mirrors for THz radiation.

Therefore the first task in designing the fast-scanning THz FPI was finding a wire mesh with the correct reflectivity between 0.1 and 1 THz. This work is primarily interested in spectroscopy between 0.1 and 1 THz because more power is available from a PC switch at these frequencies, there are fewer spectral water lines in this range, and there are still many signatures in this range [72]. To achieve the correct reflectivity in this spectral range several copper meshes were analyzed, all of which had periods smaller than the wavelength at 1 THz. The results are shown in Fig 31. and a mesh with 175 µm period and 55.9 µm diameter copper wires was the most appropriate for the THz FPI. In these transmission results the 175 µm mesh had a reflectivity ranging from 95% at 750 GHz to 99% below 450 GHz, this corresponds to a FPI Finesse > 60 for this spectrum.

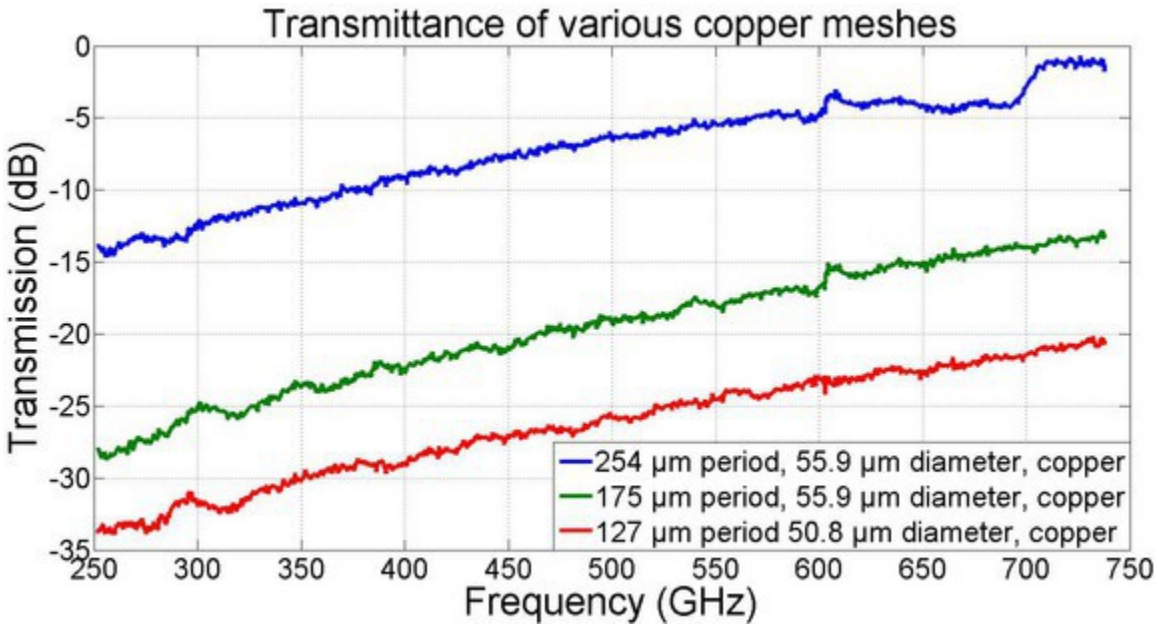

Figure 31: THz transmission data taken through 3 different copper meshes. The 175 µm mesh proved to be best suited for THz use, with 95% to 99% reflectivity (R = 1-T) across the measured spectrum.

After choosing the THz FPI mirrors, the remaining components of the fast-scanning tunable THz FPI could be designed. The areas of the FPI that needed to be designed or chosen included: a mounting system for the wire meshes, a slide system to ensure that the FPI mirrors move precisely and linearly, a linear actuator to control FPI mirror separation, and mounts for the linear actuator and mirrors.

3.3.1. Design 1: Sliding bushing-based Fabry-Perot plates with copper mesh mirrors

The first step in designing the fast-scanning, tunable FPI was finding a mechanical slide system that would allow the FPI mirrors to move precisely, while staying very parallel with respect to each other. For this initial design iteration a 30 mm cage rod system was chosen. The picture of the design in Fig. 32 shows that one of the FPI mirrors was fixed, this mirror was mounted to a one inch lens holder. This was chosen because the lens holder has the 30 mm cage rod holes built in, with set screws. The cage rods themselves were mounted to this lens holder with the set screws.

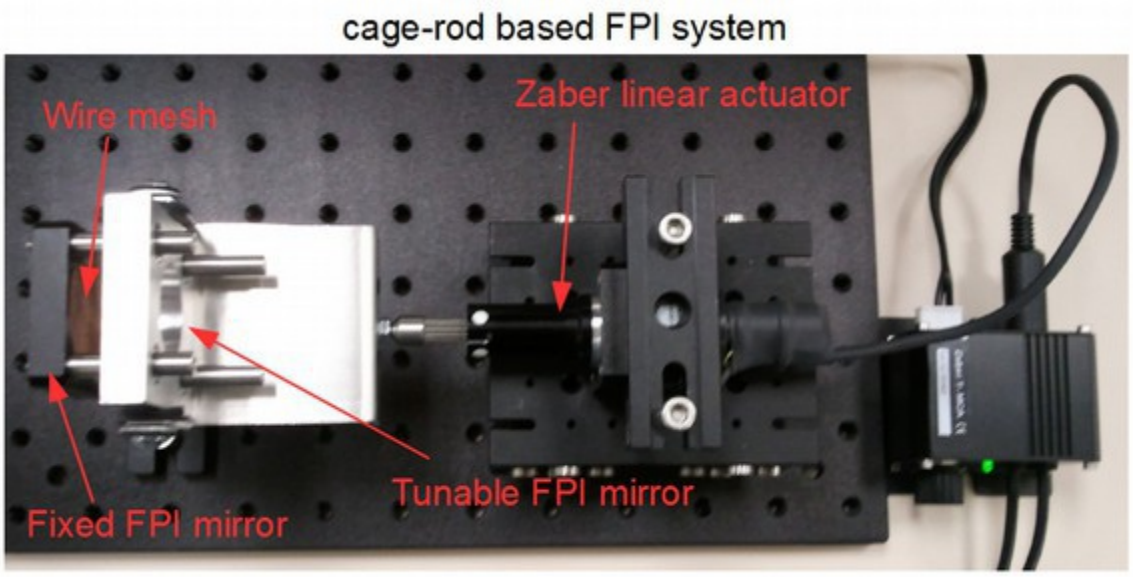

Figure 32: First FPI design. A standard 1 inch lens holder was used for the fixed mirror and the tunable mirror was custom fabricated. The wire mesh "mirror" was superglued to the metal frames.

The tunable mirror was made of the 6061 aluminum alloy because this material is very inexpensive, but also robust and light. A 1-inch hole was cut in the center of the mirror, to match the hole in the fixed mirror, and four additional holes were cut for the cage rods. However, because this mirror was intended to move, the holes were cut with much larger diameter than the cage rods (which were 6 mm in diameter) and oil-infused bushings were pressed into the holes. This was done so the tunable FPI mirror could slide easily (with low friction) on the rods. This mirror was also attached to a mounting plate. The mounting plate was built for two reasons: to prevent the bushings in the tunable FPI mirror from binding and to lower the linear actuator out of the THz beam path. Fig. 33 Shows how the FPI plate could bind from rotational forces acting on the bushings, this binding completely prevented the linear actuator from moving the FPI plate. The mounting plate was designed to make contact with the FPI plate only in the

middle of the plate, thereby reducing rotational binding forces and allowing the linear actuator to move the mirror. Fig. 33 is a side-view of the FPI setup and it also shows how the linear actuator is lowered out of the beam-path with the mounting plate.

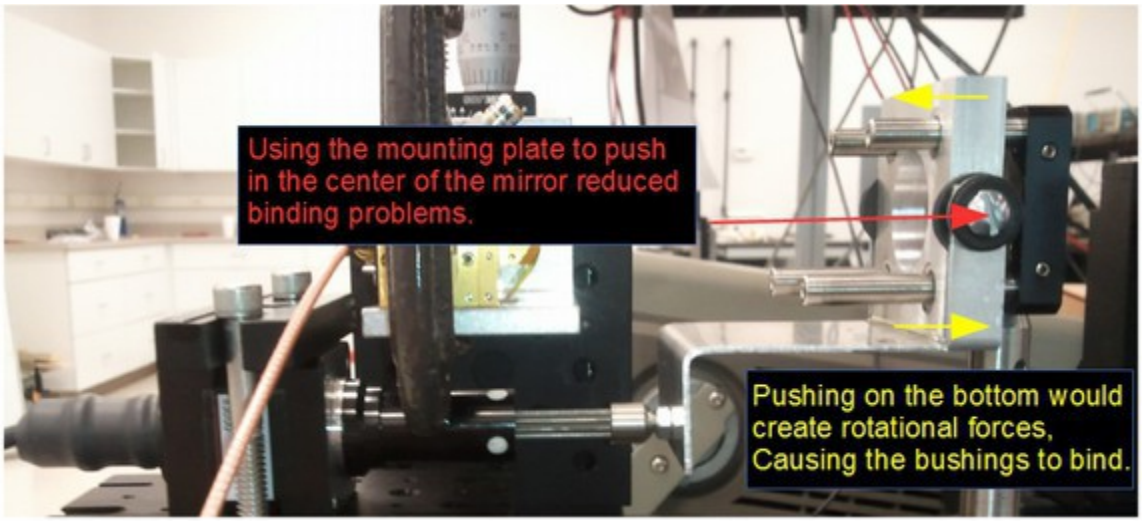

Figure 33: The mounting plate in this design lowered the linear actuator out of the beam path and helped the FPI slide more smoothly by reducing rotational binding.

As mentioned, the two mechanical plates shown in Fig. 33 are where the FPI mirrors are mounted, but the mirrors themselves are the wire-meshes presented in the previous section. In this FPI design, the wire meshes were simply laid of the FPI holes and glued into place. In Fig. 32 the mesh on the fixed mirror is visible. The mesh is applied to the tunable mirror in exactly the same fashion and is present in both Figs. 32 and 33 but the view is obstructed because it is on the side of the tunable plate that faces the fixed plate. Having the wire-meshes facing each other was an important design consideration; in order to resolve the fundamental mode of THz frequencies the mirrors (meshes) must become very close to each other. For example, to measure 1 THz the meshes must be only 150 μm apart. Because this design allows the meshes to come into contact, the spatial mirror separation necessary for high frequencies could be easily

achieved.

For precision control of the FPI mirror separation a linear actuator from Zaber Technologies Inc. was used [73], this actuator is pictured in Figs. 32, 33. When choosing the linear actuator there was three primary considerations: 1) The minimum step size must be small enough to resolve frequency differences of a few GHz or less. 2) The maximum movement speed must be fast enough to record scans quickly, one of the goals was to scan a spectrum in less than three seconds. 3) The linear actuator must be programmable. The frequency resolution requirement dictates a step size of ~1 μm. For example, at low frequencies, such as 100 GHz, a 1 μm change in mirror separation will correspond to a frequency-center change of ~0.1 GHz, and at 1 THz the frequency-center change will be 6.6 GHz. This resolution at the low end of the spectrum would be greater than most current spectral analysis methods, while at higher frequencies the resolution would be similar to what is currently seen in many TDS systems [67].

The maximum movement speed is dictated by the displacement that the linear actuator must cover. 100 GHz was intended to be the lowest frequency measured with the PFI, this corresponds to a plate separation of 1.5 mm. Frequencies higher than 100 GHz are then measured as this plate separation decreases, until eventually the desired maximum frequency is reach. If the maximum frequency for some measurement is 1 THz, this corresponds to a plate separation of 150 μm. So the plate separation would need to change from 1.5 mm to 150 μm (1.35 mm) in approximately 3 seconds. Therefore the maximum required shaft-speed of the linear actuator is 450 μm/s.

The Zaber model NA14C30 linear actuator was chosen for the tunable FPI

because it was inexpensive, exceeds both the step size and maximum speed requirements, and is programmable (pictured on the right side of Fig. 32 is the programmable controller). The minimum linear step size of this actuator is 0.381 μm and the maximum speed is 100 mm/s. Using this linear actuator this first design iteration of the FPI was completed and the whole device was assembled. Data was successfully taken with this fast-scanning, tunable-THz-FPI and is shown later in this chapter (page 77), the software written to control this FPI unit is also complete and included in this document in appendix B.

3.3.1.1. Design advances

This was the first FPI design, so there were no improvements over previous designs, however this design does represent the *first ever* fast-scanning, tunable-frequency THz-FPI spectrum analyzer to successfully collect data. As such it is a significant design and was presented to the THz community at an international conference [70].

3.3.1.2. Design shortcomings or problems

This FPI design was good proof of concept but had several problems. None of the problems prevent data from being collected, but they reduce the quality and accuracy of the collected power, which is critical when scanning for spectral signatures. The most notable problem was the binding issues mentioned in the discussion of Fig. 33. The mounting plate helped reduce binding, but it did not eliminate the problem. When the

bushings would bind on the cage rods, the FPI mirror would get stuck, thus causing the linear actuator motor to slip, this problem then became a chain reaction. Not only is the data ruined because several data points were taken at the same location, but the motor register is then offset. So whatever used to be theoretical motor position "X" was then motor position "X-Y" where Y is completely unknowable variable. This totally prevented the collecting of any more data until the motor was reset. The binding problem was also extremely sensitive to the vertical position of the linear actuator, The linear actuator actually had to be angled slightly because of the binding issue. To help ease the linear actuator alignment it was mounted on an adjustable-height platform. This vertical alignment sensitivity makes the FPI spectrum analyzer setup more challenging and time consuming than was intended.

Another problem was mirror parallelism, if the FPI bushings are binding due to some rotational forces, that means the FPI mirror is rotating slightly and therefore it cannot be parallel to the other mirror. The rotational forces one of the mirrors "rock" and slide down the cage rods at an angle. In addition to this, the binding of the bushings on the cage rods caused the linear actuator to exert a lot of force on the fixed FPI mirror, thus making it "lean" backwards. This also increased the angle between mirrors. Having some angle between the mirrors will cause inaccuracies in collected data, the distance on one side of the FPI cavity will be different from somewhere else in the cavity, thus creating a larger and less accurate spectral bandpass feature. To more effectively communicate this problem, it is illustrated in Fig. 34.

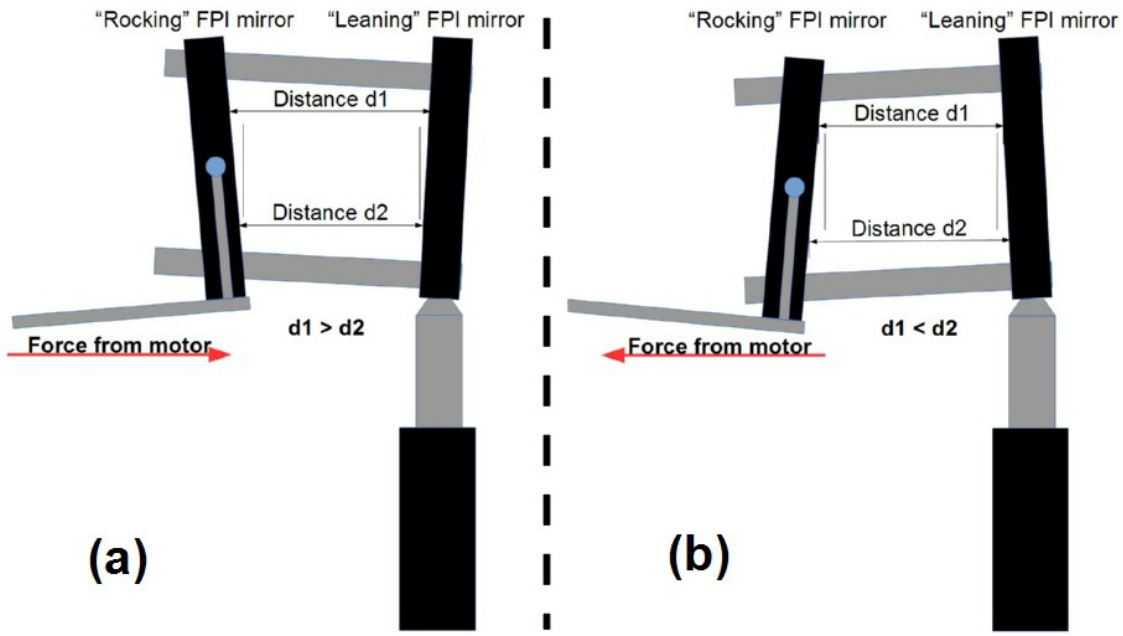

Figure 34: The binding and rocking problems (greatly exaggerated for illustrative purposes) with this FPI design. (a) The angles that are produced when the motor is driving the mirrors closer together. (b) The angles that are produced when the motor is pulling the mirrors farther apart.

Much of the rocking problem described here happens because the bushings are slightly larger than the cage rods (6.35 vs. 6 mm). An attempt was made with using 6.35 mm diameter cage rods, but the binding problems were considerably worse and the tunable FPI mirror would not move easily. Another problem would occur when the mirror movement direction changed. Since the mirror rocked at different angles, depending on the direction of movement, there would be a transition period when the movement direction changed. During this period the mirror separation doesn't change uniformly, rather the angle between the mirrors changes. This again lead to multiple data points being collected at the same plate separation. However because of adjustments made in the FPI controlling software (described starting on page 83) this problem was minimized.

There was also a smaller problem with this design that stems from how the wire meshes were mounted to the mechanical cage-rod plates. The plates were laid flat on a table, the wire meshes were placed on top of them, and then glued into place using standard superglue. The problem with this method is that the wire meshes are not guaranteed to be flat, Fabry-Perot mirrors must maintain flatness. Curved or distorted meshes will cause undesired frequencies to transmit through the FPI and this reduces the Q-factor of the measurements. After considerable use there was noticeable slack in the wire-mesh, so a better mounting solution was needed.

Additional wire-mesh Fabry-Perot designs were made, but not actually used for data collection, so they are located in Appendix A. A problem with all of these designs is that the wire-mesh mirror reflectivity shows a strong dependence on frequency. This is not surprising, as the reflectivity is directly dependent on the ratio of wavelength vs. unit cell size. So a scanned spectrum will not be truly accurate because the size of the bandpass feature will change with frequency, thus artificially changing the amount of power collected. If the change in reflectivity vs. frequency were small, it may be compensated for in post-processing with a frequency sensitive correction factor. Transmission vs. power in figure 31 increases exponentially by $-39.38*e^{(-0.001555*f)}$ (obtained with curve fitting tool), where f is frequency in GHz and the answer is in dB units. Dividing collected data by such a correction factor would compensate for the transmitted power difference vs. frequency.

Nonetheless, the change in reflectivity vs. frequency is not small. Figure 31 shows a spectral range of ~500 GHz and the transmission (and hence reflectivity

R = 1-T) changes by 15 dB for each curve. This change is so great that any single mesh will have trouble working over a 1 THz spectral range; using the exponential fit of the data in Fig. 31, if a mesh has appropriate reflectivity, say 95% at 1 THz, at 100 GHz the same mesh will be 99.9994% reflective. With such a high reflectivity the fundamental bandpass feature would resemble a Dirac delta function, and measuring any signal would be nearly impossible (the power contained under a Dirac delta function is infinitely small). Similarly, if the reflectivity is 95% at 100 GHz, it will be roughly 52% at 1 THz and spectral selectivity will be very poor (finesse = 4.75). Therefore the wire-mesh mirror is only good for measurements over small spectral ranges, so a different mirror design is needed for truly broadband spectroscopy. To address this problem a new mirror concept will be presented in Chapter V that is based on the linear THz polarizers discussed in Chapter IV.

3.3.2. THz spectral scan setup and results

Proof-of-concept testing for the fast-scanning, tunable-frequency, THz FPI spectrum analyzer was taken on a single-frequency, coherent source at 530 GHz (a frequency multiplier from Virginia Diodes Inc. [29]). A narrow line-width, single frequency source was used for initial testing because it should demonstrate the frequency discrimination capability of the FPI. From Fabry-Perot theory, the FPI mirror separation (d) corresponds to a specific resonant transmission frequency; for 530 GHz it should be 283 μm. Since the mirror reflectivity was measured separately, the theoretical Q-factor (analogous to finesse) of the FPI is also known. The Q-factor is a metric commonly used to describe resonating cavities, it measures the ability of the cavity to resonate on a single

frequency, while rejecting others. It is calculated from the FWHM of the transmission resonance peak (Δf), and the center frequency of the peak (f_c): $Q = f_c/\Delta f$ [74]. The FPI mesh-mirrors with 175-μm period are seen in Fig. 31 to be ~98% reflective at 530 GHz (finesse = 155), and thus the bandpass features should have a spectral line-width (FWHM) of ~6.84 GHz; corresponding to an optical Q-factor of 77. So to summarize this experiment theoretically, the FPI data taken on the 530 GHz source should see the fundamental signal pulse at 283 μm plate separation with a Q-factor of 77, corresponding to a finesse of ~155 and a change in frequency (Δν) of 530 GHz. Higher order peaks should occur with every additional 283 μm of separation. Achieving these results would confirm that the FPI has very good frequency discrimination capabilities.

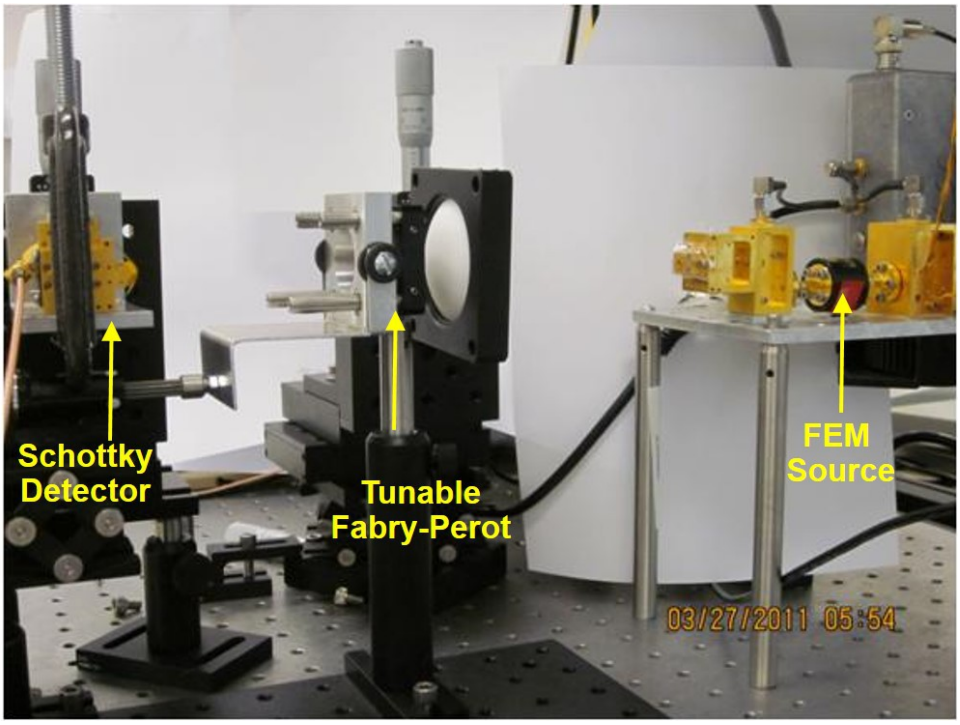

Figure 35: Experimental setup for the THz FPI spectrum analyzer. Here the 530 GHz source is visible, along with a lens used to focus signal into the FPI, the FPI, and a Schottky diode detector with excellent 530 GHz responsivity.

The experimental setup used for this data collection is shown in figure 35. The 530 GHz FEM (frequency extension module) source is on the right side of the setup, a 4-inch focal length Teflon lens was used to collimate the signal into the FPI, and the signal was then collected with a zero-bias Schottky diode detector. The Schottky diode was chosen for this measurement over a pyroelectric detector because it has much faster rise and fall times (ns vs. ms), and can therefore take data at a much faster rate. To accommodate this, the FEM was electronically chopped at 30 kHz (vs. a maximum of 10 Hz for a pyroelectric detector). With the fast detection scheme, this experiment could demonstrate not only the fast-scanning capability of the FPI, but also the accuracy of power vs. frequency measurements. Readings from the Schottky detector were measured with a standard lock-in amplifier and its output data was collected with a LabJack model U9 data acquisition module (DAQ) at its maximum sampling frequency of 6 kHz [75].

Both the linear actuator movement and the LabJack data collection were controlled within the MATLAB programming environment (the programming process is explained in detail in the next section). The theoretical Q-factor of 77, for this FPI, corresponds to a spatial Nyquist resolution of ~3.65 μm/sample. So for a 300 μm scan distance (this distance would guarantee measurement of a bandpass peak), the scan time would have to stay above 0.0137 seconds. However, to fully resolve the signature signature shape 3 samples are needed on the bandpass peak. At 6 kHz sampling this resolution (2.43 μm/sample) corresponds to a movement rate of ~15 mm/s if the scan is completed by a single sweep in one direction. The linear actuator was capable of meeting this speed requirement. Therefore, the theoretical minimum time required to resolve the

530 GHz peak through the FPI, with this criteria, is (300 μm)/(15 mm/s) = 0.02 seconds.

To start data collection the FPI was scanned at a very slow rate and high resolution to ensure that all spectral features were accurately captured by the data, the result is shown in Fig. 36. This scan time was 60 seconds and the spatial resolution was 0.75 μm. This first test proved to be a good illustration of the capabilities of the FPI system. The high resolution used fully resolved the features of the collected signal. The scan length (change in plate separation) was just under 500 μm and was taken over a plate separation that would collect two bandpass modes. By collecting two bandpass modes the accuracy of the passed wavelength vs. plate separation, and the Q-factor of the FPI could be determined.

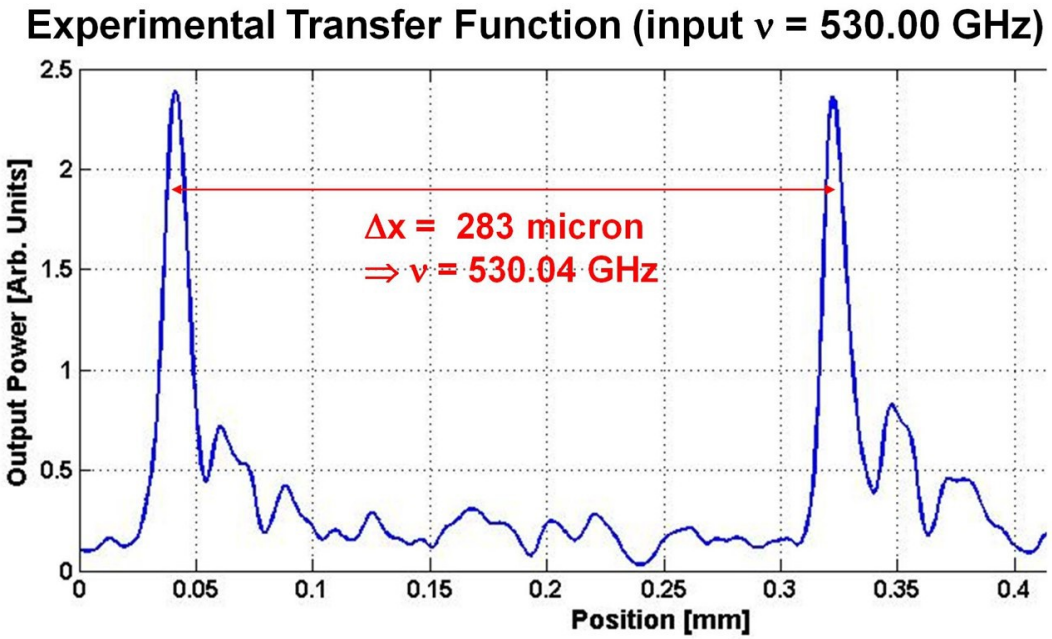

Figure 36: High resolution data from the fast-scanning FPI at 530 GHz. Shown here are two bandpass modes with the correct spacing between them.

The results in Fig. 36 show that the bandpass modes have exactly the correct separation for a 530 GHz signal, thus showing the accuracy of the FPI system, and this

was a very encouraging result. Unfortunately, the FWHM width of the bandpass modes was ~11.4 μm, this equates to a change in frequency of ~10.6 GHz. With a center frequency of 530 GHz, the calculated Q-factor is 50. This was a decent result, the frequency selectivity is quite narrow, but a Q-factor of 50 is only ~2/3 of the predicted value. The reason for this discrepancy was attributed to deficiencies with the FPI design highlighted in a previous section (page 66). The rock/lean problem described in that section makes the mirrors slightly off of parallel, and this would increase the number of frequencies that pass through the FPI, thus lowering the Q-factor. A lack of mirror flatness could have a similar effect. The noise and smaller peaks present in Fig. 36 were also attributed to these design problems. Nevertheless, this result proved the accuracy of the FPI, while illustrating its frequency selectivity capability.

The next experiment conducted was designed to test the speed with which an FPI scan could be made. This test is important because the faster the system can scan, the more practical it becomes for real-world use. The same experimental setup from the previous test was used, but the scan time was varied, and the mirrors scanned the same distance for every test, 500 μm, starting with 600 μm separation. In this test the DAQ was constantly sampling at 6 kHz, so the resolution of each scan will become lower, as scan time decreases. The scans started at 0.5 second scan time, and the time was decreased in subsequent scans until the FPI system could no longer detect the bandpass features reliably. Fig. 37 shows the results from this experiment where, once again, the bandpass features were measured to have the correct spatial separation. In these plots, the left most bandpass feature is the fundamental mode. The FPI mirrors did not quite

come into contact because of the leaning issue, so very small separation distances (< 150 μm) could not be measured, hence no transmission peak at the lowest separation (as predicted when plate separation = 0).

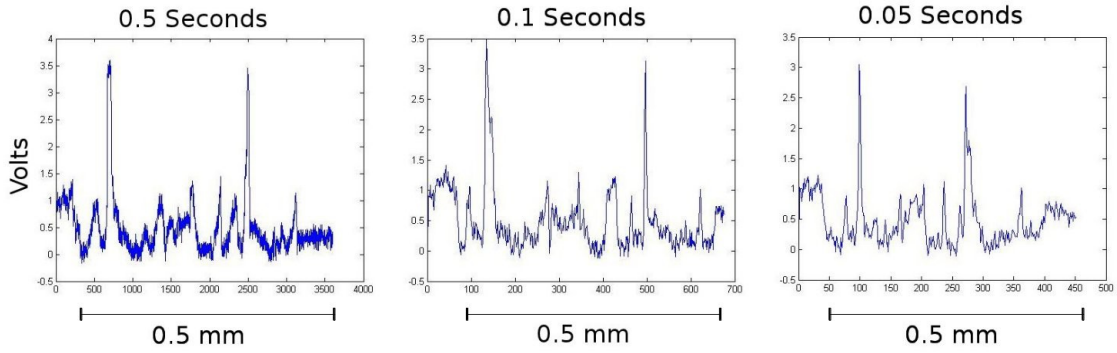

Figure 37: FPI scans at 530 GHz with varying scan time. All three scan times shown were capable of accurately measuring the FPI bandpass features.

With the scan rate at 6 kHz, the resolution of the first scan (0.5 s) was very high, 500 μm/3000 samples = 0.167 μm/sample. This evident in Fig. 37(a) where the line plot is noticeably more dense, and the collected bandpass features adhere closely to the airy function shape seen in Fig. 36. As the scan time decreased the resolution decreased because the sampling rate was unchanged: 500 μm/600 samples = 0.833 μm/sample for the 0.1 second scan (Fig. 37(b)) and 500 μm/300 samples = 1.67 μm/sample for the 0.05 second scan (Fig. 37(c)). Despite the decrease, all three scans remained above the previous criteria of 2.43 μm/sample, however the peaks became slightly less resolved as scan time decreased (exemplified by the lower peak intensity of the second mode in Fig. 37(c)). The airy function shape of the bandpass modes also started to become distorted (stretched and widened) as the resolution decreased. This is indicative of the decreasing scan time having a negative effect on FPI accuracy. 0.05 seconds represented a hardware-limited fast scan time, because at this scan rate the linear actuator began to slip,

thus yielding inconsistent results. As in the slow scan (Fig. 36), some out-of-band noise is present in the results, this is expected and attributed to the same mirror alignment problems discussed earlier.

Another important factor in these results is the rejection of out-of-band wavelengths. In both Figs. 36 and 37 the bandpass features are ~10 dB larger than the noise floor. The noise floor in this situation is not the true system physical noise, but rather the 530 GHz signal leaking through the FPI between bandpass features. Having the out-of-band wavelengths 10 dB lower than the desired wavelengths is very desirable and confirms that most of the collected power is from the desired frequencies in the FPI. An experimental value for the mirror reflectivity can also be backed out from this data, by solving the transmission function in Fig. 28 for F. Solving this, the reflectivity of the wire meshes is experimentally estimated at 60%, this is substantially different than the 98% measured values for each individual mesh, and shows how the rock/lean problem in this FPI design degraded the frequency selectivity. In other words, the mesh reflectivity isn't actually 60%, but idiosyncrasies in the FPI behavior makes it behave as though it is.

This behavior can be explained analytically by solving the Fabry-Perot airy function with error introduced (eq. 11). In these equations T = transmission, F is a constant dictated by the mirror reflectivity, L is the round trip path length between mirrors, and λ is the incoming wavelength. Nonparallel mirrors can be simply simulated analytically by summing many elemental Fabry-Perot airy functions with different cavity lengths [76]. For each discrete mirror separation (separation d), the FPI airy function can be numerically integrated from separation d to d+x. So if the mirrors are nonparallel by

50 μm (the FPI cavity is 50 μm wider on one side), this could be simulated by integrating from d to d+50 μm.

$$T = \frac{1}{(1 + F\sin^2(\delta/2))} \text{ where } \delta = 2\pi L/\lambda \text{ and } L = 2d + x \tag{11}$$

Similarly, if the radiation incident on the FPI is not collimated, the cavity will effectively be a different length to radiation that is not incident at normal incidence. This will change the wavelength that constructively interferes at certain points in the cavity. So to simulate a diverging (or converging) input signal the wavelength can be varied as T is calculated across the FPI mirrors.

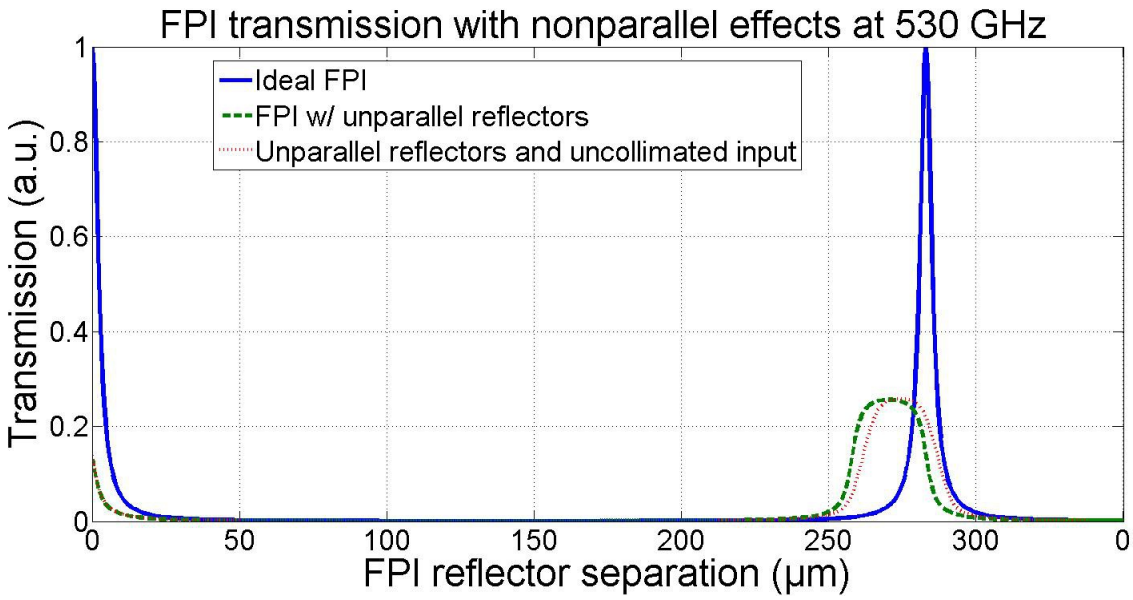

Figure 38: The analytical transmission through a Fabry-Perot with various geometric imperfections added. Here nonparallel FPI mirrors and an uncollimated input signal have been simulated.

The results from this analysis are shown in Fig. 38, and behave as expected. As the plates become nonparallel the transmission peaks begin to weaken, broaden, and there is a shift in center frequency. The weakening can be easily explained, because only a

small portion of the FPI is at the correct separation, so at other locations on the FPI mirrors the transmission is lower than 1 for the input frequency. This also causes the bandpass modes to broaden, as different sections of the FPI mirrors pass different center frequencies simultaneously. The shift in center frequency is related to the reference point of the plate separation. In this example the plate separation on the x-axis was referenced to the short side of the FPI cavity. So as the cavity length increases (due to being nonparallel) the bandpass feature will shift towards smaller wavelengths (because when the x-axis is centered on a small wavelength, longer wavelengths will also be transmitted).

The calculation for an uncollimated input is similar, as the input becomes more and more divergent (or convergent), the bandpass feature begins to broaden slightly more. The is again expected because a beam entering the cavity at an angle will see a different cavity length due to simple trigonometry, thus changing the constructive interference frequency. Error can also be introduced into the FPI by having the radiation incident at some angle other than normal, however this wasn't shown because it simply moves the location of the bandpass feature, no broadening occurs, analytically. The pulse broadening shown here with misalignment of the FPI mirrors, or an uncollimated input signal, is likely responsible for the lower-than-predicted resolution of the FPI.

These experimental results show that the FPI is a practical and high-speed device for taking spectral data. Extrapolating these results out to the 1.5 mm mirror separation, necessary to cover the entire THz range, a scan could be completed in only 0.3 seconds. However, it is important to note that no Schottky diode detector has bandwidth large

enough to take such a scan. So in real world scenarios, either a slower pyroelectric detector must be used, or several Schottky diode detectors. Pyroelectric detectors are very slow, so they would lengthen THz spectral scans into hundreds of seconds, yet this scan time is still considerably quicker than current frequency-domain scanning systems and the setup time is minimal. The FPI components are is simple as well, so it would cost should be low. Using several Schottky diode detectors may be the best way to proceed with the FPI systems in the future, because multiple scans could be taken in a matter of 1 or 2 seconds (1 scan for each detector, mounted on a wheel or similar component). Schottky diode detectors also have another advantage, which is virtually zero responsivity at out-of-band wavelengths; this would cut down on noise in the FPI scans, thus producing more accurate results.

3.3.2.1. Fabry-Perot software development

In order to operate the FPI spectrum analyzer, software had to be written to control the movement of the mirrors, and to control the data collection from a lock-in amplifier. The MATLAB programming environment was used to complete this task because it is a high-level language, thus making programming an easy task relative to lower level languages such as C. The first task in creating this software was programming the Zaber linear actuators so the FPI mirrors would move as desired. After the mirror movement was completed, the LabJack DAQ was programmed into the same code to manage the data collection. All of the code used for data collection is included in Appendix B.

The Zaber linear actuator uses a stepper motor that is controlled by 6-byte data packets transmitted through an RS-232 cable. No pre-written MATLAB code existed from the manufacturer for these motors, so the code written was completely original and done specifically for this work. The first task in programming the motor was figuring out how to communicate individual commands to the controller, through the 6-byte data packets; an example packet is: [0 60 0 0 0 0]. This shows the 6 individual 8-bit numbers in the packet. The first number selects the linear actuator (multiple actuators can be used with one controller). If only one actuator is connected to the controller, then 0 can be used. The second number is the command byte, in this example 60 is shown. This command tells the controller to report the linear actuator position. The next four numbers are the data bytes, in little-endian notation. For a read command like the one shown in the example, all zeros are used. Other commands, like move to position "X," are more complicated. The input position for such a command must be converted first into the step number of the motor, and then into little-endian format.

$$[byte1, byte2, byte3, byte4] = entryToBits(576020) \rightarrow [20, 202, 8, 0] \quad (1)$$

$$[number] = bitsToEntry(8, 12, 3, 4) \rightarrow [67308552] \quad (2)$$

So the first code that was written was two functions (Funcs. 1,2) to convert any regular number into little-endian notation, and the reverse. As seen from the above equations, entryToBits() converts some number into the correct corresponding 4 bytes, and bitsToEntry() converts 4 bytes into the correct corresponding number. The other important aspect of converting a user input into the correct notation was converting from a common unit (such as mm) to the number of linear actuator steps. For example, when

moving the linear actuator to position 6 mm (for the smaller NA08B30), the corresponding entry number for entryToBits is 6 mm/.0000925 mm/step = 64865 steps. This is because the step size of the Zaber NA08B30 is 0.0000925 mm. Giving a movement velocity also works in a very similar way, except instead of dividing the number by step size, the number is divided by minimum motor velocity. For example, 6 mm/s corresponds to 6718.9 steps/s because the minimum velocity of the NA08B30 is 0.000893 mm/s. These two functions were critically important and used in all of the forthcoming code, as they convert any user input into the correct format for the Zaber controller to read.

With these two functions in hand the scanning software was written using a series of movement and movement speed commands. For the slow scan done in Fig. 36 The function slowScan() was written and a function called oscillate5() was written for the faster scans. These functions are identical in how the linear actuator movement is controlled, the only differences are relate to the DAQ programming. The DAQ sampled at 6 kHz in oscillate5() and 3 Hz in slowScan(). An example call for one of these functions is [transmission] = oscillate5(1, 29.5, 0.5, 0.5). The first number in this call is the motor selection (NA14C30 or NA08B30), the second number is the starting point. The linear actuator has 30 mm travel, so 29.5 mm puts the actuator 0.5 mm from the end of travel, where the stationary FPI mirror was located. The third number is the scan time, 0.5 seconds here. The fourth number is the distance to be scanned, 0.5 mm here. This function call is what was used for Fig. 37(a).

The movement functions begin by calculating the movement speed necessary to

cover the distance (0.5 mm in this example) in the allotted time (0.5 s in this example), and then turning the movement parameters into the 4-byte data packets. Then the linear actuator is set to a high movement speed of 25 mm/s and moved to 2/3 of the initial starting position, the “pre-start” position (Fig. 39(a)). From Design 1: Sliding bushing-based Fabry-Perot plates with copper mesh mirrors, the early FPI designs had a rocking problem with the tunable mirror plate. Moving short of the initial starting position first ensured that there was no change in the rock angle during the scan. This process is better explained with the illustration in Fig. 39. Obviously, the FPI mirrors would ideally be parallel, but having a constant lean is better than having it change during the scan, because the overall change in plate separation will be more accurate. This part of the code was made for the first FPI design that had the rocking problem. After this the actuator is moved to the starting position (Fig. 39(b)).

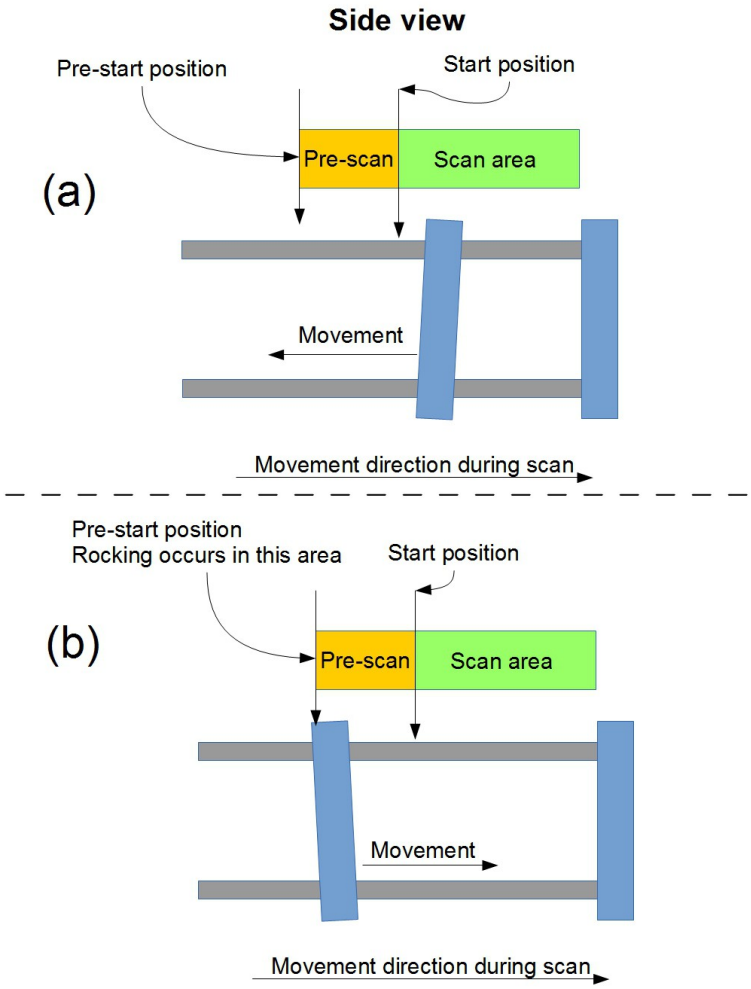

Figure 39: The angle of the tunable mirror can change depending on the movement direction. Moving the mirror to a pre-start position ensures that when the scan starts, the mirror angle does not change. This way the mirror position information is more accurate.

When the tunable mirror was in the start position the movement speed is then changed to the correct speed, dictated by scan distance/scan time. Then the linear actuator moves the tunable mirror the distance specified in the function input, toward the stationary plate; this is the final movement in a single FPI spectrum analyzer scan. The DAQ data collection begins the moment (next line of code) the final FPI movement is called. The data collection lasts the same amount of time as the scan time specified in the

function input (so 0.5 s for the example above). Assuming the acceleration and deceleration of the linear actuators is near instantaneous, this method of data collection gives an accurate sample vs. position, exemplified by the data in Figs. 36 and 37. Unlike the Zaber linear actuators, the LabJack DAQ had MATLAB libraries available from the manufacturer. So when either scanning function was called, the DAQ would be initialized near the beginning of the code, and then sampling could be easily initiated.

An alternative method of scanning the FPI would involve having the linear actuator controller report its position for each sample. This would be ideal, but this was far to slow to do a high-speed scan. Sending a position query to the controller took ~0.25 seconds and was found to be unreliable (sometimes the position simply wasn't reported). So using the timing based approach was more practical with this hardware combination.

A particular point was made when programming for the FPI to make all code function based. Because of this the scanning functions could easily be set inside of another script or function and called many times. As an illustration of this, a simple graphical-user-interface (GUI) was made to control the Zaber linear actuator in MATLAB. A screenshot of this GUI is shown in Fig. 40, and the code for this GUI is now featured on the Zaber Technologies Inc. website [77].

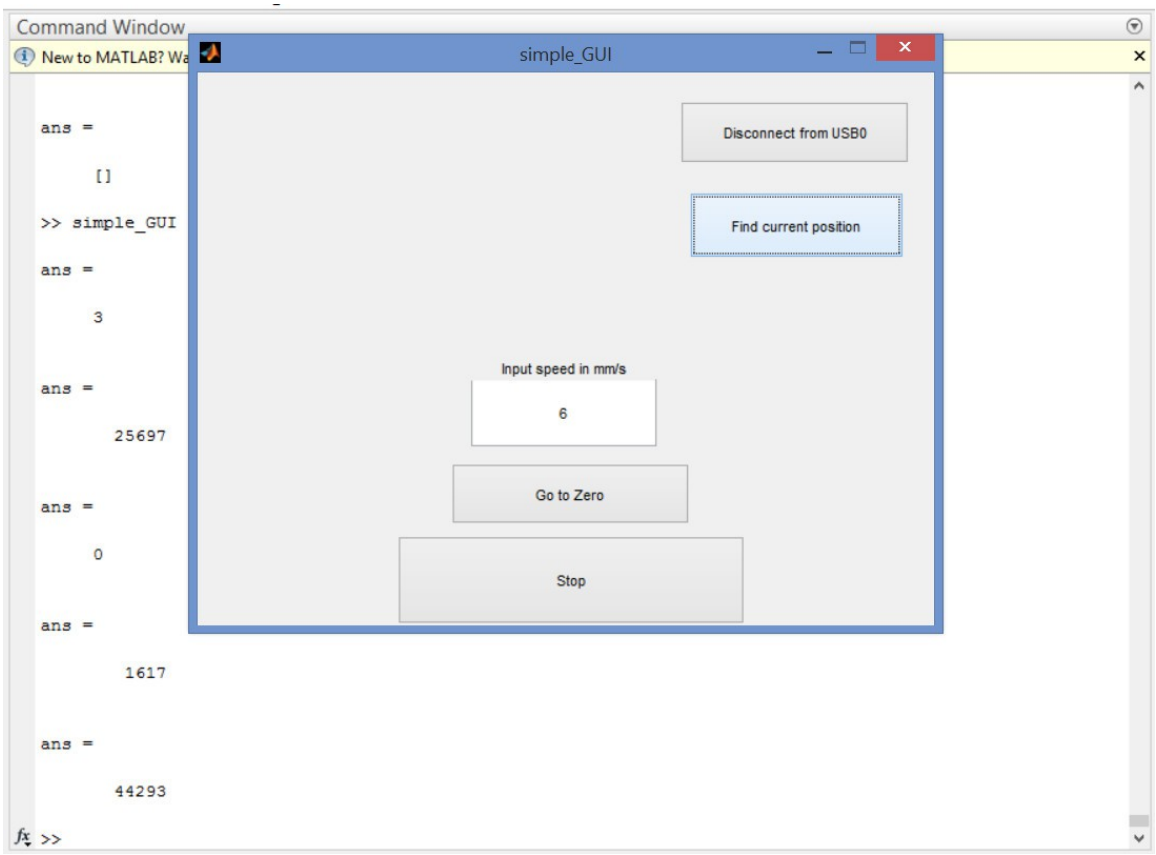

Figure 40: A simple GUI created to control the Zaber linear actuators. Inputs are converted into data packets using the function-based code. The "Find current position" button was pushed in this screenshot and the position of 44293 is displayed in the command window. This position is in motor steps and corresponds to 16.87 mm.

3.4. A discussion of the Fabry-Perot, improvements, and future work

The FPI represents an important new approach to THz spectrum analysis. Currently there are three primary methods of measuring the THz spectrum of a PC switch: (1) time-domain spectroscopy (TDS), (2) Fourier transform spectroscopy, and (3) spot frequency measurements with calibrated detectors (such as was done in Chapter II). All three methods have advantages and disadvantages when compared to each other. TDS systems simply create a cross-correlation between an ultrafast laser pulse and a THz

pulse, this works exactly like cross-correlation in signal processing [78]. The result from this process is an accurate recreation of the THz pulse in the time domain (fig. 41(a)). Spectral information is then found by Fourier transformation using Wiener's theorem (fig. 41(b)) [79]. TDS systems do a good job of obtaining accurate spectral information from a THz source but they are extremely sensitive instruments that can lack practicality for several reasons. First, TDS systems require extensive setup time. After inserting a PC switch into such a system a very careful alignment must be performed, this can take hours to complete. Second, TDS systems are very expensive and a system in which the source can be easily "swapped" out must be custom built on an optical table. This requires a trained engineer or physicist, an ultrafast laser, and many expensive optical components. The third and final reason TDS systems can be inadequate for some applications relates to THz reflective spectroscopy; the THz pulse path length in a TDS system must be very precise. In a real world scenario the THz path length to the target will be constantly changing, jeopardizing the alignment of the TDS system for every sample.

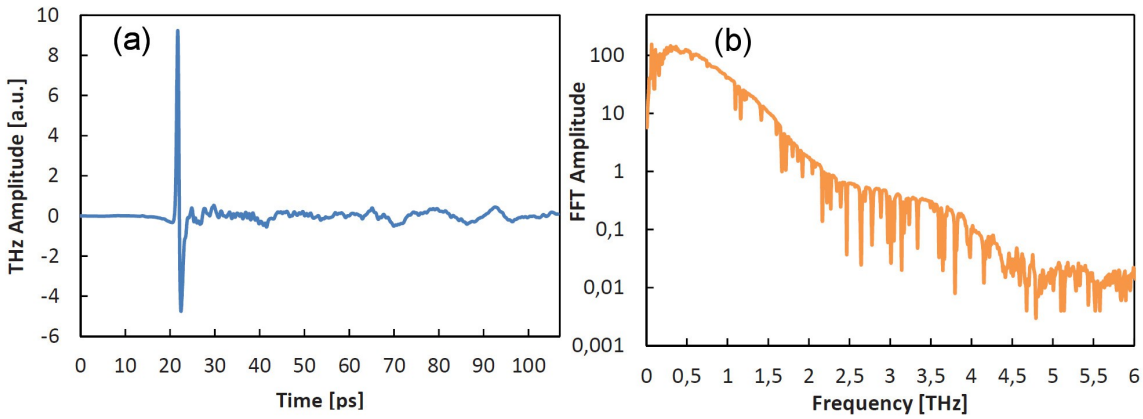

Figure 41: Example TDS results from a Menlo Systems commercial system. (a) a measured THz pulse. (b) The THz spectrum calculated from the time-domain pulse [79].

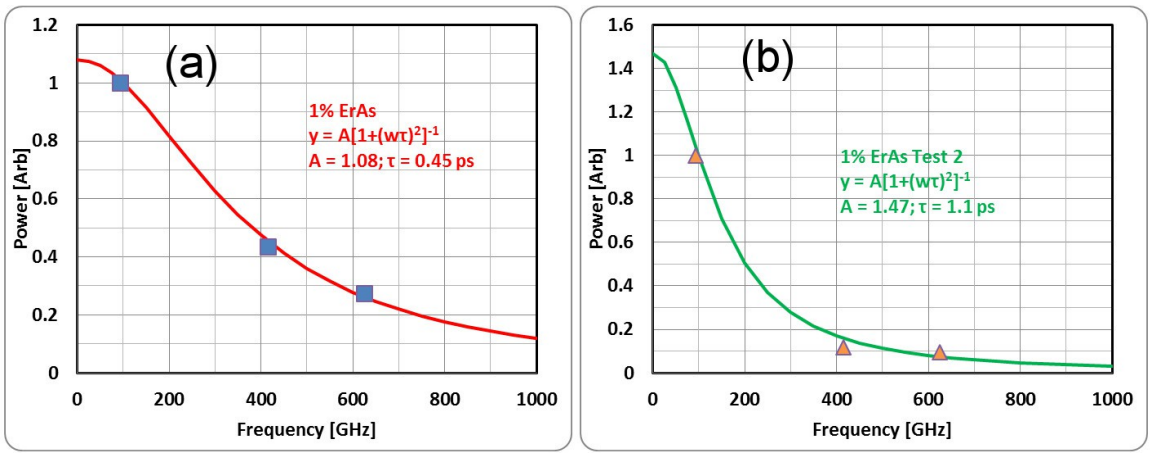

Figure 42: Bandwidth calculations for 1% Er bearing ErAs:GaAs PC switches using Discrete frequency measurements for spectral estimation. (a) is the measurements taken during the intial discovery of extrinsic PC in ErAs:GaAs and (b) is a measurement taken for [63]. The difference between these two measurements show that this method of spectral analysis lacks in precision compared to TDS systems.

Fourier transform spectroscopy (FTIR) is a historical, common technique for THz characterization and is capable of measuring from THz spectrum through visible spectrum. The problem with this technique is that the dynamic range is poor below ~3 THz, several orders of magnitude worse than TDS systems. This is largely due to the thermal detectors used in these systems, and this also decreases the dynamic range of the system even further when one or more components in the system are hot [80]. Lower dynamic range also virtually eliminates this technique from reflective spectroscopy applications, because the required dynamic range will scale non-linearly with stand-off distance (radar-range equation, signal power drops by $1/r^4$). Last, the resolution from Fourier transform spectroscopy is poor compared to other spectroscopy techniques (>3 GHz) [80].

Spectral reconstruction using spot frequency measurements is much simpler than TDS or FTIR, but also more limited. This method is good for getting bandwidth

estimates from a PC switch because it doesn't require precise optical table setups like a TDS system, and it is inexpensive because the only components needed are common optics and direct, band-limited detectors. Each detector is placed in the THz path sequentially and at approximately equal distance from the source and the output signal is recorded. However this method is not capable of doing any type of spectroscopy because discrete frequency spectral measurements are extremely low resolution. For example, in Chapter II only three data points could be taken (because there was only three band-limited detectors). This is enough to estimate the bandwidth of the PC switch, but no other spectral information can be garnered (such as spectral signatures). Another downside is that experimental setup is tedious, as every detector must be sequentially placed in the same location. The precision of this method is questionable as well, as mentioned earlier and shown in Fig. 42. Experimental inconsistency[9] can make measurements on identical devices different by 50% or more, although the change in laser power between measurements could also be partially responsible [5], [63].

To conclude this section several possible improvements for the FPI are be suggested as future work. The first of which related to detectors. The best FPI performance should come from use with band-limited, waveguide-mounted, zero-bias Schottky diode detectors, rather than more broadband detectors such as bolometers and pyroelectrics. This statement is justified by two facts: The fast rise and fall times available in zero-bias Schottky diode detectors makes fast scans (<1 s) possible, and the

9 Experimental error for spot frequency measurements could be introduced through poor laser alignment on the PC switch, detector alignment inconsistencies, and changes in laser performance (shortly after the data in Fig. 42(b) was taken the laser failed, suggesting it may have not been performing optimally).

sharp wave-guide low-frequency cutoff of these detectors will help reject unwanted frequencies from being measured. In chapter V (page 136) it will be shown that higher frequency modes should have little effect on measured power, but very low frequencies were not discussed in great detail. For a small mirror separation, say 100 μm, very low frequencies will not be rejected by destructive interference, but only by the mirror reflectivity. So without some kind of high-pass filter, high frequency measurements could be corrupted by low-frequency leak-through. The sharp low-frequency cutoff presented by waveguides inherently creates this shortpass filter. So a detector "wheel" of 3 or 4 Schottky diode detectors covering the desired spectrum would allow scans to be accomplished in a matter of seconds, with greater accuracy.

Another improvement could possibly be made using cleverly designed optics. Shown in [81], [82], and [83], it is possible to make diffractive THz optics that only focus wavelengths chosen by the lens designer onto the focal point. An example of this is shown in Fig 43(a), this lens is called a "superzone" lens because each element (or zone) is designed for an individual wavelength [81]. So it should be possible to fabricate THz lenses (out of materials like Teflon or polyethylene) that focus only desired frequencies into the detector, after the signal passes through the FPI. For example, if the intention was to detect the THz signature of Lactose monohydrate at 532 GHz, a lens could be made specifically to focus wavelengths from 500 to 550 GHz.

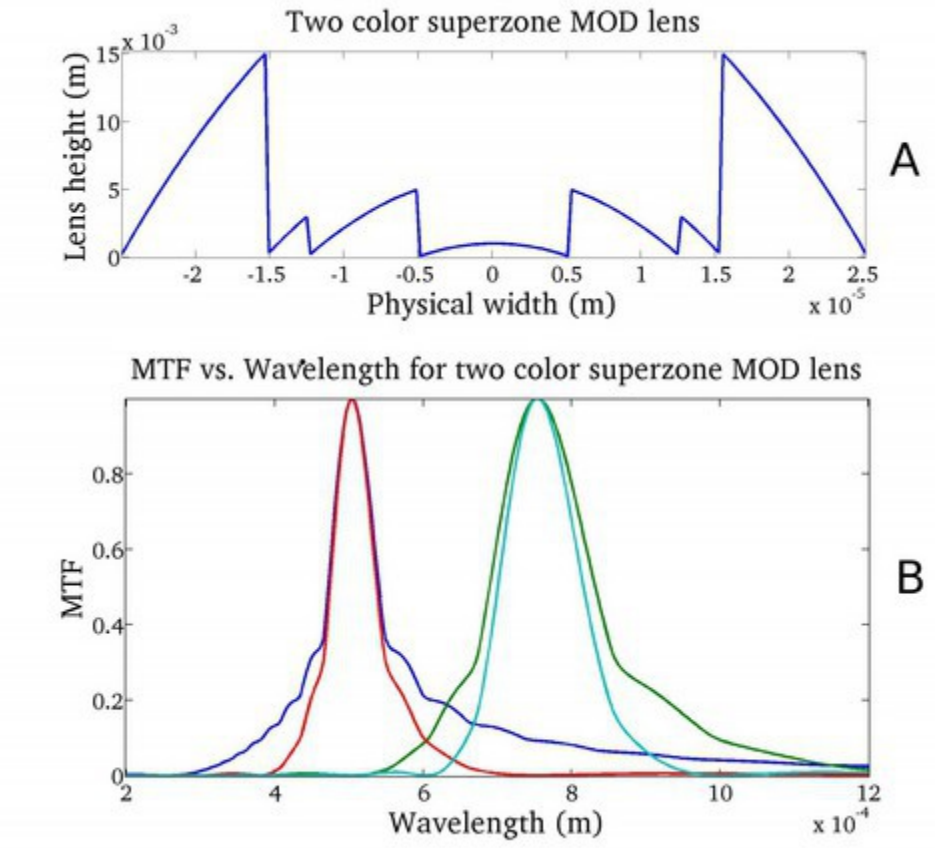

Figure 43: An example of a "superzone" diffractive lens. The elements of this lens are designed to focus only 400 and 600 GHz (750 μm and 500 μm) onto the focal point. Other frequencies will focus elsewhere. (a) is a cross-sectional view of the lens profile and (b) is the MTF of each lens element vs. wavelength.

Fig. 43(b) shows the normalized modulation transfer function (MTF), a common optical metric for spatial resolution, of wavelengths propagated through this lens design (the area under the MTF curve was summed for each wavelength). Each plot on Fig. 43(b) is for a different lens element in Fig. 43(a). It is apparent that this lens was designed to focus 400 and 600 GHz at the design focal length. So if the detector was placed at the focal point of the lens, it would detect these frequencies more efficiently. The other frequencies in the graph are focused, of course, but at different focal points.

The design possibilities of this lens type are many, so they could be designed to enhance the detection of any portion of the THz band. For this work an example of a THz superzone diffractive lens was fabricated and presented at an international conference [83] and is shown in Fig 44.

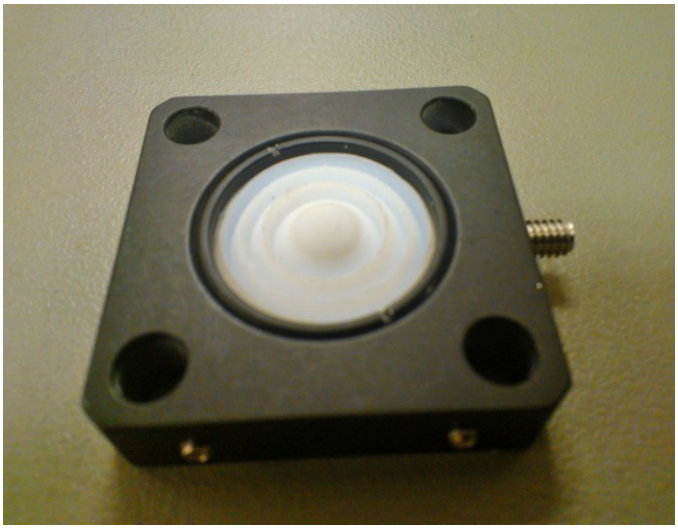

Figure 44: An example of a simple superzone diffractive THz lens designed to focus 200, 400, 600, and 800 GHz at 2 inches.

The final suggested improvement for the FPI spectrum analyzer is improving the mirrors. Wire-mesh mirrors worked will for this proof-of-concept design, but the change in reflectivity with frequency proved problematic. The useful frequency band of the FPI is limited by this factor. After this FPI concept was presented to the THz community in 2011, another research group used a small metallic coating to achieve a mirror with much smaller reflectivity change, in 2013 [84]. This was a step in the right right direction, but in chapter V another, more flexible approach is presented, using THz polarizers for the FPI mirrors. Polarizing FPI mirrors are promising because their reflectivity can be easily tuned for maximum resolution, or maximum power. But first, in Chapter IV, new THz polarizers will be discussed that were eventually used for the FPI mirrors because these polarizers were exciting in their own right, and led to several publications.

4. Structured-Surface-plasmon enhanced THz polarizers and devices

Chapter III explained and demonstrated an exciting new THz spectrum analyzer based on a tunable, fast-scanning Fabry-Perot interferometer (FPI) [70]. This is a significant advancement for reducing the cost of accurately measuring THz sources like those presented in Chapter II, and for the possible development of reflective spectroscopy systems. In the tests from Chapter III, the THz FPI showed a good ability to discriminate and accurately measure different frequencies. The FPI is also easy to setup, align, and can take scans very quickly (<1 s). However there is one notable deficiency: the FPI mirrors used are relatively narrow-band so the entire THz spectrum can not be scanned. So at the end of Chapter III FPI mirrors based on THz polarizers were presented as a concept. Polarizers should make excellent mirrors for the FPI; they are far less frequency dependent than wire meshes, and can be adjusted to maximize frequency selectivity or power. This chapter focuses on the work done to develop better THz polarizers that eventually could be used for the FPI spectrum analyzer, and this fits the research plan shown in previous chapters, and below (Fig. 45).

The dashed box in the research plan provides a graphical illustration of what this chapter will cover. First the current state-of-the-art in THz polarizers will be discussed, with some common metrics, and common problems. This will be followed by a discussion of surface-plasmon-like behavior that was seen in polarizer simulations, as this work searched for the best polarizer design. Then this behavior will be rigorously studied

experimentally with different wire-grid polarizer designs. This includes changes to several physical characteristics of the polarizers, including the percentage of metal in the wire-grid unit cell (fill-factor (FF)), the period of the unit cell, and replacing a single polarizer wire with several smaller wires. Finally, this chapter will end with a summary of the new surface-plasmon-like effects in polarizers, and how they could be used to benefit other devices in addition to polarizers.

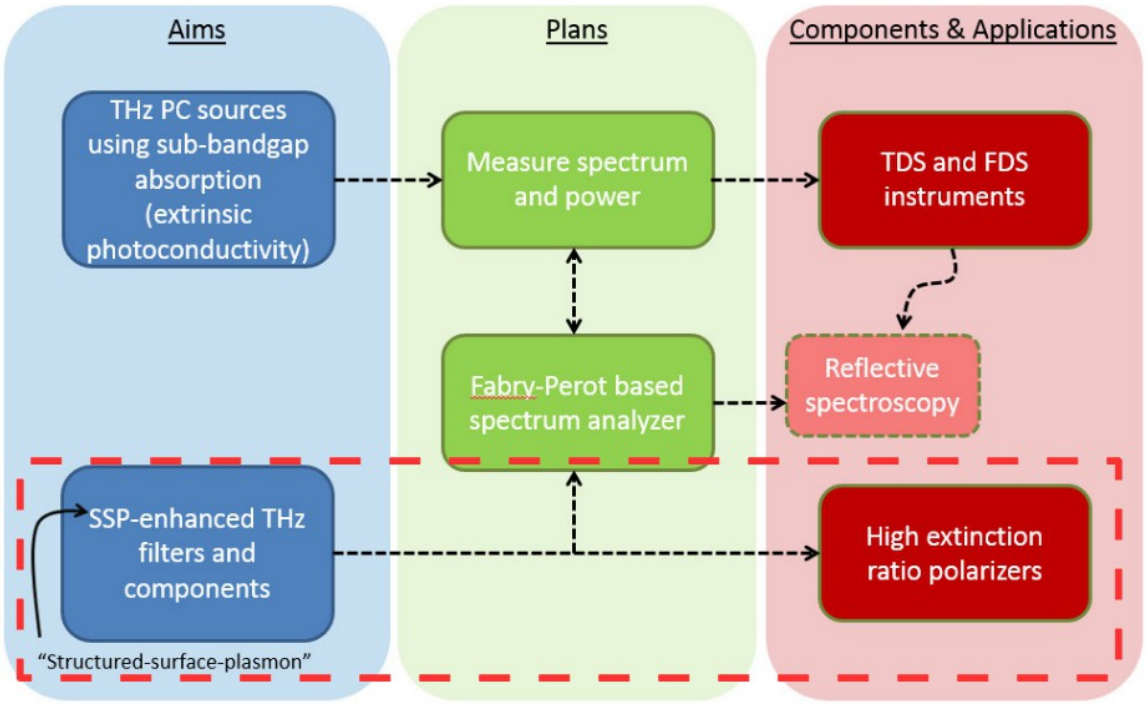

Figure 45: Research outline for this work. This chapter will focus on the new plasmon-like effects discovered during this research. This effect improves the performance of the THz polarizer dramatically. Eventually, in Chapter V the polarizers will be used to improve the THz FPI from Chapter III.

4.1. Current state of the art in THz polarizers: Free-standing wire-grids and structured surface plasmons

To find the best polarizers for the THz FPI spectrum analyzer, current commercially available polarizer designs were investigated. These commercial THz linear polarizers are usually composed of metal wires that have been stretched across some open aperture to create a free-standing wire-grid (Fig. 46) [85]–[87]. Their performance is adequate for many applications with up to 39 dB of attenuation in the parallel-polarization at ~500 GHz, and the transmission through the polarizers is nearly 100% in S-polarization. However, there are many different polarizer designs available and the advantages of each is unclear. The size and period of the polarizer wires is varied across many different designs. Sometimes polarizers with smaller periods perform better than others, and sometimes not. The same applies for polarizer wire size. For example, the polarizer with the most parallel-polarization rejection across the THz band in [85] has 10 μm diameter wires, but some other 10 μm wire designs are inferior to designs with 20 μm diameter wires. So choosing the best polarizer is not straightforward.

Figure 46: A typical free-standing wire-grid THz polarizer [85]. These have decent performance but are very expensive and fragile.

Furthermore, there are more practical problems with the standard free-standing wire-grid polarizers. First, they are not very capable of blocking signal as frequency increases. At 1 THz the best free standing wire-grid has an extinction ratio of only ~33 dB, and as frequency rises this number continues to degrade [85]. The free-standing wire-grids are also quite fragile, as the wires are usually only tens of microns thick and wide, and have no substrate to support them. So rough handling by the user can destroy the polarizer. Another problem is that they are quite difficult to fabricate; the wires must run parallel to each other, maintain perfect planarity, and are separated by only tens of microns. This makes the fabrication, and consequently purchasing price quite high.

Because of this, fabricating substrate-based wire-grid polarizers in house was a more cost-effective option. A modest cleanroom was available to fabricate simple devices using photolithographic techniques developed for the microelectronics industry. Fabricated polarizers would be much less expensive because the materials that comprise the polarizers are inexpensive. For example, the single-crystal-quartz substrate materials used in this work cost less than $20 for 2-inch diameter. The cost of the metal wires that comprise the polarizer was also negligible because cheap metals could be used, such as aluminum. Additionally, the amount of metal used per polarizer is very small (a few grams). With this decision, the next step was to decide on the polarizer dimensions.

A 2-inch diameter would be adequate for the polarizer; this diameter is small enough to handle easily, but large enough to easily encompass the beam-waist of an incoming THz signal (assuming a spot size of ~1 cm, typical for many systems). The diameter was a pragmatic decision, but choosing the other critical polarizer dimension

(period and wire-width) was not as obvious. Polarizers are designed to discriminate a single linear polarization, so it was desirable to achieve maximum rejection of signal in the parallel-polarization, but transmit most in perpendicular-polarization.

To determine which period and wire-width was desirable, a study was performed on the literature of linear THz polarizers and optical gratings, and an interesting phenomenon was found. The literature shows that significant signal could pass through periodic arrays (such as a polarizer) with features that were considerably smaller than the wavelength of the incoming signal (hole sizes as little as 1% of the wavelength). Examples of this are abundant in the visible and near-IR regions, where surface plasmon polaritons have been utilized to create extraordinary optical transmission (EOT) through sub-wavelength features [88]. EOT is simply when more radiation is transmitting through an aperture than geometric optics would predict. This work was also extended to the THz region on substrate based polarizers. Some of the THz devices that exhibited EOT include sub-wavelength triangular grating structures (with a period of a few microns) [89], [90], sub-wavelength binary optics to collimate THz laser beams [91], and low period (a few microns) THz polarizers [92]. This was exciting because while perpendicular-polarized signal still passed through the polarizer with little loss, P-polarized signal was even more strongly rejected than normal.

This EOT phenomenon was attributed to “spoof” or “structured-surface plasmons” (SSP). The SSP is very similar to the traditional surface-plasmon polariton in its behavior, but not strictly the same physical effect. Surface-plasmon polaritons are electromagnetic surface waves that can form at a grated dielectric-to-metal interface if

high frequency light (close to the metal plasma frequency) wave is incident perpendicular to the interface. The surface wave is confined primarily to the interface. But if the period of the grated surface matches the wave vector of the surface plasmon, the surface wave can be coupled back into free space on the opposite side [88]. This means that surface-plasmon polaritons can enable EOT in small metallic gratings or arrays. However as the frequency of the incoming light decreases, the propagation constant of the plasmon along the interface decreases, and at frequencies well below the near-IR, surface-plasmon-polaritons are not well confined (they simply disperse) [93]. So at THz frequencies (much lower than near-IR), surface-plasmon polaritons cannot be generated efficiently.

This is where the SSP terminology comes from. THz radiation can experience strong EOT effects when propagated through extreme sub-wavelength arrays, much like visible and near-IR light does because of surface-plasmons. Yet, surface-plasmon-polaritons cannot physically be responsible. So the SSP name was invented to label a phenomenon that displays behavior similar to that seen with true surface-plasmons.

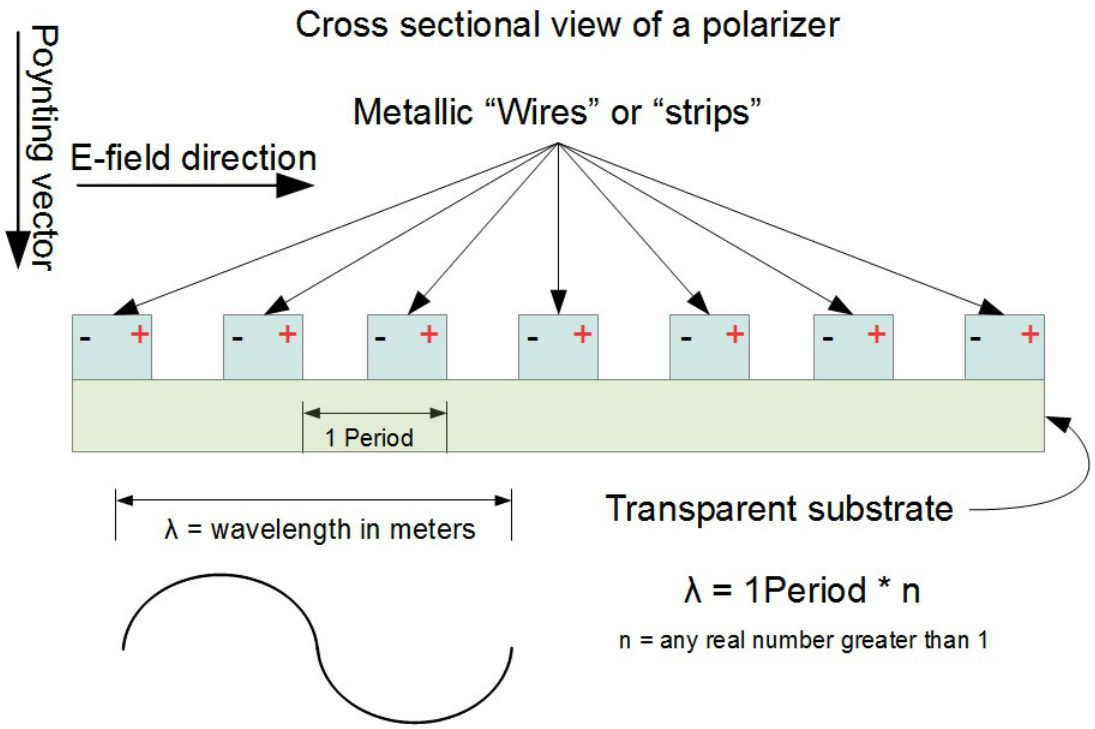

Figure 47: An example of a sub-wavelength period THz polarizer that utilizes SSP enhancements. The oscillating dipoles created on each metal strip enable EOT.

To continue this research it was decided to try to utilize SSP enhanced polarizers for the FPI mirrors, a reasonable possibility if the polarizers are custom fabricated. SSPs are strongly reliant on device geometry: like plasmons, a metallic grid of sub-wavelength periodic apertures in a metal sheet will support SSPs. And sub-wavelength polarizer designs have such a geometry. The physical basis behind the SSP effect is that incoming S-polarized waves create oscillating surface charges on the polarizer wires, which concentrate charge at the gap edges (the sub-wavelength apertures in this case), creating oscillating dipoles across the gaps. When the gaps are made very narrow, the electromagnetic energy is concentrated inside them and radiated efficiently out the other side, thus creating EOT. This is shown schematically in Fig. 47.

4.2. Applying SSPs to the simple substrate based polarizer

The earlier results in the literature suggested that maximizing EOT through sub-wavelength gratings also increases the extinction ratio in transmission [e_T = S-polarized transmission (dB) – P-polarized transmission (dB), where S = perpendicular and P = parallel] because the EOT maintains high S-polarization transmission, while reducing the P-transmission because of the smaller polarizer features. So to find a promising polarizer geometry that could be fabricated (the fabrication equipment was limited to 2 μm resolution), full-wave finite-element simulations were performed using High Frequency Structure Simulator (HFSS) [94]. The goal of the simulations was to find the polarizer geometry that maximized e_T, while still keeping S-transmission at an acceptable level (> -3 dB would be preferred).

The first parameter studied in the simulations was the polarizer period (L in Fig. 48(a)), especially its effect on e_T. After this the next parameter investigated was the wire or strip width, without changing period. This means that the percentage of metal in the wire-grid unit cell would increase as the strip width increases, a quantity referred to as fill-factor (FF). FF is given by W/L in Fig. 48(a), so if a polarizer has a 50 μm wide metal strip and a 100 μm period, the FF is 50%. In the previous literature the FF of a polarizer had not been rigorously studied with simulations and experiments. Naturally, one would expect the S-transmission to decrease according to geometric optics as FF is increased; however, simulations would better tell how FF effects S- and P- transmission together, and therefore the effect on e_T.

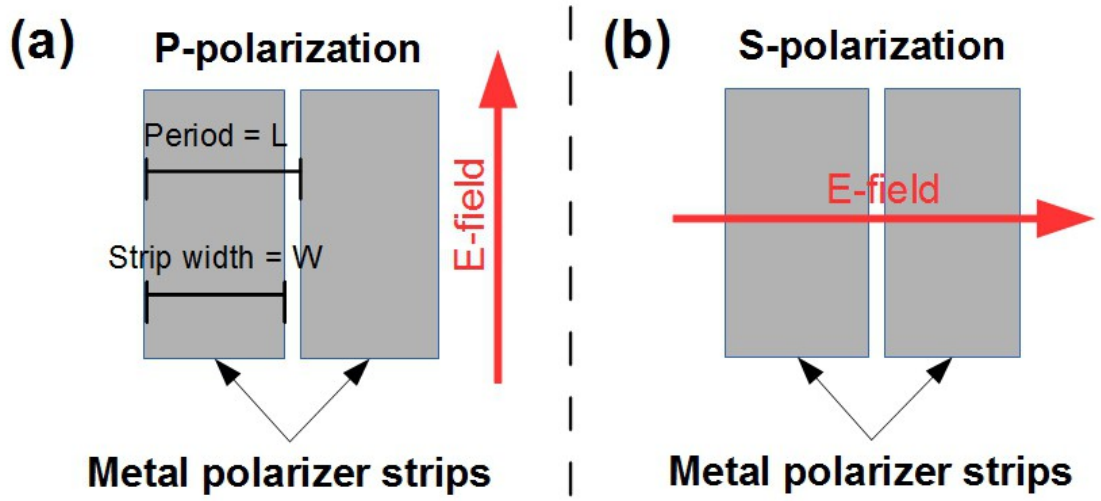

Figure 48: S- and P- polarization definitions. This figure is shown again here because it helps define the polarizer period (L) and strip width (w). This is important for understanding the polarizer naming convention used here.

The HFSS simulations were carried out with a single unit cell of the polarizer, as in Fig. 48, and periodic boundary conditions were used to emulate the effect of the unit cell repeating infinitely in both directions. THz signal was propagated perpendicular to the substrate using Floquet ports, which mimics an incoming plane wave with a single linear polarization. To match the frequency range that could be measured experimentally, the simulations were conducted from 200 GHz to 1 THz. Next the polarizer substrate was picked, with an inexpensive substrate material being very desirable. So initially polycarbonate was chosen for the substrate, which is a plastic that exhibits excellent transparency at millimeter wave (MMW) and low THz frequencies (< 500 GHz). However, as frequency increases the absorptive losses in a typical 1.5 mm thick polycarbonate substrate increases to well above 3 dB [94], so eventually the polycarbonate substrate was replaced with Z-cut single-crystal quartz. Z-cut-quartz substrates cost significantly more than polycarbonate but exhibit virtually no absorption

across the entire experimental spectrum in this work (a claim that will be later confirmed). Quartz was also a good material because it could be obtained with extremely flat, optically polished surfaces, and is chemically inert. The thickness of the quartz substrate was chosen to be 0.5 mm because that provides physical durability during fabrication and characterization.

The metal chosen to comprise the polarizer strips was aluminum because it is inexpensive and adheres well to quartz, an important factor for the following fabrication. Aluminum also exhibits good electrical conductivity, although not as high as gold or silver, but the price is far lower. The thickness of the metal was set at 2000 Å, an easy thickness to obtain by thermal evaporation. To ensure the aluminum and quartz absorptive and reflective losses were modeled accurately at THz frequencies, look-up tables were used to enter the correct complex dielectric function [95]. For aluminum the metal dielectric function is based on the Drudian model with a momentum relaxation time of $\tau = 10^{-14}$ s. Early simulations based on polycarbonate substrates used experimental spectrometer data to find the correct dielectric function.

For all simulations and experiments conducted the polarizers were given a compact naming convention that was based on the width of the metal strip (W) and the polarizer period (L) as defined in Fig. 48(a). For example, a 50% FF polarizer with W = 50 μm and L = 100 μm would be labeled 50x100 μm, and the FF is simply W/L. The first simulations, to study the effect of changing the polarizer period on extinction ratio, were done with 10x20 μm, 20x40 μm, 40x80 μm, and 80x160 μm polarizers. Three different frequency points were simulated to show how the extinction ratio changes: 500,

600, and 700 GHz. At these frequencies all four polarizer designs have sub-wavelength period, and the simulations could be tested experimentally. The results from these simulations are shown graphically in Fig. 49.

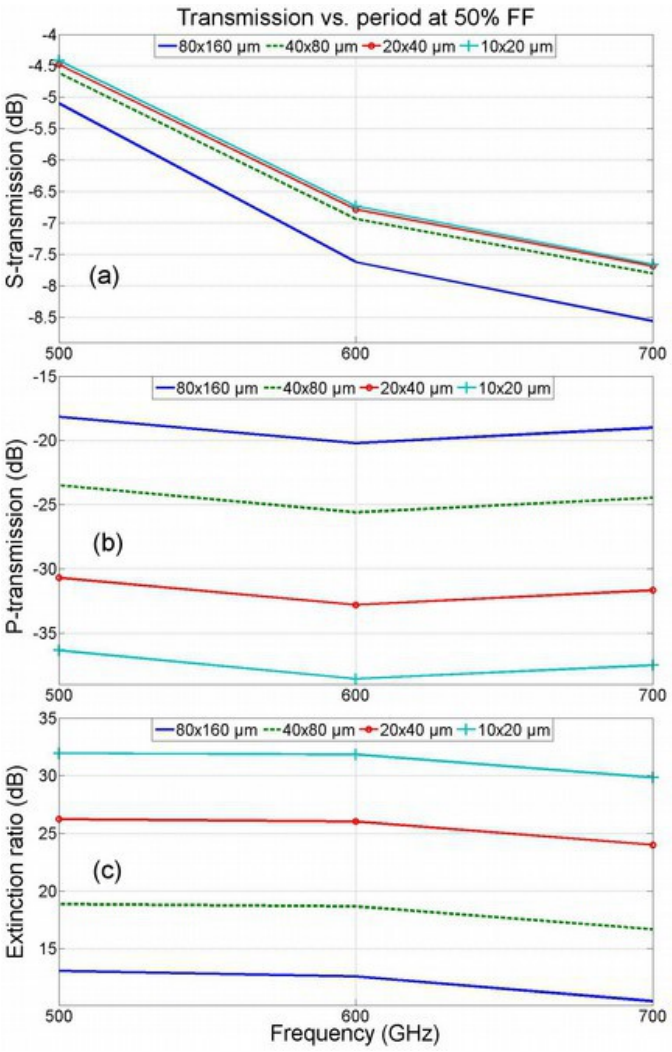

Figure 49: The polarizer period study at a constant FF on a polycarbonate substrate. This figure agreed with results previously found by others that decreasing the period to sub-wavelength sizes improves performance [92].

The results clearly agree with previous work in that decreasing the sub-wavelength period improves the performance of THz wire-grid grid polarizers. The observed increase in e_T (Fig. 49(c)) is attributed primarily to the reduction in P-transmission with decreasing period (Fig. 49(b)), but there was also a marginal increase in S-transmission (Fig. 49(a)). These initial simulations were done with 1.5 mm thick polycarbonate substrates, and this explains the rapid increase in loss in S-transmission with frequency. The wire grids themselves are reflecting very little radiation in S-transmission, which is why the data in Fig. 49(a) converge as the period decreases. This will be substantiated by the quartz simulations done later. The P-transmission decreases

steadily with period, as expected. In P-polarization there are no SSP effects present because there is not any significant dipole formation across the polarizer gaps, so as the gap size decreases the reflection must increase, thereby lowering transmission.

After confirming that reducing the polarizer period to deep sub-wavelength levels improves polarizer performance, the second set of simulations aimed at finding the optimum FF at a constant period. These simulations were performed on the same periods shown in Fig. 49, but in Fig. 50 the results for only 40 µm period are shown because this was the value eventually selected for fabrication. The fill-factors chosen for the study ranged from 30% to 90% in 10% increments.

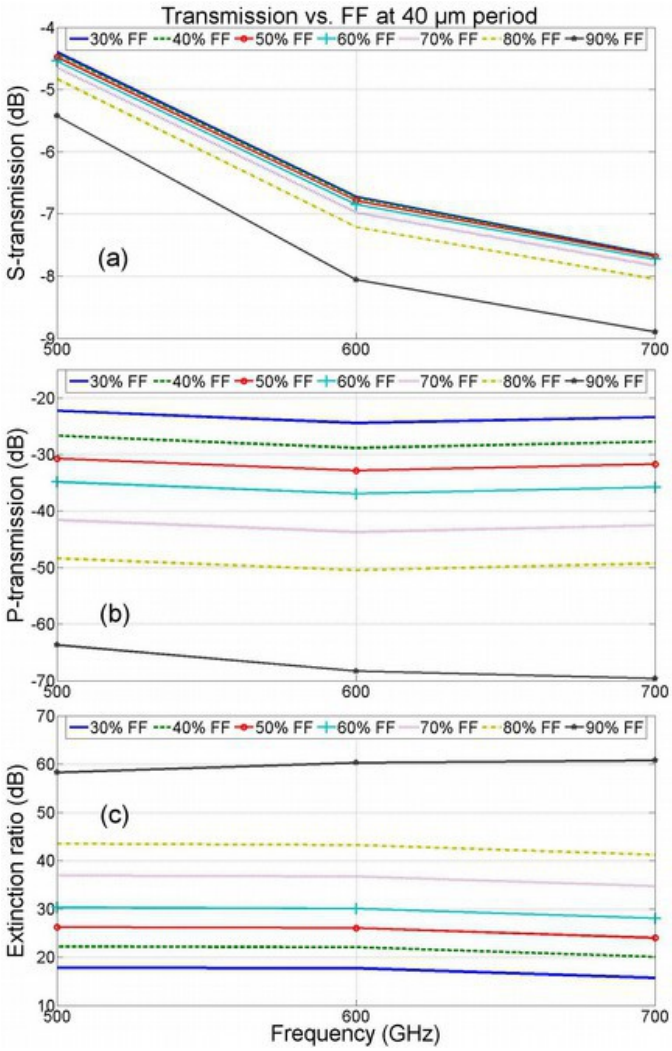

Figure 50: The transmission vs. FF simulation results on a polycarbonate substrate. (a) While S-transmission decreases with FF, the change is surprisingly small. (b) P-transmission sees a large, non-linear drop in transmission with FF. (c) The P-transmission dominates the FF results, with the highest fill-factors having the greatest extinction ratio

The results from this study were very exciting; at all of the tested FF levels the S-transmission (Fig. 50(a)) was quite high, with the low-FF data again converging on the polycarbonate absorptive limit. This means that the

highest-FF wire-grid of 90% only exhibited ~1 dB of insertion loss (neglecting the polycarbonate absorptive losses). And it suggests that the SSP enhancement present in each grating must be increasing as the FF increases, likely because the EOT is also strengthening. This increasing SSP effect is enabled by a non-linearly (concave up) increasing Poynting vector magnitude in the polarizer gaps. This is hardly surprising considering that while the FF tripled from 30% to 90% the S-transmission remained relatively unchanged. It should also be noted here that the geometric optical limit for transmission at 90% FF is -10 dB, neglecting any absorptive losses. The S-transmission of the polarizers simulated here were all above that level even with the absorptive losses.

The results become even more exciting when the P-polarization results are analyzed (Fig. 50(b)). As the FF increases, the P-transmission decreases super-linearly. This makes sense given that the percent change in gap size increases super-linearly as FF increases. For example, from 30% to 40% FF the gap size decreases 15% and from 80% to 90% FF the gap decreases 50%. So this means that a high FF polarizer should be able to substantially outperform a lower FF polarizer (like those commonly seen commercially) in P-polarization. The large super-linear decrease in P-transmission dominates the extinction ratio plot (Fig. 50(c)), where the 90% FF polarizer has by far the highest e_T. The FF dependence on polycarbonate polarizers was published in a peer-reviewed journal [94].

From this point on, Z-cut single-crystal quartz substrates were adopted instead of polycarbonate because the quartz is relatively lossless at THz frequencies, allowing the polarizers to perform much better in general. With both the period and FF studies complete (on polycarbonate), the next step was to combine the results of each by testing how polarizer performance changes when the period is decreased on a high FF device. So to continue the simulations, two 80% FF polarizers were chosen, 80x100 µm and 32x40 µm. And since these polarizers were later fabricated, the simulations were swept from 200 GHZ to 1 THz with a resolution of 1 GHz (the experimental range). Using the frequency sweep also provided more insight into the detailed behavior of the polarizers, including etalon modes that were present because of the standing waves in the substrate. According to etalon theory, the standing-wave period can be calculated by $\Delta f = c/2nt$, where n = index of refraction, t = etalon thickness (0.5

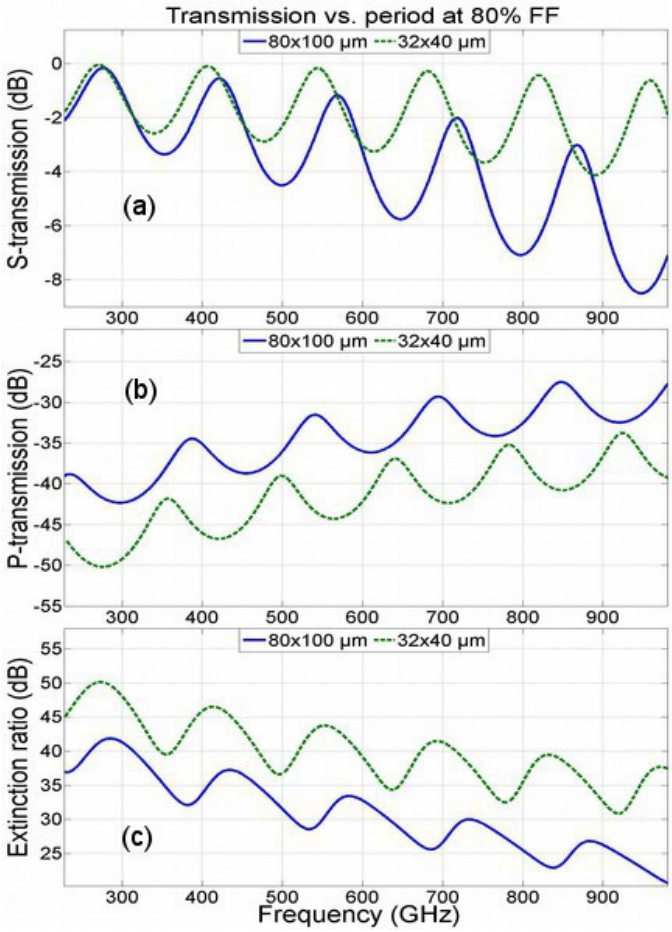

Figure 51: The simulated transmission through 80% FF polarizers with 100 µm and 40 µm periods on a quartz substrate. (a) S-transmission. (b) P-transmission. (c) extinction ratio. It is clear from these plots that the 40 µm period polarizer is superior in both S-transmission and P-transmission.

mm), and c = speed of light). This predicts a standing-wave period of $\Delta f \approx 142$ GHz for t = 0.5 mm and n = 2.2 [95], and the simulated results are shown in Fig. 51.

As predicted, the standing wave period is ~142 GHz. For each polarizer the standing waves create slightly different peak frequencies, because of reflective phase differences created by the metal strips on the surface of the polarizer. In any case, the most important information shown in Fig. 51 Is that the 32x40 μm is vastly superior to the 80x100 μm period polarizer. The results are similar to the previous results on polycarbonate substrates in that the smaller period polarizer has higher S-transmission (Fig. 51(a)) and much lower P-transmission (Fig. 51(b)).

Other useful information can be seen in this simulation because of the quartz substrate. The S-transmission of the 32x40 μm polarizer is very near 100% for the entire simulated spectrum at constructive interference peaks, which helps illustrate the transparency of this substrate. Because of the high S-transmission, the 32x40 μm polarizer meets the EOT criterion set forth earlier, where most of the signal can pass through the polarizer. Another point can be made here to illustrate the EOT effects created by the SSPs. The optical geometric limit for transmission through an 80% FF unit cell is -7 dB, but in this simulation the transmission is considerably higher, especially with the 32x40 μm polarizer which has a minimum transmission of -4 dB at 900 GHz.

After finding that increasing FF and reducing period at the same time indeed creates a better polarizer, more simulations were done to find the optimal FF ratio. Earlier simulations only went to 90% FF, but the S-transmission was still high at this point. So increasing the FF further would finally show what period and FF would maximize extinction ratio while still having acceptable S-transmission. For this final simulation the period was set at 40 μm and the FF was set to 80%, 95%, 98.75%, and 99.75%. The results are plotted in Fig. 52 and are quite exciting. The transmission in S-polarization (Fig. 52(a)) was not significantly affected until the FF was near 99%. In fact, at two constructive interference locations more than half of the signal is transmitted even at 98.75% FF. As expected from previous simulations on the polycarbonate substrates, the P-transmission (Fig. 52(b)) decreased monotonically.

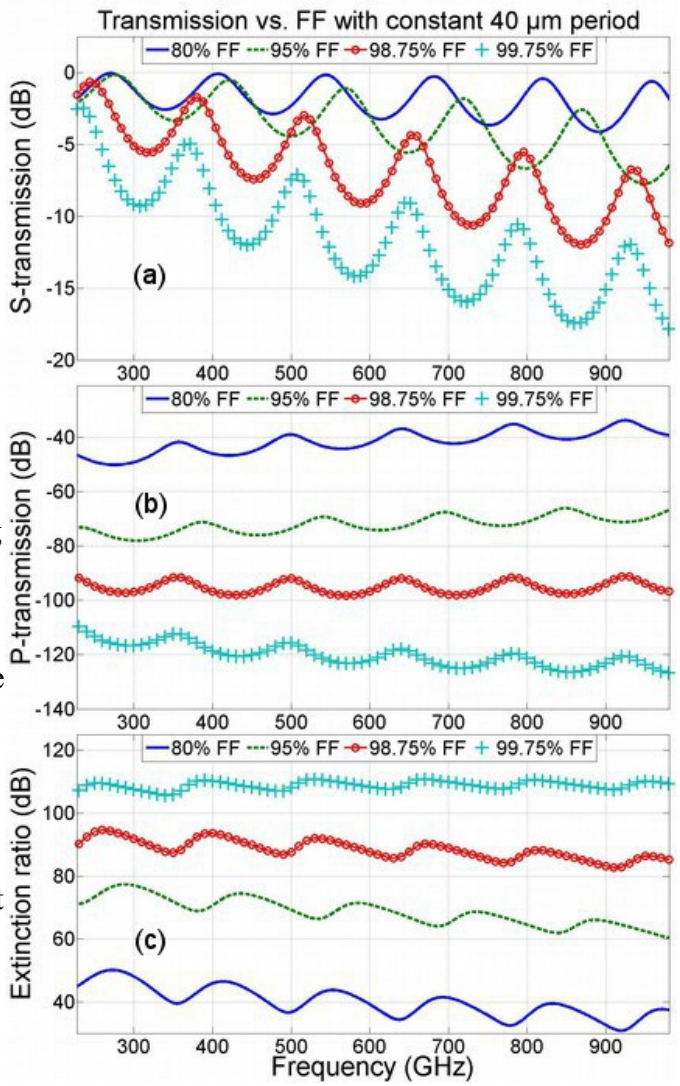

Figure 52: Simulated transmission vs. FF for 40 μm polarizers on quartz substrates. (a) S-transmission. (b) P-transmission. (c) extinction ratio. The results here are surprising, even the 98.75% FF polarizer transmitts more than half of the incident signal at certain frequencies.

The results for S-polarization are far more interesting than P-polarization because there is a very large SSP-enabled EOT effect present. Geometric optics predicts S-transmission magnitude for all four FFs (-7 dB for 80% FF, -13 dB for 95% FF, -19 dB for 98.75% FF, and -26 dB for 99.75% FF), yet the lowest simulated values are -4 dB, -7 dB, -13 dB, and -18 dB respectively (all coming near 1 THz). A consistent pattern observed in the S-transmission simulations is that the transmission is a strong function of frequency too, exemplified by the 99.75% FF polarizer having an astounding -2 dB transmission at 100 GHz. This is consistent with the SSP-enabled EOT being strongly dependent on the wavelength-to-period ratio (λ/L). When this ratio becomes smaller, EOT weakens and geometrical optics has a larger impact on transmission. The observed dependence of S-transmission on λ/L explains why reducing polarizer period improves THz performance.

This result is supported by the work published on the polycarbonate polarizer [94] where a decrease in transmission was also seen as frequency increased. But at that time it was unclear how much of the decrease was caused by the geometric effect versus absorptive losses from the polycarbonate substrates. However, since quartz has effectively no absorptive losses across the entire simulated spectrum, the decrease seen here must be the geometric effect. The geometric effect is also observed in Fig. 51 and explains why the S-transmission of the 80x100 μm polarizer decreases more quickly.

To confirm the SSP effects seen in the above simulations, three polarizer designs were then fabricated and tested: 32x40 μm, 38x40 μm, and 80x100 μm. Together these polarizers were able to experimentally test both the effect of FF (32x40 vs 38x40 μm)

and period (32x40 vs. 80x100 μm) on polarizer performance. Designs above 95% FF were not pursued experimentally because, although they exhibited higher simulated e_T, they were subject to fabrication errors caused by the limited spatial resolution of the lithography (2 μm).

4.2.1. High fill-factor experiments

The fabrication was done using standard planar-processing techniques, typically used for silicon fabrication. With the availability of a modest clean room and thin-film metal-deposition equipment, the processing is cost-effective and fast. There are three steps in the process, after the substrate has been chosen: 1) metal deposition, 2) patterning (photo-lithography), and 3) wet etching.

As mentioned earlier, the polarizer substrates were 0.5 mm thick z-cut single crystal quartz with optically polished, flat surfaces. Besides exhibiting excellent transparency, quartz also provides good adhesion with evaporated metals, such as aluminum. The diameter of the substrates (and hence the polarizers) was 2 inches. This diameter was chosen because it was compatible with the available fabrication equipment, and can also be easily packaged into 2-inch rotation stages for testing. Furthermore, 2-inch diameter was appropriate for use with the FPI spectrum analyzer. Without these limiting factors the polarizers could be made to be any size, as long as the substrates are available and the diameter is considerably larger than the incoming wavelengths.

The aluminum was deposited on the quartz substrates using a thermal evaporator (Denton model DV-502B). Besides adhering to the quartz well, aluminum is a good

metal for fabrication because it has a low melting point and is relatively insensitive to evaporator conditions [96]. The target thickness for the evaporated films was 2000 Å. After evaporation, the polarizers were patterned onto the metal with a 2 µm thick film of positive photoresist (AZ-1518) using a contact mask aligner (Karl Suss MJB-3). After patterning the photoresist was removed with developer and the aluminum was etched with a standard phosphoric-based acid solution [97]. The remaining photoresist was then removed with acetone, leaving a finished and ready-to-use polarizer.

The polarizers were then packed into the 2-inch rotation stages. Because of the 0.5 mm quartz substrates the polarizers were physically robust, thus making handling and packaging very easy. A finished and packaged polarizer is shown in Fig. 53(a) and a micro-photo of the same (38x40 µm) polarizer is shown in Fig. 53(b).

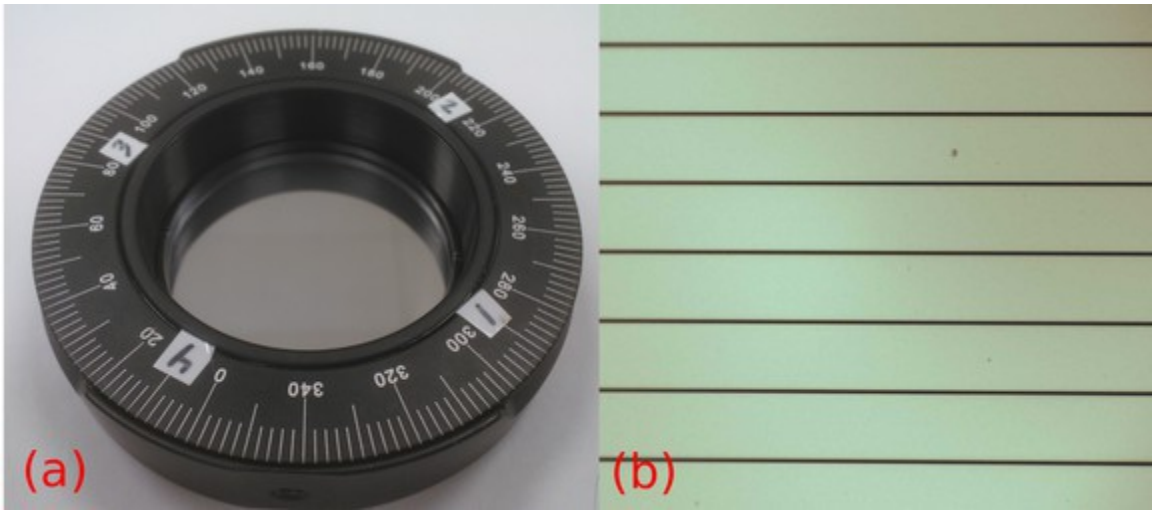

Figure 53: A finished and packaged 38x40 µm polarizer on a quartz substrate. (a) The polarizer in it's rotation stage, ready for testing. (b) A magnified photo of the polarizer.

Experiments consisted of measuring the THz transmission with a commercial frequency-domain spectrometer (Emcore model PB7100). The spectrometer frequency

range is 200 GHz to 1.8 THz, but because of dynamic range limitations, the polarizers were only tested from 200 GHz to 1.0 THz (P-transmission data after this point fell into the system noise floor). Even at 1 THz, the dynamic range of the spectrometer is at best 45 dB, and from the simulations the P-transmission can be vastly lower than this. However the dynamic range is higher at lower frequencies, at 200 GHz being ~70 dB. Another factor that limits dynamic range is the experimental setup, the detector and source in this system are circularly polarized, so each must have a polarizer in front to create a linearly polarized signal. To achieve the very high degree of linear polarization needed to test these polarizers (>70 dB at 200 GHz), two additional high-FF (30x40 μm) polarizers were used that provided a combined extinction ratio of ~80 dB [98]. These two polarizers were co-aligned to create maximum transmission so they could act as an analyzer. A block diagram of this experimental setup is shown in Fig. 54.

The first step in this experiment was to take a background scan with both analyzers in place but not polarizer under test. Next a bare quartz substrate was tested to confirm its transparency. This test confirmed that the absorption through the 0.5 mm quartz substrate

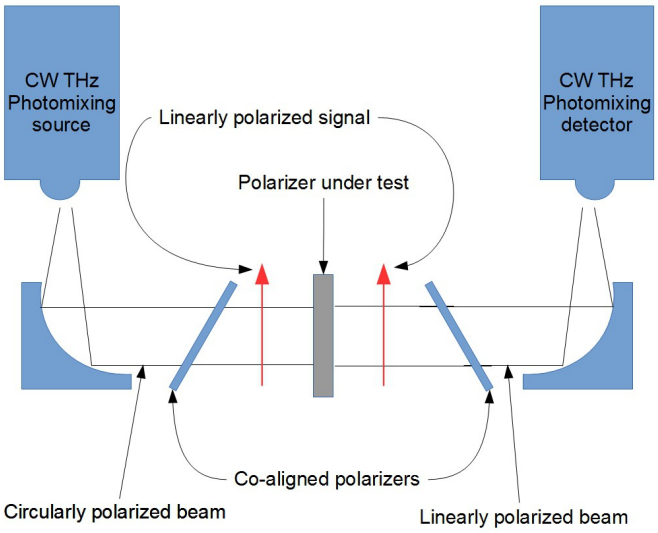

Figure 54: Block diagram of the experimental setup for polarizer characterization. Two high-extinction ratio polarizers were used to create a linearly polarized signal for the polarizer under test. The analyzers were angled in the beam path to prevent standing waves from forming in the system and skewing the results.

was immeasurably low and flat across the entire frequency range (Fig. 55). However, the predicted etalon-induced standing wave was present, with the correct period of 142 GHz and a peak-to-valley ratio of approximately 2.0 dB. With these initial scans completed the polarizers were then tested in S- and P-polarizations.

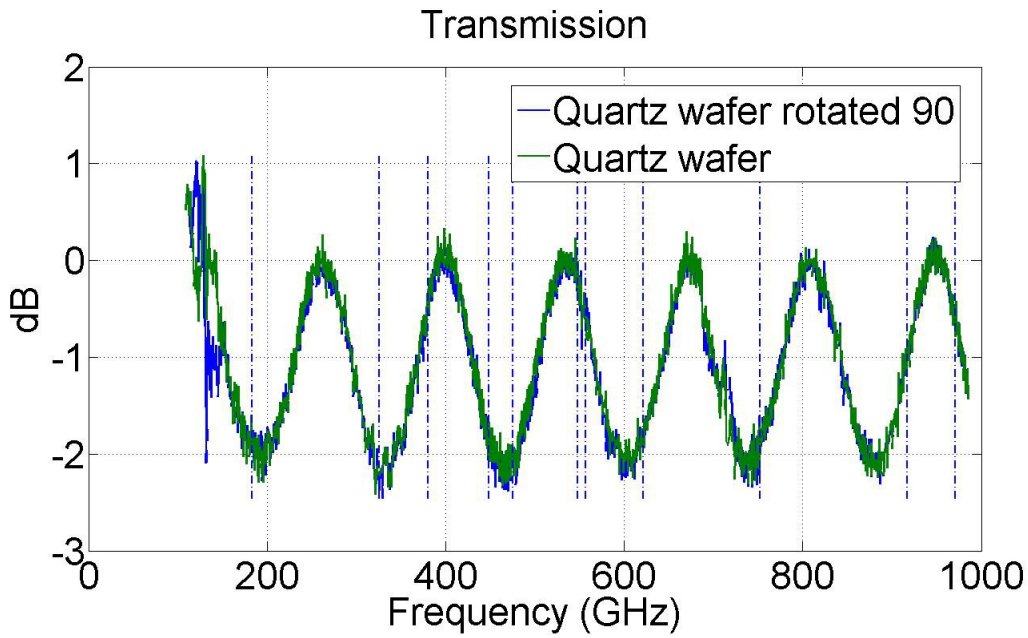

Figure 55: The experimental THz transmission through the 0.5 mm thick Z-cut single crystal quartz polarizer substrates.

The effect of varying period was tested first, namely the transmission of the 32x40 μm and 80x100 μm polarizers. The results are plotted in Fig. 56 whereby the S- and P-transmission are in good quantitative and qualitative agreement with the simulations (Fig. 51). The 32x40 μm polarizer displayed higher S-transmission (Fig. 56(a)) than the 80x100 μm polarizer, and higher than the geometric optics limit of -7 dB at all tested frequencies. This confirms the earlier assertions that decreasing the polarizer period to far sub-wavelength values increases the EOT effects. Just as in simulation, the minimum transmission through the 32x40 μm polarizer was -4 dB at 1 THz (excluding

the narrow valley at 700 GHz, which is thought to be an artifact). The transmission through the 80x100 µm polarizer was slightly lower than predicted. As a result the S-transmission reached the geometric limit at high frequencies. This small difference is not fully understood, but likely due to fabrication imperfections on the 80x100 µm polarizer. In further agreement with simulation, the S-transmission through both polarizers gradually decreased because of the geometric-optics effect present as λ/L decreases, as discussed in the previous section.

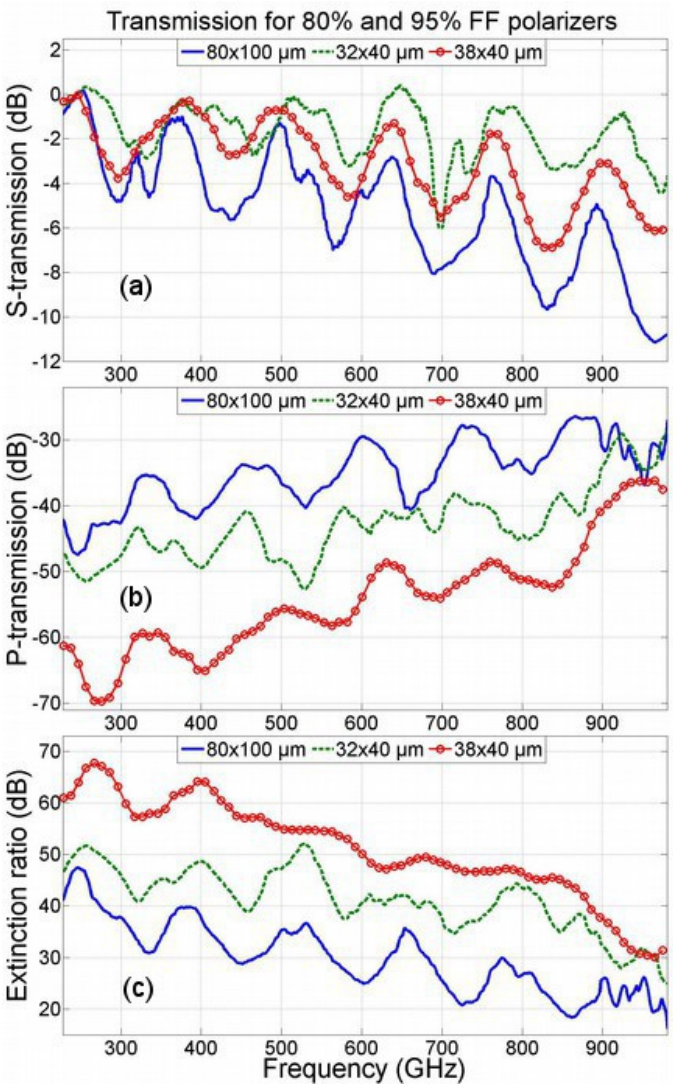

Figure 56: Experimental transmission results for all three fabricated polarizers on quartz substrates. (a) S-transmission. (b) P-transmission. (c) extinction ratio. These results show that smaller period and high-FF dramatically increase the polarizer extinction ratio without harming S-transmission a great deal.

The P-transmission (Fig. 56(b)) increases gradually with frequency and the measurements are nearly identical to the simulated results. As predicted, the 32x40 µm polarizer has significantly lower P-transmission – a result of the incoming waves not being able to resolve the smaller gaps as readily. Importantly, these

results confirm that reducing the polarizer period is important on high FF polarizers. The etalon induced standing wave is present in both S and P results as well, with the expected period of 142 GHz and a peak-to-valley depth of ~4 dB for S-polarization, and ~10 dB for P-polarization. The increase in depth compared to the bare quartz substrate (2 dB) is because the wire-grid interface is much more reflective than the quartz-air interface. Noisy undulations are present in the P-transmission results above 900 GHz and are caused by the transmitted signal approaching the instrumental noise floor.

With higher S-transmission and lower P-transmission, the 32x40 μm polarizer has much higher extinction ratio (Fig. 56(c)) than the 80x100 μm polarizer, by ~10 dB across the spectrum. The observed experimental extinction ratios are very close to the simulated predictions. This result confirms that smaller periods create superior polarizers by taking advantage of SSP techniques and EOT.

Next the FF study was performed experimentally, the results also plotted in Fig. 56. To perform this study the 38x40 μm polarizer was characterized in the same way as the previous polarizers. The measured S-transmission for the 38x40 μm polarizer (95% FF) agreed very well with the simulated prediction, consistent with large EOT effects being present. The S-transmission was at least 6 dB higher than the predicted geometrical limit of -13 dB across the entire frequency range. S-transmission was lower than for the 32x40 μm polarizer, but only by a small margin. Nevertheless, the 38x40 μm polarizer still had higher S-transmission than the 80x100 μm polarizer, despite having higher FF. This result supports the simulated effects of polarizer period.

The measured P-transmission was also very interesting because of the system

dynamic range limitations. This measurement was in the noise floor for nearly the entire frequency range for the 38x40 μm polarizer. Therefore, the P-transmission data shown in Fig. 56(b) represents an upper bound of the true P-transmission values. The actual P-transmission values for the 38x40 μm polarizer are not known, but are at least as low as shown here. The accuracy of the previous polarizer measurements suggests that the 95%-FF P-transmission should be close to what was predicted by simulation – a very encouraging possibility. In any case, the P-transmission of the 38x40 μm polarizer is considerably lower than the 32x40 μm polarizer.

The large EOT observed in the S-polarization combined with the extremely low P-transmission mean that the 95% FF polarizer has much higher extinction ratio than both 80% FF polarizers. In addition, the noise-floor-limited P-polarization results mean that the 64 dB extinction ratio realized by the 38x40 μm polarizer at 400 GHz is minimum-bounded, but still at least 20 dB better than what is seen in commercial free-standing wire-grid polarizer at the same frequency [85]. The findings in this work, that high FF plays such an important role in polarizer design, were new to the THz field. As such, they have been published in peer-reviewed journals [94], [99].

4.2.2. Performance at higher THz frequencies

Some THz applications, such as TDS systems and possibly the THz FPI spectrum analyzer, higher frequencies are used. A common problem with commercial free-standing wire-grid polarizers is that they perform poorly at high frequency (> 1 THz). So while it is evident that high FF is an important design consideration for the low-end of the THz spectrum, it is worth investigating the performance at high frequencies. To predict how high FF effects performance well above 1 THz, new simulations were conducted on the polarizers from 0.1 to 5 THz, in 1 THz steps. The simulations are summarized in Fig. 57 and show that high FF is indeed very important above 1 THz. The S-transmission (Fig. 57(a)) continues to decrease out to approximately 3 THz for all three polarizers but then begins

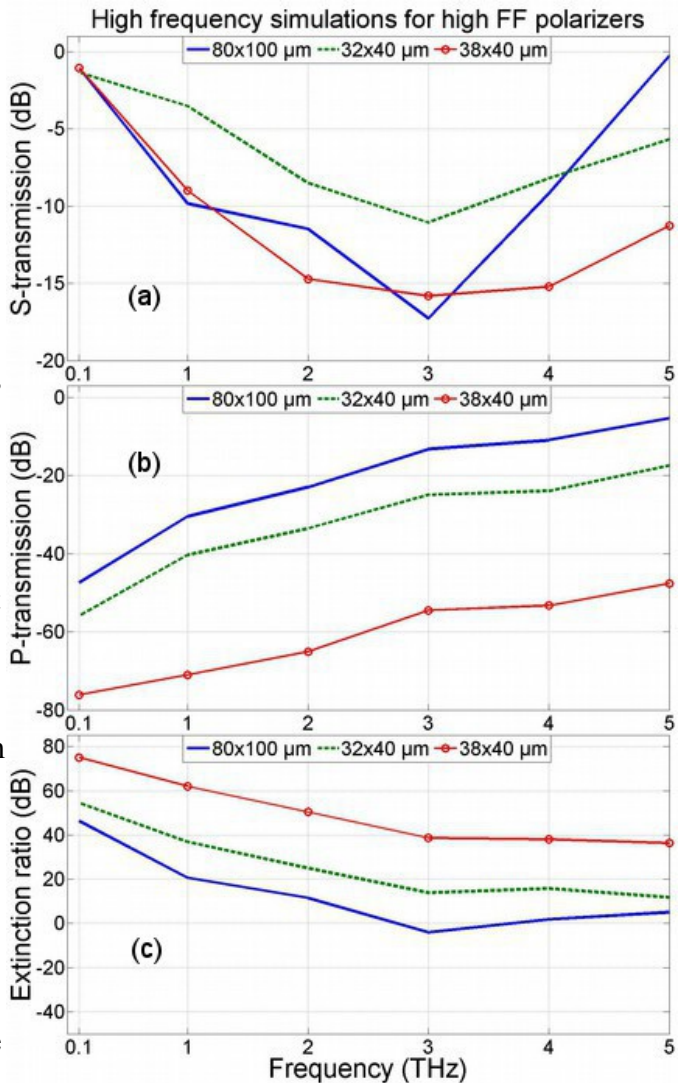

Figure 57: Simulated performance of the high FF polarizers (on quartz) at high frequency. (a) S-transmission. (b) P-transmission. (c) extinction ratio. Only the 95% FF polarizer maintains an extinction ratio > 30 dB over the entire spectrum, while other polarizers had poor performance (< 20 dB of extinction) at and above 3 THz. It should be noted that a weak absorption signature is known to occur in quartz at 3.84 THz, but it is weak and rather narrow so should not affect the polarizer performance significantly [95].

to increase above this point. This is an interesting result and helps to maintain a useful extinction ratio, but is not fully understood. However the accuracy of the previous simulations suggest that this is probably accurate as well.

The P-polarization simulations (Fig. 57(b)) are consistent with simulations and experiments below 1 THz. The P-transmission increases monotonically with frequency. As the wavelengths become shorter the electromagnetic behavior should slowly approach the geometric optical limit (-7,-7, and -13 dB respectively), as happens with all polarizers. The simulations show that this is happening, but it is evident that the P-transmission through the 38x40 μm polarizer is increasing at a slower rate compared to the other two polarizers. This is expected given the higher fill percentage and considerably smaller air-gaps in this polarizer. As a consequence, the 38x40 μm polarizer maintains a useful extinction ratio (Fig. 57(c)) across the entire simulated spectrum, still providing nearly 40 dB at 5 THz. The other two, lower FF polarizers do not perform as well and are inadequate at and above 3 THz. This is exemplified by the 80x100 μm polarizer which has a negative extinction ratio at 3 THz (more radiation is transmitted in P-polarization than in S-polarization). From these simulations it is evident that having small feature sizes compared to the wavelength, and high FF, are important design considerations for high-frequency THz performance [99].

The frequency-domain spectrometer (PB7100) could not be used to test these high-frequency predictions, because of the previously mentioned dynamic range limitations. However, initial measurements have been taken on a TDS system that provide data out to ~2 THz [100]. The results are shown in Fig. 58 and the extinction

ratios in these initial results appear to be significantly lower than simulation. The results below 1 THz are also substantially lower that previously measured values. The experimental setup used to collect this data was different, so the cause for this discrepancy is, at this point, unknown. Nonetheless, the 38x40 µm polarizer still has a higher extinction ratio in these results by a small margin. This data represents the highest frequency data recorded on these polarizers, as such the TDS engineer will present this at IRMMW-THz 2014 (abstract approval pending) [100].

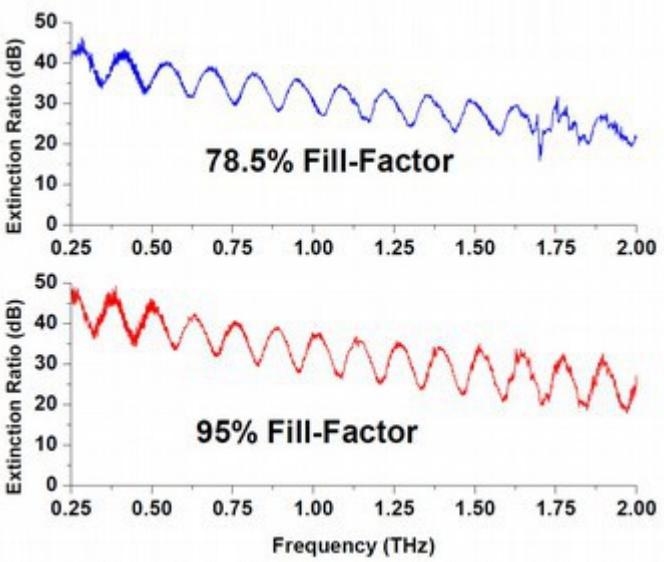

Figure 58: 32x40 µm and 38x40 µm polarizer extinction ratio measurements from a TDS system [100].

4.2.3. Effective fill-factor designs

The FF study showed that increasing the FF can greatly improve the extinction ratio of a wire-grid polarizer through SSP enhancements, but questions still remained about how to use SSPs most effectively. For instance, the 38x40 µm polarizer had a much smaller gap size than the other polarizers, it was unclear how much this alone effected the performance outcome. So to gain a greater practical understanding of SSPs a series of new simulations were conducted (with the same software and parameters) that varied FF and period in previously untested combinations. These simulations eventually

lead to the design and fabrication of a new “effective fill-factor” bi-periodic polarizer design with superior high frequency performance in S-polarization.

First an additional simulation was run to answer the question posed in the previous paragraph about the gap size. The 38x40 μm polarizer was used again, which has a 2 μm gap size, and a 2x4 μm polarizer was also simulated. The FF is obviously different between these two designs, 95% vs. 50%, but the gap size is the same. This simulation would determine how much of the enhanced extinction ratio was really a result of increasing FF, and not decreasing gap size. The results from this simulation are shown in Fig. 59 and the lower FF 2x4 μm polarizer had drastically lower extinction ratio (~20 dB) compared to the 38x40 μm polarizer. This result is logical because increasing the FF physically reduces the area that radiation can use to pass through the polarizer, whereas only decreasing period does not. Then, the large SSP enhancement present in the 38x40 μm polarizer allows for high S-transmission, so the extinction ratio improves. This result proves that high FF SSP designs offer large improvements to polarizer performance.

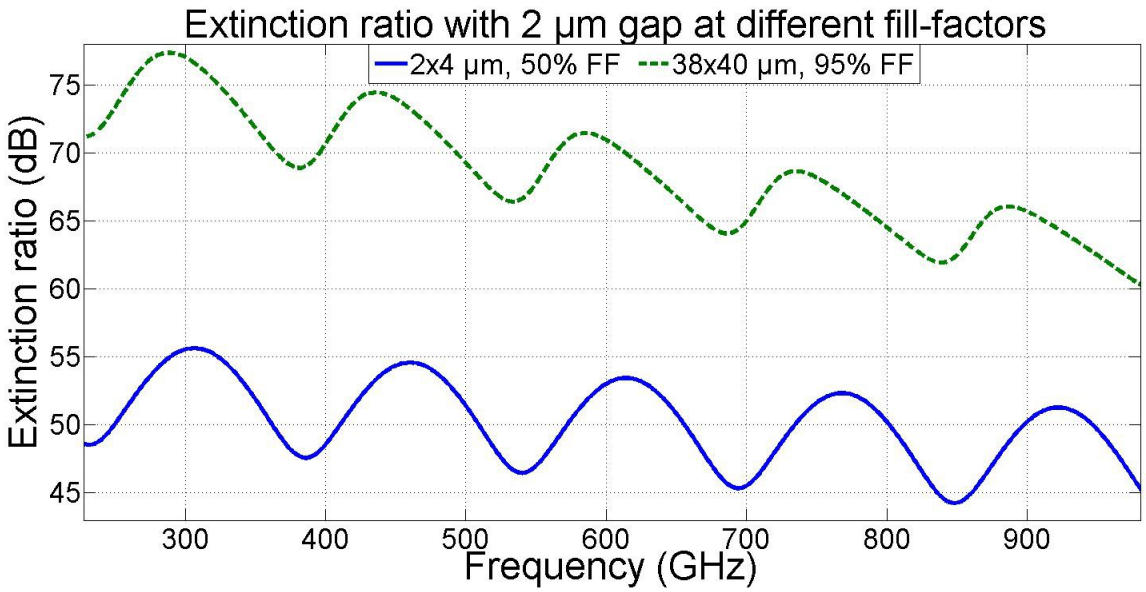

Figure 59: Extinction ratio of two polarizers with identical air gap size (2 µm), but different FF. This confirms that high FF does indeed have a significant effect on polarizer performance.

The next simulation performed compared the change in transmission as period is varied, for two different FF. Fig. 51 measured how insertion loss as period varied, but only for one FF, this simulation compared two FF levels. It was anticipated that the higher FF polarizer would see a slower increase in P-transmission as period increases, because this polarizers gap size will change less, and there is a smaller percentage of open space. The results agree with this prediction (Fig. 60(b)) – the P-transmission in the 50% polarizer increases at about twice the rate of the 95% FF polarizer, and another noticeable difference in P-transmission is that the lower FF polarizer has a bigger performance drop as frequency increases. Again, the difference in performance as frequency changes makes sense, because of geometric factors (the low FF polarizer has larger gaps).

In S-polarization (Fig. 60(a)) the same geometric effect that enhances the high FF P-transmission rejection, causes lower S-transmission that decreases more quickly than in the low FF polarizer. However the decrease in S-transmission for the high FF polarizer is not nearly as significant as the increase in P-transmission for the low FF polarizer. Because of this the high FF polarizer sees a much slower drop in extinction ratio (Fig. 60(c)) as the period increases (about half). The undulations present in these results are likely a result of the standing waves shifting because of phase changes as the period changes.

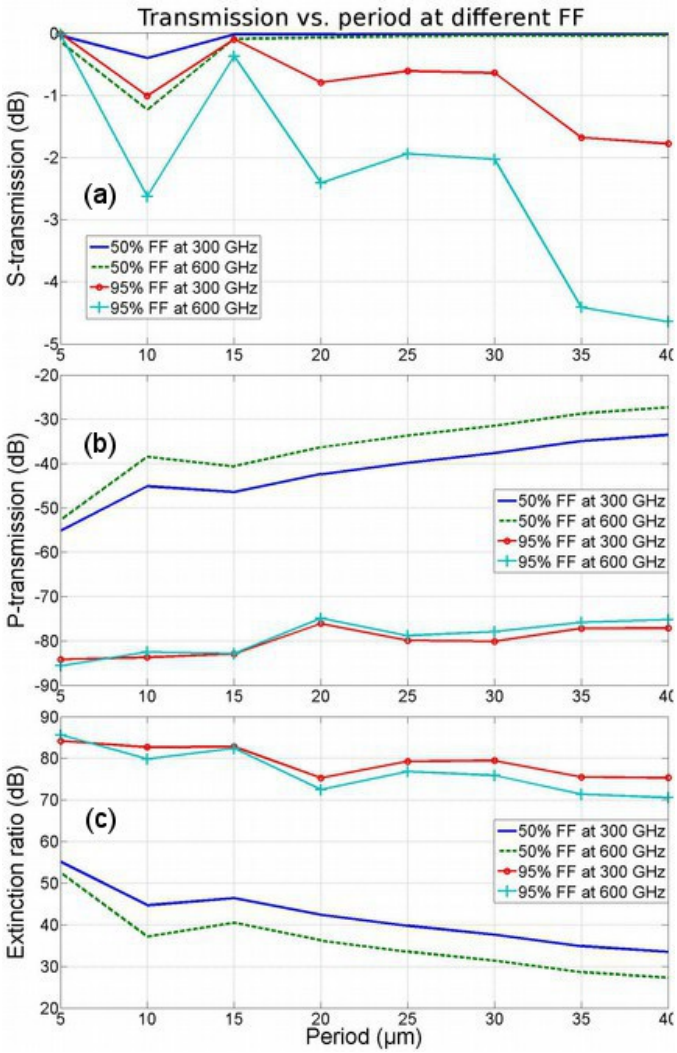

Figure 60: High FF polarizers are less sensitive to period change. S-transmission (a) decreases more noticably for high FF, but the P-transmission (b) increases at a much faster rate for the low FF polarizers. The extinction ratio (c) for high FF polarizer decreases more slowly with period as a result.

Using the results from these simulations, and the experiments in the previous section, a new design was created (Fig. 61(b)). The goal of this design was to mimic the high FF polarizer performance in P-polarization, while at the same time decreasing the

geometric effect seen in S-polarization, thereby improving the performance of the polarizer by reducing reflection of the desired (S-polarized) signal. This idea germinated from the simulation in Fig. 59 which showed that high FF greatly decreases P-transmission, and from Fig. 60 which showed that small period gratings greatly outperform larger period gratings. So if both high FF and smaller gratings could be combined, without creating the need for smaller fabrication capabilities, the THZ polarizer performance could be improved. Accomplishing a high S-transmission could also have the benefit of increasing extinction ratio. The new design was called an effective fill-factor design (EFF). The EFF design is similar to the regular high FF design, but the metal polarizer strip is divided into many smaller strips. Dividing the strips makes the actual FF of the polarizer much lower, 40%. Because the gaps in the metal strips are so small, the incoming P-polarized wavelengths should still be highly reflected, P-transmission should be mostly determined by the size of the large gap. However in S-polarization the lower actual FF and SSP effects from the smaller grating should allow more signal to pass. In the design shown here the regular polarizer (Fig. 61(a)) is 30x40 μm and the EFF polarizer (Fig. 61(b)) is labeled as 30x40x2x2 μm (30x40 μm with 2 μm wide strips, separated by 2 μm).

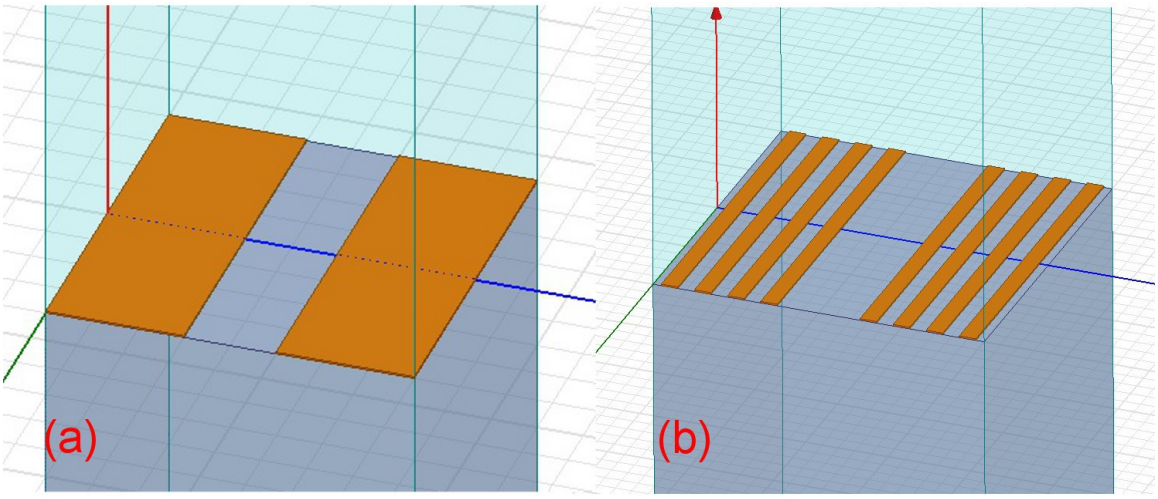

Figure 61: (a) Normal 75% FF polarizer unit cell, as it appears in HFSS. (b) 75% EFF design with 40% actual FF.

The results (Fig. 62) from the EFF simulations agreed well with prediction; as frequency increases the S-transmission (Fig. 62(a)) trends very flat for the EFF polarizer, with very little reflection (minimum transmission of -1.75 dB), while S-transmission through the ordinary high FF polarizer gradually decreases with frequency. Then in P-polarization (Fig. 62(b)) the two designs have nearly identical performance (<1 dB difference), with the regular polarizer having slightly lower P-transmission. This was an exciting result, because it meant that high FF polarizer extinction ratios can be achieved without suffering from high insertion loss in S-polarization. As shown here the two polarizers should have nearly identical extinction ratio (Fig. 62(c)). The only limiting factor for this design is fabrication capability (i.e. minimum spatial resolution), the design chosen here was made with this consideration as the strips and small gaps are 2 μm, equaling the smallest resolution possible with the available fabrication facilities.

To confirm the EFF design simulations the two polarizers from Fig. 61 were then fabricated with the same fabrication process used in chapter III. The polarizers were also tested in the same photomixing spectrometer setup and Fig. 63 shows the results. The S-transmission (Fig. 63(a) is indeed very close between polarizers. Noise in the signal makes analyzing the result more challenging,

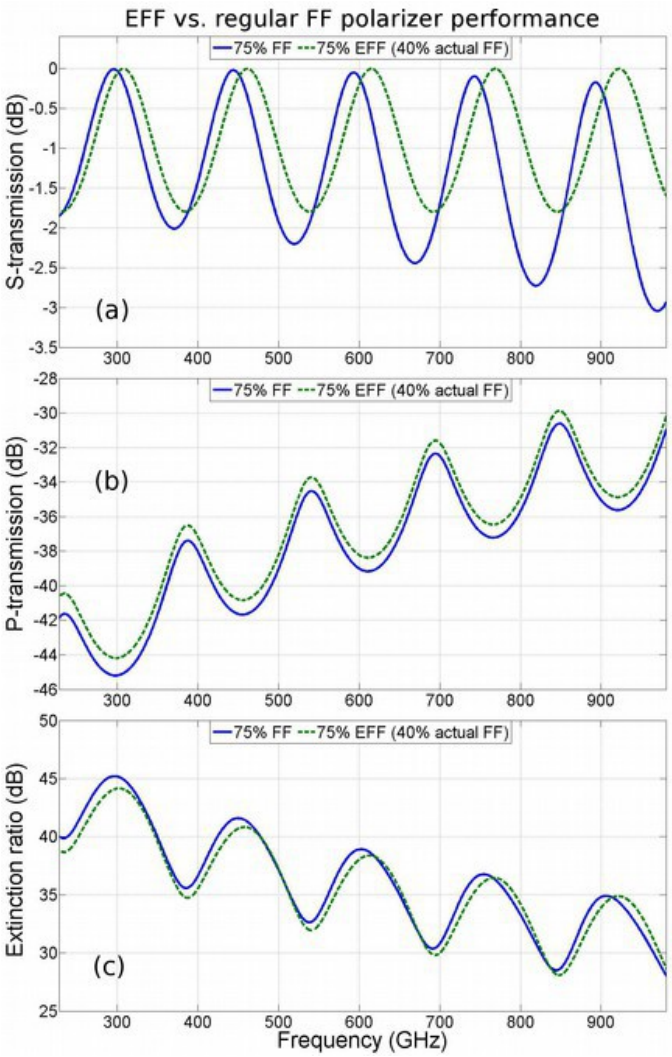

Figure 62: Simulated transmission through the 75% FF and EFF polarizers. (a) S-transmission, here the EFF polarizer trends flat across the spectrum, the high FF polarizer has a gradual decrease. (b) P-transmission, the two polarizers are nearly identical in performance. (c) Extinction ratio, both polarizers are nearly identical, but because of superior S-transmission the EFF polarizer begins to overtake the high FF polarizer.

but the EFF polarizer does trend flat across the measured spectrum, while the regular high FF polarizer sees a gradual decrease in S-transmission with frequency. The undulations in this data are larger than expected, and the maximum values go higher than 0 dB, both of these factors are likely due to system alignment imperfections caused by the analyzing polarizers. In any case, this data agrees with simulation that the EFF polarizer performs better in S-polarization at high frequency.

The P-polarization results (Fig. 63(b)) are very exciting as this is what would determine the usefulness of the EFF design. The EFF design appears to work as predicted. The P-transmission of the two polarizers is virtually identical, without a plot legend it would be impossible to predict which polarizer corresponds to each curve. The key factor that allows this design is that smaller periods have lower P-transmission, so the overall P-transmission through the EFF design is dominated by the larger 40 μm period. Once again, this is illustrated in Fig. 60(b) where the smallest simulated period (5 μm) has at least 10 dB lower P-transmission than the 40 μm period polarizers. Because of the close performance of the high FF and EFF polarizers, the extinction ratio results are also virtually identical (Fig. 63(c)).

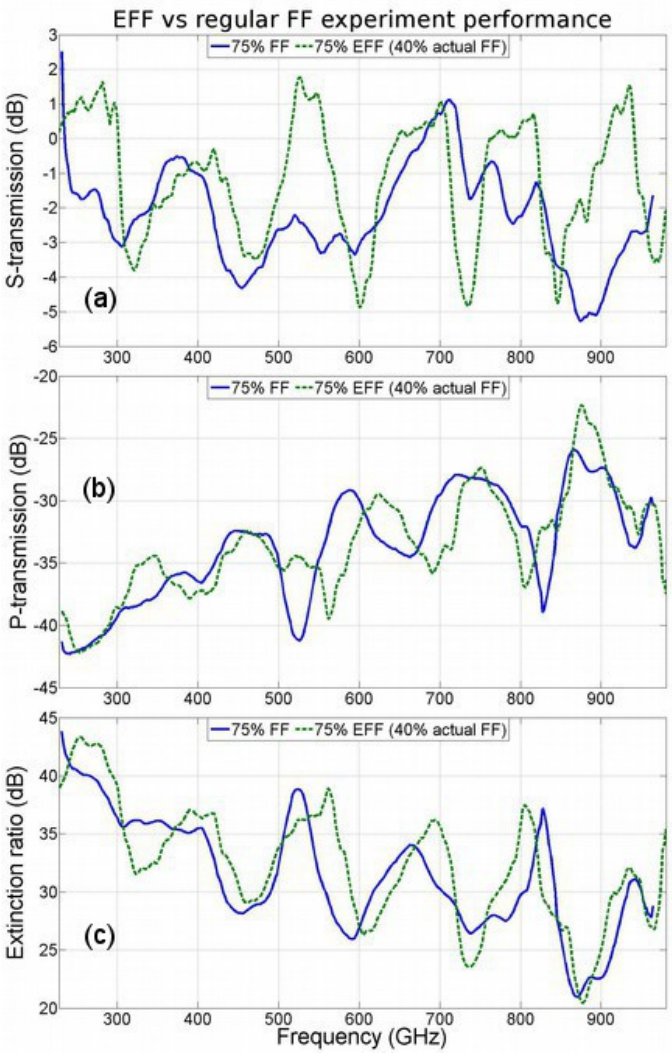

Figure 63: Experimental measurements of the fabricated EFF and corresponding high FF polarizers. (a) S-transmission, the two polarizers ae close but the EFF polarizer is trending flatter. (b) P-transmission, the two polarizers are nearly identical. (c) extinction ratio, once again the two polarizers are nearly identical.

The EFF design could be an important advancement for wire-grid THZ polarizers because of their lower insertion loss. In fact, this polarizer design was eventually chosen for the SSP polarizer enhanced THz FPI because of the S-transmission efficiency. In THz systems every dB of power is important, because there isn't much power available (see the power output values in chapter II). So in the case of a circularly polarizer incident signal, like that from the antenna design used in chapter II, the EFF polarizers will allow more of that signal to enter the FPI cavity, thereby increasing the SNR in the spectrum analyzer. For example, for a perfectly circular input at 900 GHz only 3 dB of signal will be kept from entering the FPI cavity with an EFF polarizer, because there is no S-transmission loss at this frequency. However the 38x40 µm high FF polarizer will lose twice the signal, ~6 dB, because of its higher S-polarization reflectance. The work done

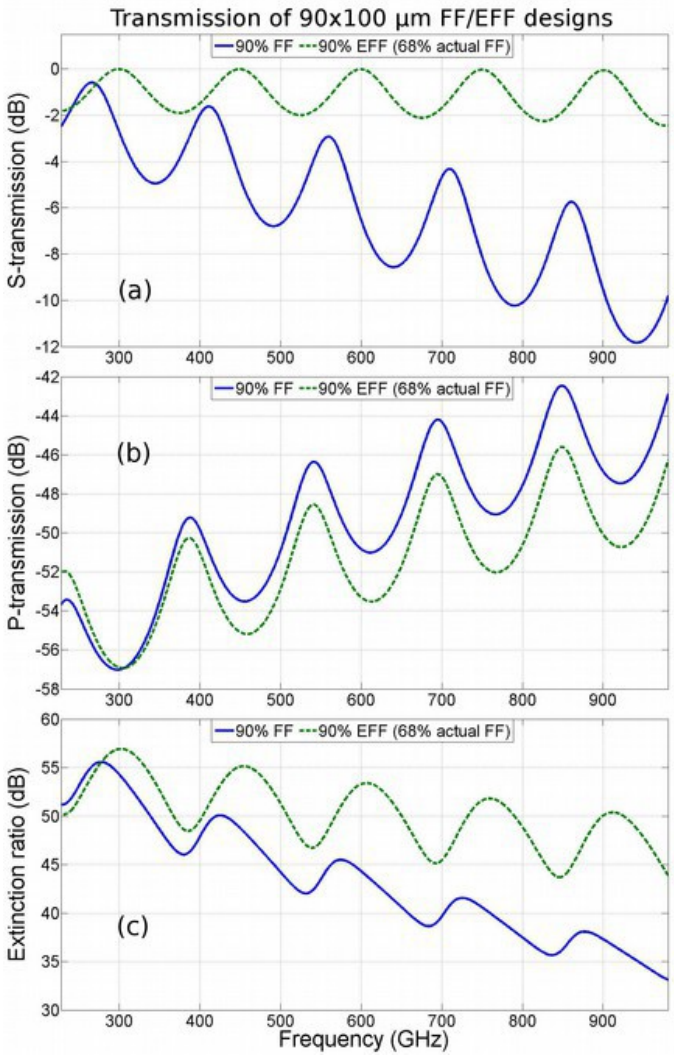

Figure 64: Performance of 90x100 µm FF and 90x100x3x1 EFF designs. (a) S-transmission. (b) P-transmission. (c) extinction ratio. This simulation used bother higher FF and larger period to provide a better example of how EFF "bi-periodic" polarizers can enhance performance.

here has certainly improved the practical understanding of THz polarizers and gratings, with both the high FF designs and the EFF designs. Because of this the EFF designs were recently presented at an international THz conference [98].

As a final note on EFF designs, it was realized after the experiments that the EFF technique would be better illustrated by a higher FF design, or a larger period. So simulations were then done with a 90x100x3x1 (3 μm strips separated by 1μm) μm EFF polarizer design (Fig. 64). This design was never fabricated, but the simulation results shown below help to reinforce the benefits of this design technique. Here the benefit in S-transmission is much more pronounced (Fig. 64(a)), where the smaller grating allows significantly more transmission (~10 dB at 900 GHz). The smaller grating even enhances the P-transmission (Fig. 64(b)) rejection slightly by slowing the rate at which p-transmission increases. This is not yet fully understood electromagnetically but may be caused by additional field cancellation effects created by electric fields oscillating parallel to the wires. As a results of better S and P performance this EFF design has a much higher extinction ratio (Fig. 64(c)) than the regular 90x100 μm polarizer.

4.3. A Summary of structured-surface-plasmons and their benefit to the linear polarizer

The research carried out in this work has advanced the design, performance, and understanding of Structured Surface plasmons in the THz field, primarily through the concepts of sub-wavelength period and high (>90%) fill-factor as applied to wire-grid polarizers. These techniques could likely be applied to other sub-wavelength

components, as long as they have a periodic geometry. This could include metamaterial THz bandpass filters [101] or Schottky diode detector arrays. Experiments have shown excellent performance from the high-FF polarizers from 0.2 to 1.0 THz, and simulations predict good performance at much higher frequencies as well. From a practical standpoint, the polarizers described in this chapter cost a fraction of a free-standing wire-grid, have superior THz performance, and are more robust.

A new bi-periodic polarizer was also demonstrated, called an effective-fill-factor polarizer (EFF). This polarizer can recreate the S-polarized performance of a low-FF polarizer, but the P-polarized performance of a high-FF polarizer. As such, the S-polarized performance of the substrate-based, EFF polarizers, combined with their flatness (because of the optically polished substrate), makes them perfect for use as polarizing mirrors in the FPI. The next chapter will discuss a new FPI design that uses the 30x40x2x2 μm EFF polarizers as the resonant mirrors. In addition to the publications already published on the high FF [94], [99] and EFF [98] polarizers, four new conference proceedings have been submitted to IRMMW-THz 2014 and await approval.

5. Improving the THz Fabry-Perot with linear polarizers

The previous chapter explained the polarizers created for this work in detail. With the advancements made on these components, this final chapter will wrap up the research plan presented in the previous chapters. Here the polarizers will be used to improve the THz FPI spectrum analyzer. Then the new extrinsic THz PC switches will be used as a source of THz radiation in a demonstration of the FPI with polarizing reflectors. This is shown by the dashed box in Fig. 65, which now encompasses the entire research plan.

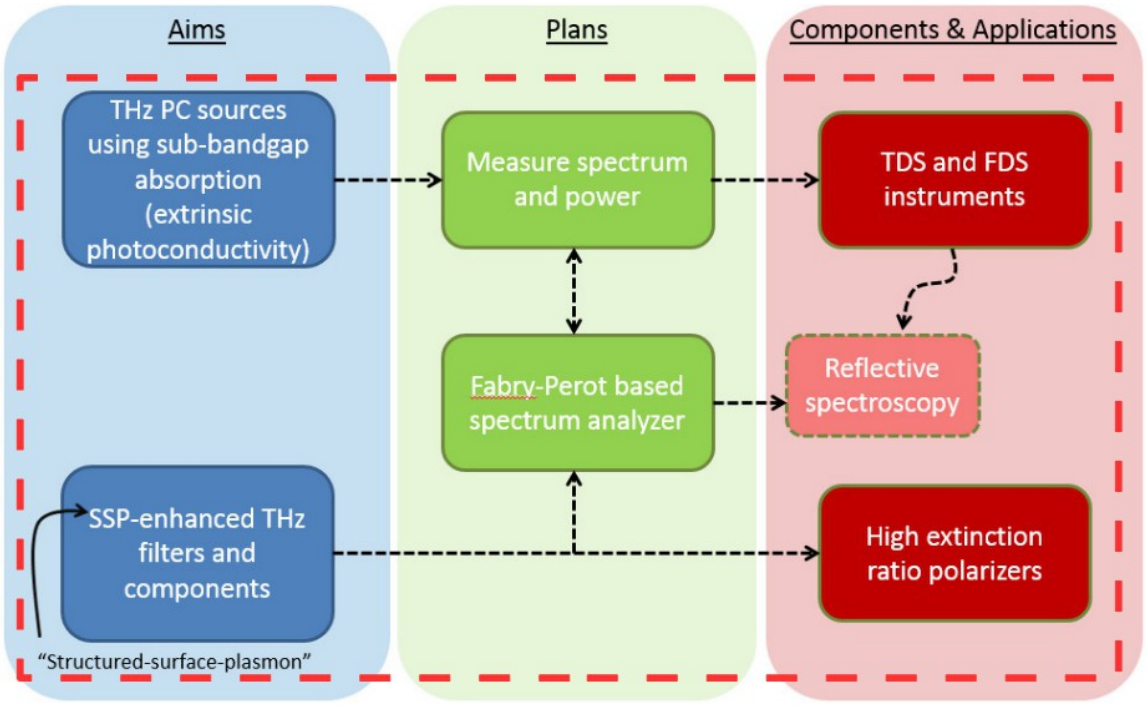

Figure 65: The research plan for this work. The presentation of the polarizing FPI in this chapter represents the culmination of the work done in all of the previous chapters.

Polarizers have many applications: they can be used as beamsplitters for interferometers, or for other instruments such as autocorrelators. When P-polarized light is strongly rejected by the polarizer, reflection is at least 99.9% for a high EFF THz wire-grid polarizer. This means that they could also be well suited as variable FPI reflectors, provided that the incident radiation is polarized. S- and P-polarzations are separated by 90 degrees, and in between these two orientations the reflectivity of a polarizer changes monotonically. This is illustrated in Fig. 66, where the reflectance of a polarizer was calculated from the experimental transmission (R = 1 – T) as a function of rotation angle.

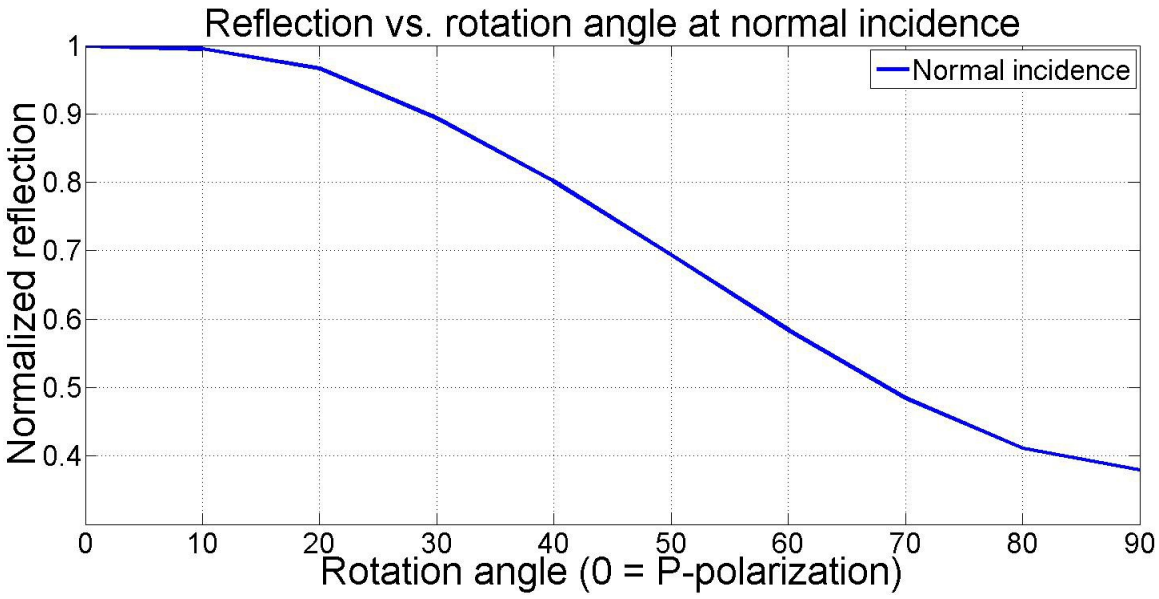

Figure 66: Reflectance of a generic THz polarizer at different rotation angles between S- and P-polarization, at normal incidence, for the 30x40x2x2 μm EFF polarizer. This experiment was conducted with a 100 GHz linearly polarizer signal.

The reflectance of the polarizer in this test reached 95% (at 100 GHz) approximately 23 degrees away from P-polarization. The slope of the reflectance vs. rotation is not steep at this point, so tuning the desired reflectance of 95% for FPI reflectors is accomplished quite easily because of the insensitivity to rotation. If the

mirrors of the FPI were indeed polarizers, the reflectivity could be tuned to be exactly the desired value up to at least 2 THz. This makes polarizers a perfect candidate for mirrors. There is another advantage to using polarizers as well, which is that the spectral selectivity (Q-factor) of the FPI would also be easily tunable. So if the spectrum being measured was from a very powerful source, the Q-factor of the FPI could be increased to obtain a finer scan resolution. Alternatively, if there was very little power available, a high Q-factor might push the signal into the noise floor of the detector, so a lower Q and less precise resolution could be used. This makes a polarizer-based FPI far more flexible than other designs.

Since the polarizers can be tuned for reflectance, this removes another limitation. Like the wire-mesh, polarizers have reflectance that changes with frequency (although not as severely). So an advanced polarizer FPI design could have polarizer rotation angle that changes during the spectral scan, to keep reflectance constant. An example of the change in reflectance vs. frequency of a polarizer is shown in Fig. 67. This plot is transmission, but again, R = 1-T is a safe assumption for these wire-grid polarizers because the crystal quartz substrates have negligible THz absorption.

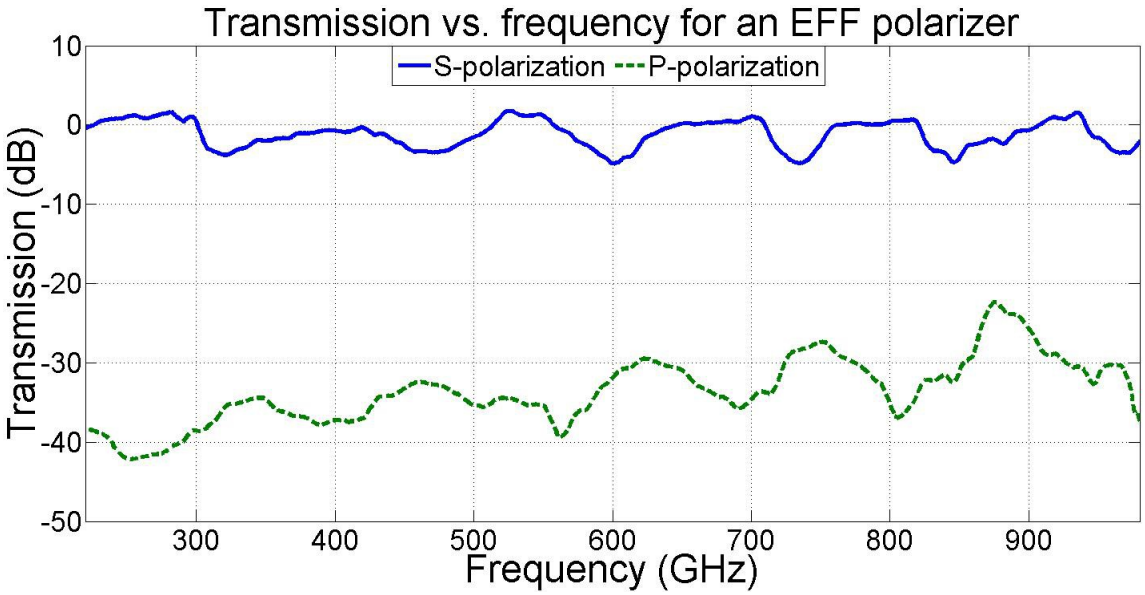

Figure 67: Transmission through the 30x40x2x2 μm EFF polarizer. Here the change in transmission (and thus reflection) vs. frequency is shown.

5.1. The linear polarizer enhanced THz Fabry-Perot interferometer

In the previous chapter the polarizer chosen for use as FPI reflectors was described: the 30x40x2x2 μm EFF polarizer. This one is a good choice because it has high e_T and good transparency in S-polarization. The new FPI design (Fig. 68) was created using a CNC machine, linear translation stage, 2-inch rotation stages, and the same Zaber linear actuators used for the previous FPI design. A linear translation stage was used instead of a cage rod system because it was easier to mount rotation stages, however, it had other benefits as well. The problems with the cage rod FPI system were explained in great detail in chapter III and Appendix A, where binding, rocking/leaning, nonparallel FPI mirrors, and motor slipping could occur, thus skewing interferometric results. The linear translation stage moves much more smoothly, easily, and precisely in one plane only. So all of the previous problems associated with the cage-rod system were

removed. The tunable FPI plate was simply mounted to the end of the translation stage, and the stationary mirror was mounted 1 cm past the end of the translation stage (Fig. 68 shows the stage extended some distance).

To move the translation stage the Zaber linear actuator was coupled to the stage as shown. The translation stage was spring loaded, so a small but constant force pushed the stage into the linear actuator at all times. Because of this the linear stage didn't require fastening to the linear actuator. So when the linear actuator extended, the stage would advance forward because of the actuator force, and when the linear actuator retracted the stage would retract in kind. Since the same linear actuator was used for this design as in chapter III, the same MATLAB code could be used as well.

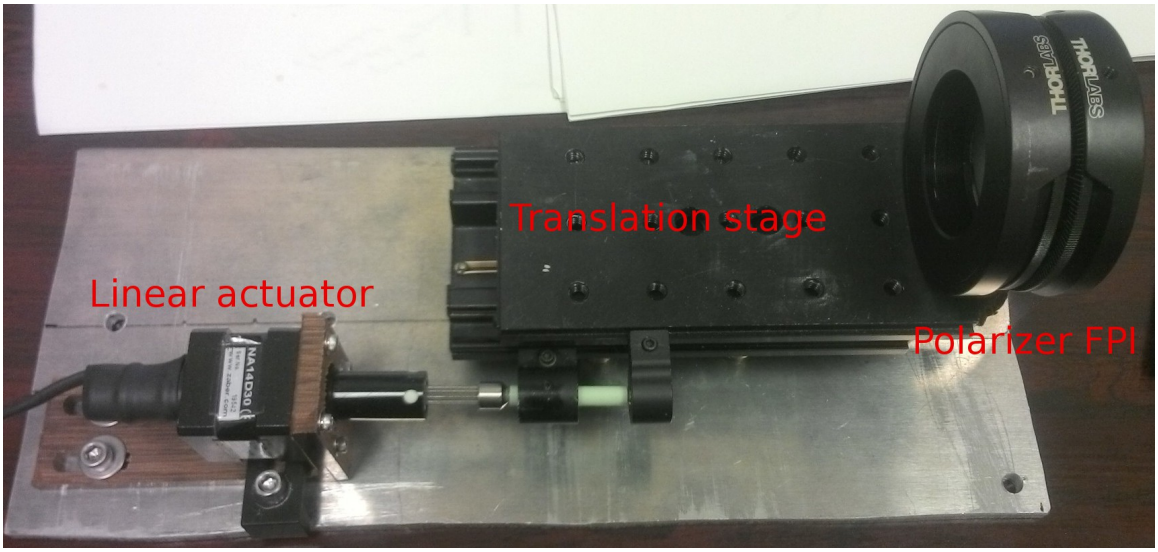

Figure 68: New FPI design. The linear actuator provides much more stable and reliable movement, compared to the cage rod system. The polarizers are mounted to the front surface of the rotation stages to create the FPI cavity.

To make this FPI design easily transportable, it was mounted to a single aluminum plate (pictured) with precisely located mounting holes for the linear actuator, the translation stage, and the stationary FPI mirror. This plate, along with the linear

actuator mount, and the stationary mirror mount, were made with a CNC milling machine. The first step in this process was to design each part with CAD (computer aided design) software. BobCAD was used for this work (designs are presented in Appendix C). After the parts were each designed, they were transformed into the appropriate CNC machine code (g-code in this case) and the parts were fabricated.

Figure 69: A polarizer based FPI mirror. Using glue, the polarizer is attached so it protrudes from the front surface of the rotation stage.

The last step in making the new FPI design was mounting the new EFF THz polarizers to the rotation stages, so the reflectivity of the FPI could be adjusted easily. This would allow the FPI to be set for high spectral resolution and lower transmission, or for lower resolution but higher power transmission. The rotation stages are shown in Fig. 68, but the polarizers are difficult to see, so one is shown separately in Fig. 69. The method used to mount the polarizer to the rotation stage was simple. A retaining ring was partially screwed into the center of the rotation stage and glued into place, then the polarizer was glued to the retaining ring. The polarizers were mounted this way so they would come into contact with each other when used as reflectors. Therefore, the fundamental-mode bandpass feature of the FPI could be measured, even at very high frequency (>1 THz). Careful attention was paid while mounting the polarizers to make sure the metal polarizer strips were on the top surface.

5.1.1. Fabry-Perot measurements at 530 GHz

After all of the individual FPI components were made, the system was assembled for testing. The first step in testing was aligning the FPI polarizers so they were both ~95% reflective, this way the system would have good spectral selectivity and the input signal would resonate in the cavity. To do this alignment, a linearly polarized 100 GHz source (Gunn oscillator) was used, and the polarizers were individually adjusted so that the transmission was ~5%. Then both FPI mirrors were put in the system and spectral measurements began.

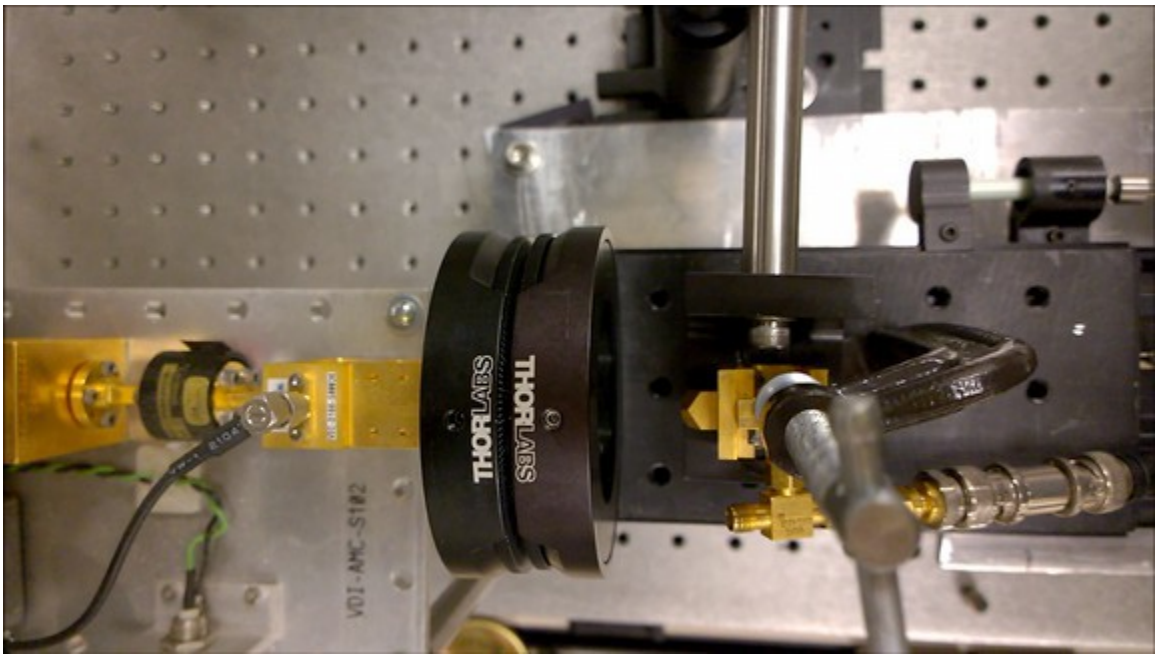

Figure 70: Experimental setup of the polarizing FPI, with the coherent, single wavelength, 530 GHz source.

The first spectral measurements taken with the new polarizing FPI consisted of repeating the 530 GHz scans taken with the wire-mesh based FPI. This experiment would serve as proof that the polarizing FPI design can also discriminate THz frequencies. The experimental setup can be seen in Fig. 70. To match the experiment

performed on the wire mesh FPI the scans were again taken at three different scan times, 0.5, 0.1, and 0.05 seconds. However this time the scan distance was 600 microns, so the resolutions were slightly reduce to 0.2, 1, and 2 μm/sample. Importantly these three resolutions are all still above the previously stated resolution requirement of 2.43 μm/sample, needed to fully resolve the bandpass features if the Q of the FPI is 77.

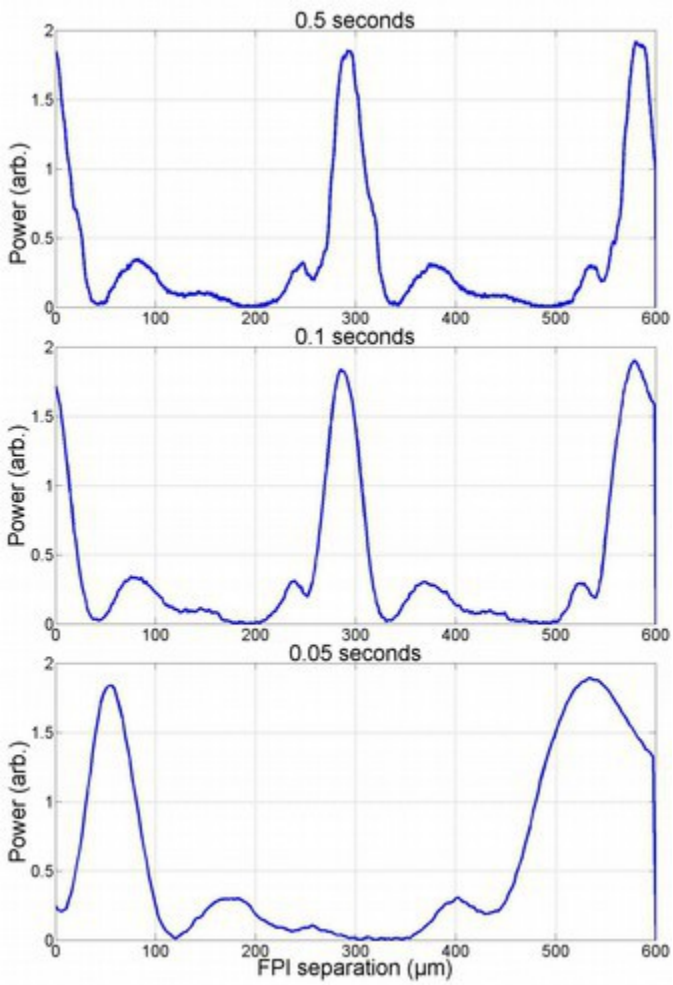

Figure 71: Polarizing FPI scans at 530 GHz. The bandpass modes are again seen here, with the correct spacing of ~283 μm.

The FPI reflectors in this setup are guaranteed to be very flat because of the optically polished, quartz polarizer substrate (however they are not guaranteed to be parallel). Because of this the zeroth order bandpass mode of the FPI could be realized (when the reflectors are in contact). A 600 μm scan distance allowed for the scanning of the zeroth order mode, along with the fundamental bandpass mode and the 2nd mode, which should be centered at ~566 μm. The results of this experiment are shown in Fig. 71 where the bandpass modes are present and located where expected. The first mode is again located at approximately 283 μm, and the separation between the

features is correct as well. The resolution of the bandpass features was quite a bit lower than desired, with a FWHM of ~34 μm, corresponding with a $\Delta f = 64$ GHz and a Q of only ~8.5. However this is simply an alignment issue (the plates weren't perfectly parallel and the source wasn't collimated). As discussed in Chapter III, nonparallel FPI plates and uncollimated input signal can significantly broaden the bandpass features. Nevertheless, the polarizing FPI still displayed the ability to discriminate frequencies with a high pass-band to rejection-band ratio of >10 dB. This result was obtained with a minimum scan rate of 0.1 seconds per 600 μm, as scan time decreased below this limit the results became inaccurate and unreliable. The resolution of these scans could likely be improved with simple collimating optics and mirror re-alignment, at the time of this publication there was not much time was available for optimization. With these results in hand, the FPI was then used to record the spectrum of the extrinsic ErAs:GaAs PC switch.

5.1.2. Fabry-Perot measurements on the 1550 nm extrinsic PC switch

Spectral measurements were performed on the extrinsic PC switches described in chapter II, this test represented the first scans taken with the new tunable THZ FPI spectrum analyzer on a broadband THz source. The experimental setup is shown in Fig 72. The setup will be described from right to left. First the ultra-fast mode-locked-laser is coupled from fiber into free-space. Then the laser beam is modulated using a mechanical chopper and focused on to the PC switch using a 10x microscope objective. At this point the PC switch produces THz power and it is coupled into free-space using a

hyper-hemispherical silicon lens. This is identical to the setup used in chapter II for PC switch power measurements. After the THz power is coupled into free-space, it propagates to the FPI spectrum analyzer. Some signal transmits through the FPI and is then measured using a pyroelectric detector, or a narrow-band zero-bias Schottky Diode detector. Voltage readings are taken from the detector, amplified with a 30 dB gain low-noise amplifier, and measured with a standard lock-in amplifier. Another benefit of the translation stage FPI design is visible in Fig. 72: ample room is available for mounting the detector in the beam path.

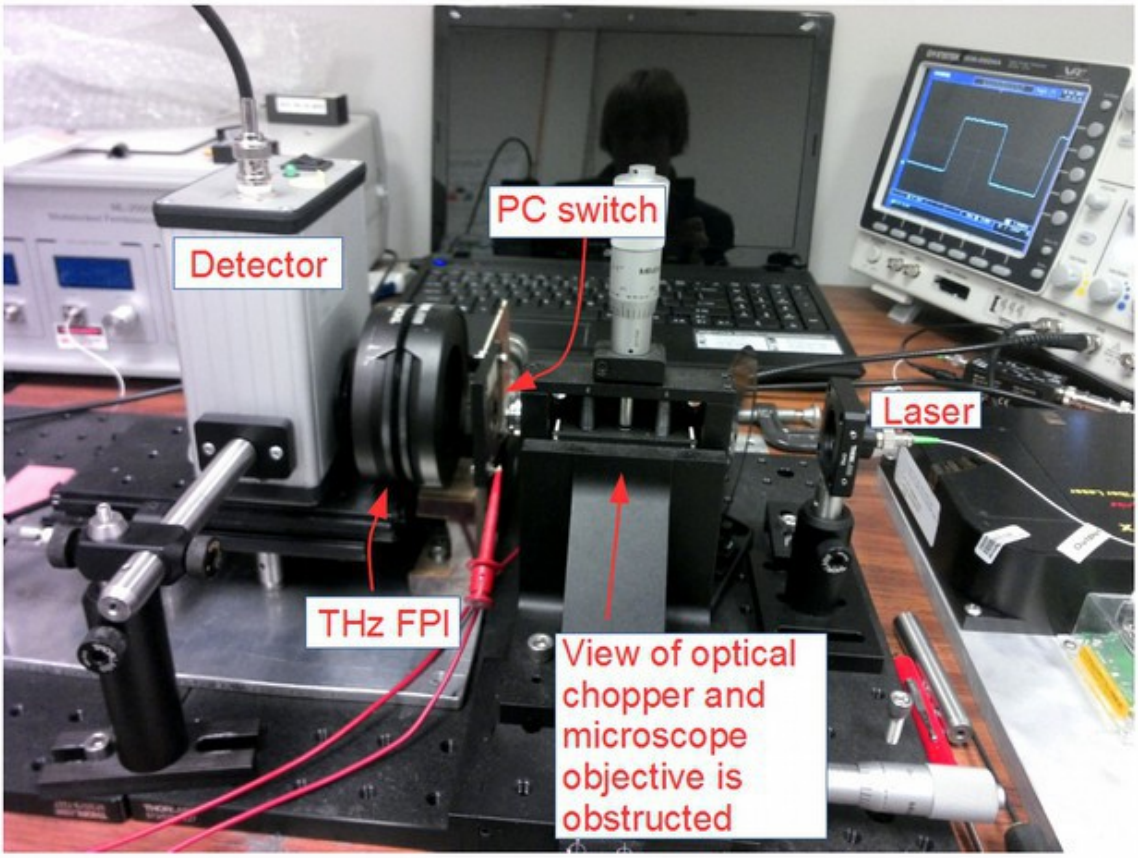

Figure 72: Experimental setup of spectral scans taken with the tunable THz FPI.

Unfortunately the laser used for this experiment was only available for a short time due to a lending agreement with the laser manufacturer, so testing was not extensive.

However, some exciting initial data was still obtained. The results were collected using the same four detectors as in chapter II, a broadband pyroelectric detector, and three zero-bias Schottky diode detectors centered at 100, 415, and 625 GHz. First the 100 GHz Schottky diode detector was used. This makes sense for the first test, because this detector has excellent responsivity (~1500 V/W [102]) over a narrow bandwidth (Fig. 73), so other THz frequencies being emitted by the PC switch should not interfere with the result. Therefore, because the detector bandwidth is much narrower than the PC switch emission bandwidth the bandpass feature should be measured if the FPI is functioning properly. Another factor that makes this detector appropriate for the first test is that the PC switch produces more power at around 100 GHz than it does at higher frequencies, so plenty of signal should be available for measurement.

The results of these first scans are shown in Fig. 74, where it is clear that the FPI spectrum analyzer qualitatively identified the 100 GHz detector responivity spectrum convolved with the power from the PC switch. This is an excellent result and provides solid proof-of-concept for the polarizer-based THz FPI spectrum analyzer. Comparing this result with the detector responsivity curve (Fig. 73) is particularly useful, as the bandwidths of the two curves are quite close. The small valley at 100 GHz in the

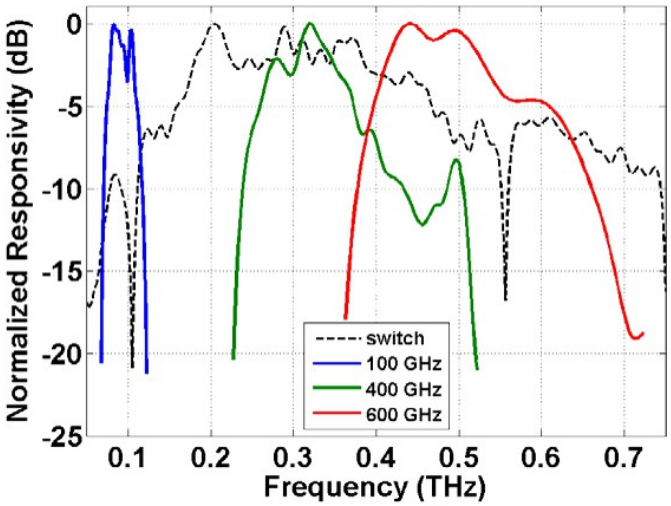

Figure 73: Responsivity curves of the zero-bias Schottky diode detectors.

responsivity curve corresponds to the shoulder in the FPI scan near the same frequency. The pass-band to rejection-band ratio of this measurement was found to be ~7.5 dB and the signal-to-noise ratio was ~39 dB. The scan was taken up to 1 THz, but the lower frequencies were zoomed in for better analysis in Fig. 74(a), and the higher frequencies are shown in Fig. 74(b).

The next scan was taken with the 400 GHz Schottky detector and the results were not as successful (Fig. 75). The fundamental bandpass feature was still measured but the peak is only ~3 dB above the out-of-band signal and was not located at the correct frequency. There are several factors that could have affected the outcome with this detector, and could easily be corrected in future work. The first is that the FPI plates may have become slightly offset from the correct absolute positions. Therefore, the peak feature, which appears to be ~350 GHz, could actually be at the correct frequency. Resetting the FPI zero point before scanning would fix this. Another factor that could improve this result is using a higher resolution. It was not realized at the time of the scan, but the resolution was not set high enough for this frequency, to

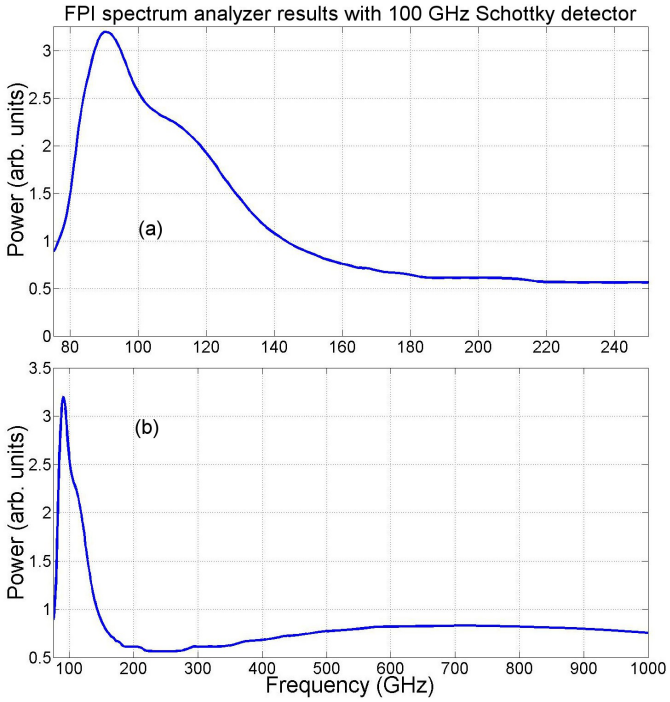

Figure 74: THz FPI spectrum analyzer scan results with a 100 GHz zero-bias Schottky diode detector. The results from this scan were very accurate, the fundamental bandpass mode was accurately measured, with the correct spectral width.

illustrate this the individual data points were also plotted in Fig. 75. Since the current code moves the FPI plate a set distance for each scan (power vs. wavelength is measured), the frequency change between data points increases linearly ($f = c/\lambda$) and high frequencies have lower resolution. Adding more data points would give a smoother, and more accurate curve, and this could easily be corrected with the MATLAB code already written. Another issue is that the reflectance of the polarizers that compose the FPI mirrors is known to change with frequency, and the polarizers were aligned at 100 GHz. However at the orientations the polarizers are in (neither one is S or P) the value of the reflectance change between 100 and 400 GHz is unclear. A solution for this problem would be to calibrate the reflectance change, and use a motorized rotation stage for the polarizer, so that the software could rotate the mirror during the scan and keep the reflectance constant for the entire scan. This is a major design change that is recommended for future work.

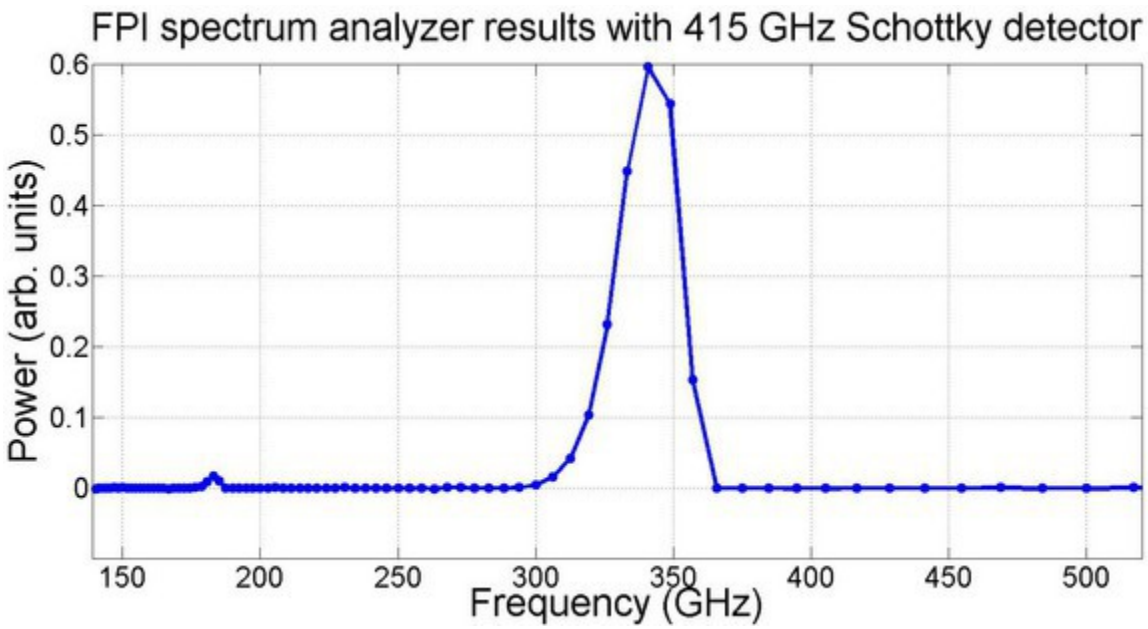

Figure 75: FPI scan results with the 415 GHz Schottky detector. The results were difficult to analyze, as the power was very low. Resolution was also poor and should have been at least double.

For the 600 GHz detector, scans were attempted but they were in the noise floor, likely from the same problems described for the 400 GHz detector. So these scans are not shown here. Another problem that may have made this experiment more difficult is that the laser used to drive the PC switch had lower power than the laser used in chapter II, so the available THz power was well under the level used in Chapter II.

The final scans with the polarizer-based FPI were taken with a broadband pyroelectric detector (Figs. 76,77). This detector is known to have a flat responsivity of ~5000 V/W across the THz spectrum. As shown in Fig. 76 the result from ~80 to 300 GHz was very good, with the 3-dB bandwidth comparing favorably with the result found in chapter II (~350 GHz). Here the 3-dB point is not shown but can be estimated as roughly 330 GHz. This is a gratifying result, especially when reflectance changes are considered. The results from the polarizer testing sections in this chapter show that the

reflectance changes with frequency, but how much it changes in this setup is unclear. If the reflectance of the mirrors increases, then the transmitted power for a broadband source will decrease artificially due to the higher-Q bandpass feature. The results shown here confirm that the polarizer-based FPI spectrum analyzer works, but needs some more development.

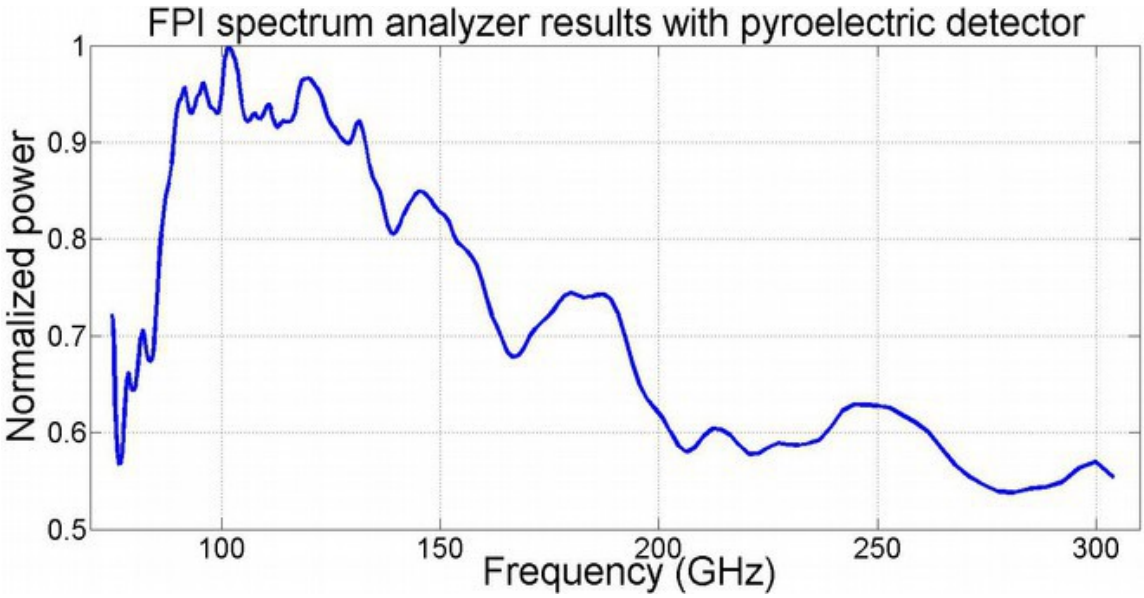

Figure 76: FPI scan with the pyro-electric detector. These results are out to 300 GHz, where the measured spectrum closely resembled the spectrum measured in chapter II.

The scan in Fig. 76 was only shown up to 300 GHz because of a problem encountered at higher frequencies. Above 300 GHz the detected power began to increase, rather than decrease as the THz spectrum must. This happens because wavelengths much longer than the FPI cavity length always experience constructive interference, and therefore high transmission through the FPI. The full scan out to ~1 THz is shown in Fig. 77, the result at high frequency does not mean the FPI was unsuccessful though, because this problem could be solved by developing high-pass filters or combining results from band-limited detectors, like the Schottky diodes

described earlier in this section.

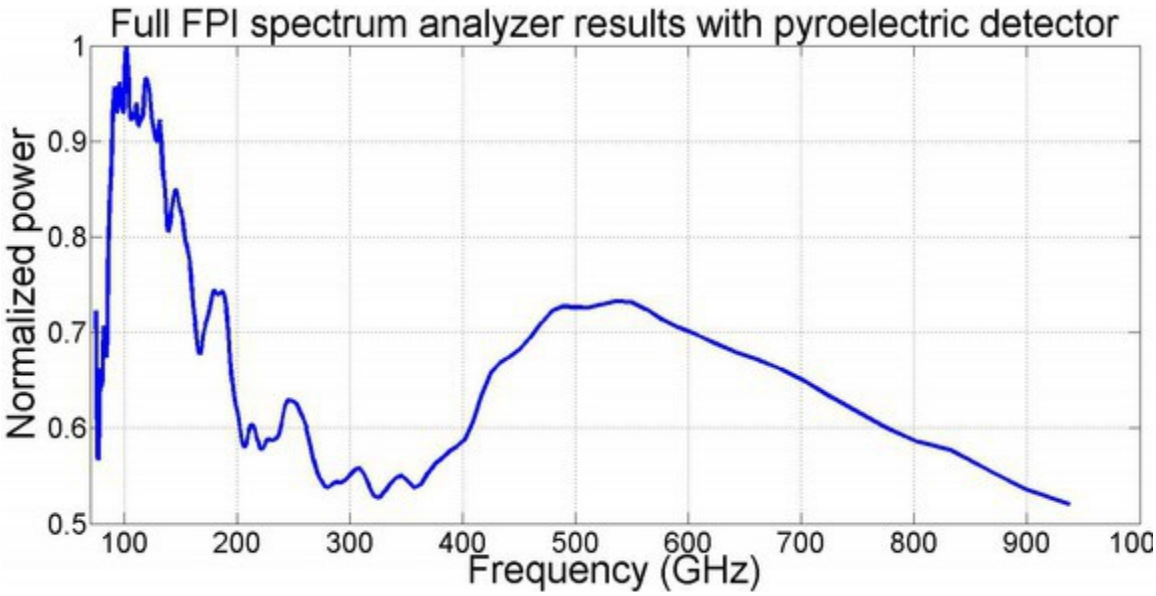

Figure 77: The pyroelectric scan out to 1 THz with the FPI. Here the need for a high-pass filter is evident. Low frequency leak through skews the results at high frequency.

After these tests were completed the laser required to operate the PC switch became unavailable, so no more experiments could be completed. Nonetheless, the results shown here are exciting because they prove that the THz FPI is capable of effectively discriminating and detecting THz frequencies. Some improvement on the system is still needed for future work. One further improvement would be using an input lens to collimate the beam and reduce walk-off losses, and then an output lens to better collect the transmitted power in the detector. In a later development stage, a more expensive linear actuator could be utilized that would provide position information in real time through access to the motor feedback loop. This way, the mirror separation information would be more accurate. In any case, this work represents the first ever demonstration of a polarizer-based FPI used for THz spectrum analysis, thus furthering the capabilities of the THz field and potentially leading to an inexpensive and accurate

new tool that could be used for transmission and reflection spectroscopy. This new THz FPI will be presented to the THz community at IRMMW-THz 2014, pending abstract approval [103].

6. Summary and future direction

This dissertation and the works published during its completion have successfully introduced new and original technology into the THz field. The field of THz spectroscopy is constantly evolving and this work is representative of that. Of particular importance, for practicality reasons, is developing better reflective spectroscopy devices and systems. The new 1550 nm, extrinsic PC switches developed here have been shown to have THz power and bandwidth comparable with current 800 nm driven switches, and will greatly enhance the practicality of THz systems by lowering the cost of components and enabling more compact systems that are easier to setup, because fiber-optic lasers and components can be utilized.

The new Fabry-Perot based spectrum analyzer also represents new possibilities for THz spectroscopy, especially when enhanced with the polarizers developed here. This spectrum analyzer concept is more flexible and less cumbersome than current TDS and photomixing systems. Further development and the use of focusing optics could realistically allow this FPI to be used in stand-off reflective spectroscopy scenarios, where TDS systems can not. The new high FF and EFF polarizer techniques developed in chapter IV have proven to be useful for the FPI spectrum analyzers, but also further the THz field more generally because THz polarizers or SSP enhanced metamaterials are used in many THz labs. The work done here has increased the understanding of how

SSPs can be used, and the polarizers represent a direct improvement of a commonly used component.

In chapter 2 several experiments were conducted to further analyze the ultrafast extrinsic photoconductive effect discovered in ErAs:GaAs, and possibly find ways to improve the performance of this photoconductive mechanism. In this light, several suggestions for future research are given here: (1) The Erbium concentration in the layer should be increased again. 3% Erbium bearing layers have been grown in the past, but this concentration of Er was high enough to negatively affect the crystalline purity of the GaAs. Nevertheless, since the 2% Er layer exhibited a distinct performance increase over a 1% Er layer, another increase should be attempted, such as 2.5%.

(2) The thickness of the ErAs:GaAs layer should be increased. The ErAs:GaAs material has a significantly lower absorption coefficient with 1550 nm photons than with 800 nm photons. Increasing the thickness of the photoconductive layer is an easy way to increase absorption, so this is be worth trying.

(3) Another way to increase 1550 nm absorption is by growing dielectric mirrors in the photoconductive layer. This has been done in the past (seen in [6]) with PC switches driven with 800 nm lasers. At 800 nm it was deemed unnecessary and actually lead to device failure in some cases, because the increased absorption lead to an increase in Joule heating. However, with the significantly lower absorption coefficient of 1550 nm photons this would be less of a problem.

(4) Last, lasers are often not centered at exactly 1550 nm. The experiment done in section 2.2.4 shows an increase in photocurrent as the wavelength decreases below 1550

nm. Therefore a laser centered closer to 1530 nm may perform better.

The discovery made in chapter 2, that the extrinsic photoconductive effect can also be used for photomixing, represents another significant area of research for the future. This is especially true since photomixing spectrometers are not path length dependent, so they might also be suitable for reflective spectroscopy.

Chapter 3 presents the new FPI based spectrum analyzer and several design iterations were presented, culminating in the final design used in Chapter V with high EFF polarizers. The FPI spectrum analyzer could be improved in a number of ways, and would need to be for commercial use. The research on improving the FPI should primarily focus on improving its mechanical operation (better linear motor, adding motorized rotation stages). Another improvement could be adding precisely aligned optics to the system, to focus and collimate more signal into the FPI, thus improving the SNR. For future research, improved THz bandpass filters would be beneficial, for limiting low-frequency transmission through during high-frequency measurements. Some work has already been done of THz bandpass filters, this should be investigated further [101]. In any case, this new spectrum analyzer idea is very promising and has already motivated other research groups to pursue it [84].

The polarizers detailed in chapter IV out-perform commercially available polarizers already, especially in the extinction ratio metric, but there is still room for future research here as well. The easiest and most imminent improvement would be adding anti-reflection (AR) coatings for frequencies of interest. Quarter-wave AR coatings have been added to substrate-based THz components in the past using cheap

polyethylene sheets. This would add virtually nothing to the cost of the polarizer, while improving its performance. An in depth analysis of the polarizer performance in beamsplitter configuration would also be useful future research. Beamsplitters are often important components in many types in interferometers, such as the Martin-Puplett, and polarizers make useful beamsplitters because of the ability to change the transmission/reflection ratio by rotating the polarizer.

Successful reflective spectroscopy systems may be important to the future of THz systems. They would allow for the non-invasive identification of concealed items. This is be especially useful in security applications where chemicals of interest are often hidden on the human body and privacy is a primary concern. In any case, in a realistic scenario items are not carefully packaged in a lab for placement into a transmission spectroscopy system. This work is important because all of the technology presented here, while being useful for transmission spectroscopy systems, is also important for achieving the first practical reflective THz spectroscopy systems.

Appendix A

Additional design 1: Ball-bearing based Fabry-Perot plates with stretched copper mesh mirrors

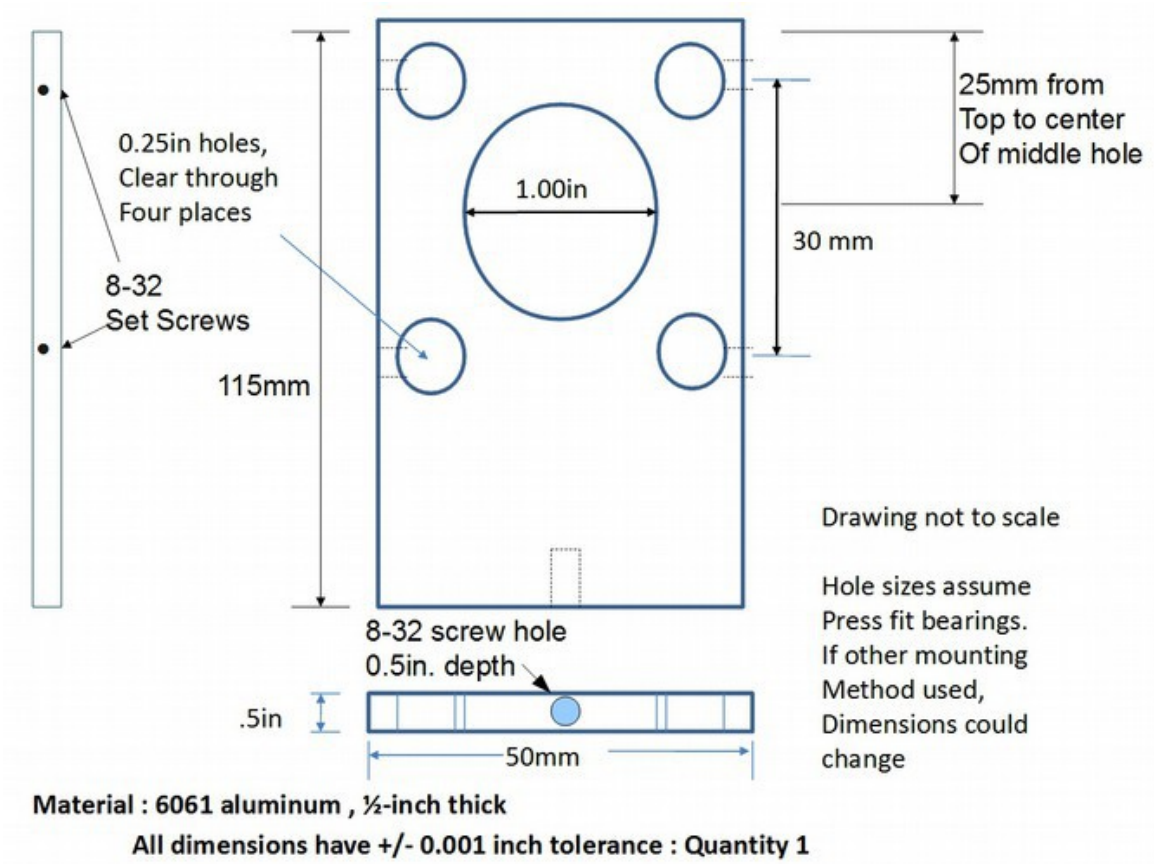

Figure 78: Design layout for new stationary FPI mirror mounting plate. Single peice construction should resist leaning more effectively. The cage rod system is again 30 mm.

A second wire-mesh FPI spectrum analyzer design was made as a response to the large number of design flaws present in the first model. Of particular interest in fixing was the rock/lean issues that plague that mirror plates, and the relative non-flatness of the

wire-mesh-mirrors. Fixing the rocking problem was a three step process: the stationary mirror plate was redesigned to resist leaning, the bushings in the tunable mirror plate were replaced with more precise linear-ball-bearings, and a superior mount was made to hold the motor. For fixing the mirror flatness issues, a new mounting system was developed to hold the wire-mesh on the mirror plates.

The new mirror plate for the stationary mirror was custom machined out of 6061 aluminum, the design is shown in Fig 78. This plate is approximately twice as thick as the previous plate, and about 2.5 inches taller. This was done to increase the structural rigidity to resist leaning. The cage rods were also increased in thickness, from 6 to 6.35 mm (¼ inch). Aside from this, this plate is identical to the previous plate. Set screws were included to lock the cage rods into place and mounting screw was put on the bottom so the plate-height could be adjusted with optical posts or some other mounting system.

The most significant change came in the design of the tunable mirror plate (Fig. 79). This plate was made ¾ inch thick and the holes drilled for the bearings were ½ inch in diameter. The ball-bearings (shown in the bottom right corner of Fig. 79) had a ¼ inch inside (6.35 mm) diameter, the same as the new cage-rod diameter. Therefore the bearings fit tightly on the cage-rods and as a consequence there was no room for the tunable mirror plate to “rock” from rotational forces, thus eliminating that problem. The ball-bearings also reduced sliding friction, so a smaller and more precise linear actuator could be used. The new linear actuator had an even smaller minimum step size (92.5 nm) but was still capable of moving at up to 25 mm/s. As mentioned in the previous section, the maximum movement speed should be at least 0.45 mm/s and the minimum step size

should be under 1 μm, both requirements are easily surpassed by this linear actuator.

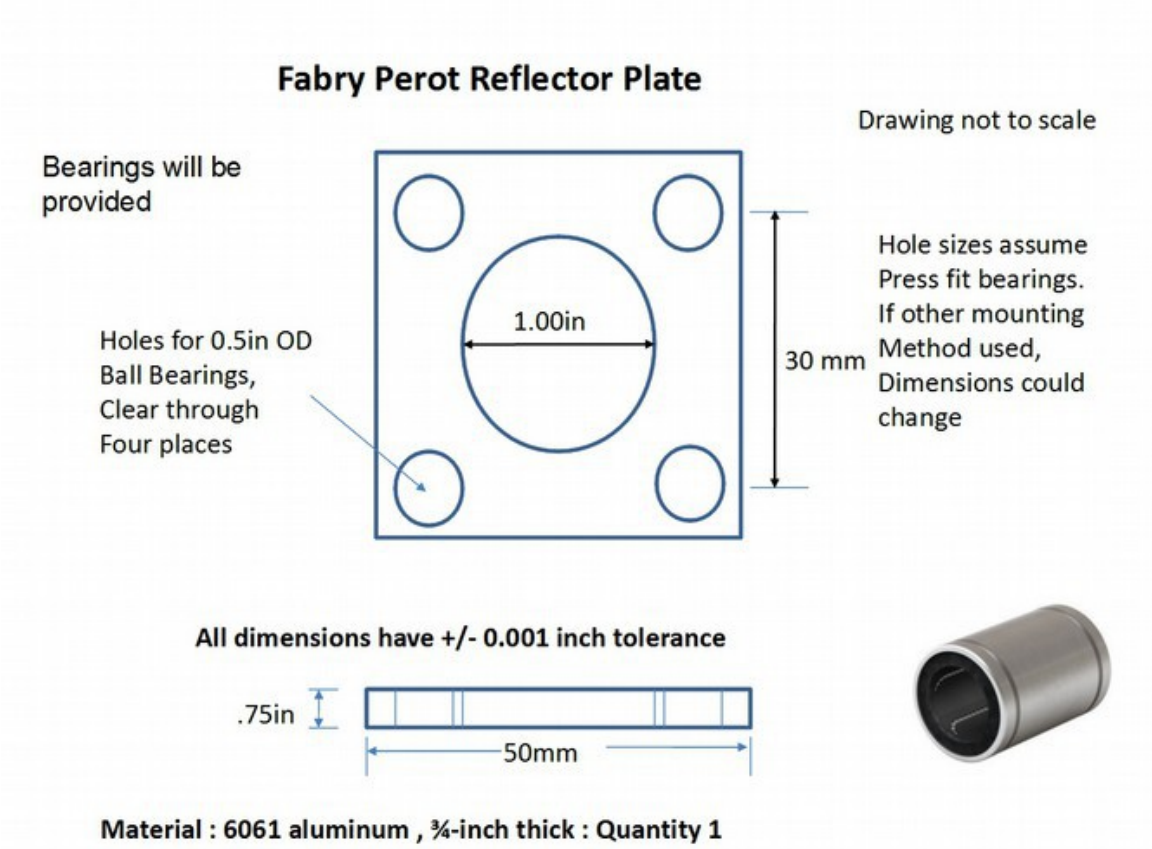

Figure 79: The tunable mirror mounting plate. This plate is thicker and has larger cage-rod holes to accomidate linear-ball-bearings. The ball-bearings help eliminate binding and rocking.

A new mount was also designed and fabricated to hold the linear actuator. Previously, the linear actuator was mounted to an adjustable-height platform so that it's vertical position could be precisely adjusted. This was necessary because of the bushing-binding issues. With the linear-ball-bearing FPI mirror plate this issue was gone, so a simple-but-rigid motor mount was made to hold the actuator and reduce FPI setup time. Fig. 80 shows a comparison of the new FPI system (on the right) to the original model (on the left), and the linear actuator mount is visible here. With this mount the linear

actuator is simply screwed onto the motor mount, which is anchored to the work bench with a standard optical post.

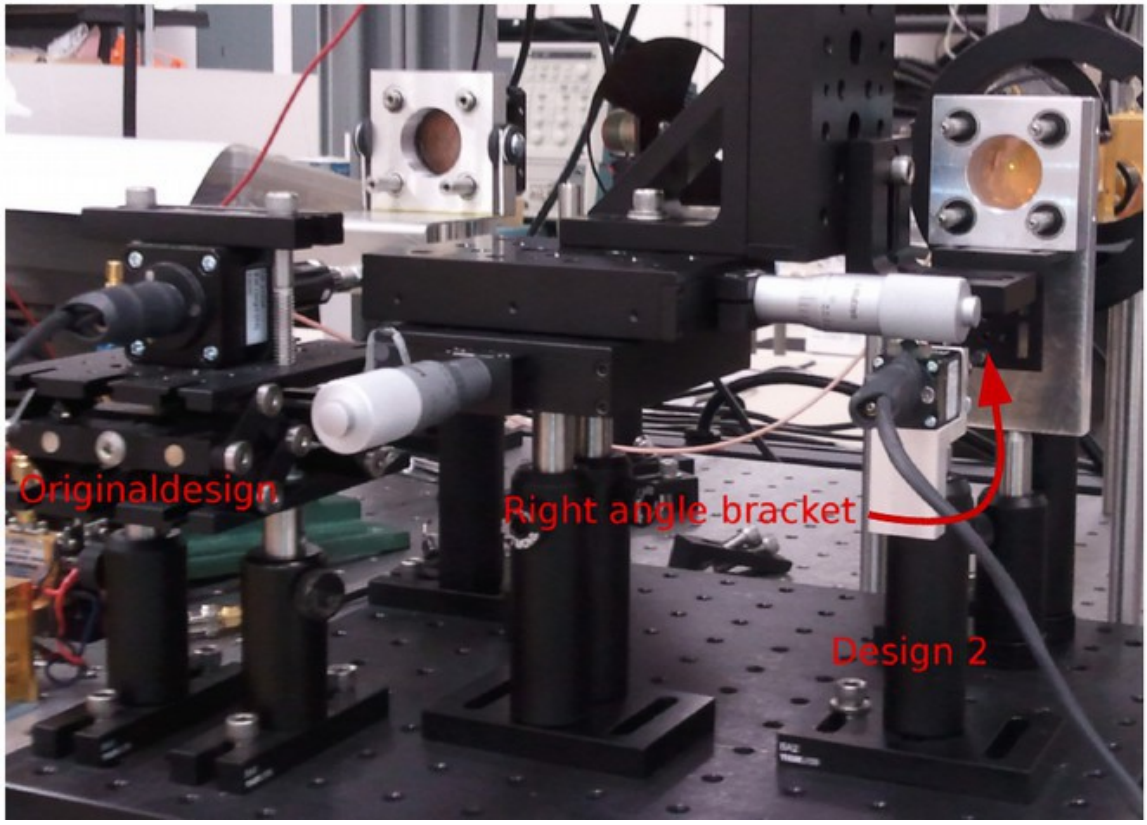

Figure 80: The second FPI design compared side by side with the original. The new design slides more easily on the cage-rods, so a smaller and more precise linear actuator was used. The actuator was coupled to a right-angle bracket on the bottom of the tunable mirror plate; eliminating the bushing related binding problems made this simple coupling strategy possible.

The final design change made in this iteration was changing the way in which the wire-meshes were mounted to the FPI mirror mounting plates. Finding a way to make the wire-meshes flatter was important for the integrity of the FPI scan results and would reduce noise. So instead of simply laying the meshes over the 1 inch diameter hole on the mounting plates, the meshes were stretched over the holes using a tensioner ring. The concept is illustrated graphically in figure 81. In this design, the raised section of the

tensioner right has an outside diameter 1 mm smaller than the inside diameter of the 1 inch mounting plate hole (so the raised section of the ring fit inside the mounting plate hole). The raised section was also 1 mm high. The mesh was woven copper and it did not readily bend at the tight angles necessary to fit between the tensioner ring and the mounting plate hole. So the act of forcing the mesh into this space, by pushing the ring into the hole, stretched it flat. The dimensions of the mesh unit cell weren't altered any, but the mesh-mirror surface was taut and flat. To hold the tensioner ring in place it was then screwed into the mounting plate through the holes seen in the top view of the ring in Fig 81.

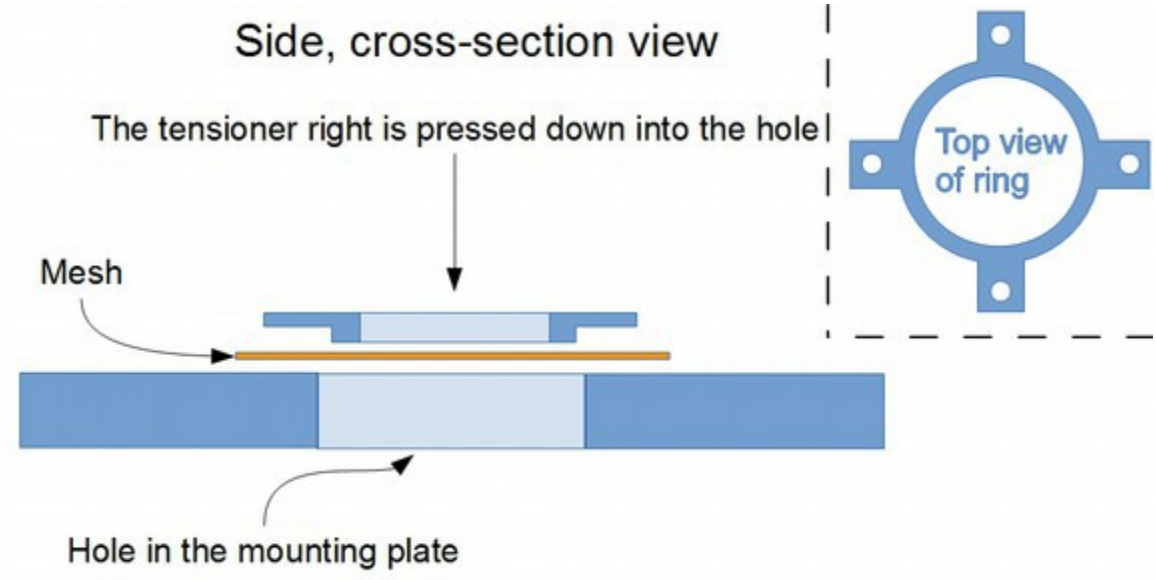

Figure 81: The wire-mesh tensioner ring concept. Pressing this ring into the mounting plate hole would stretch the wire-mesh, and force it to be flat.

Design advances

This FPI THz spectrum analyzer design represented a number of advances over the original model. Most importantly the rocking problem in the first design was completely solved by switching from a bushing-based system to a stronger, linear-ball-bearing based cage-rod sliding system. Eliminating the rocking problem fixed a number of problems. First the mirrors maintained perfect parallel orientation at all times, thus improving the scanning results (less noisy and smaller, more correct line-width). If not very carefully aligned, the old bushing-based system would bind on the cage-rods and cause the motor to slip, in this new design that does not happen. Because there was no binding the linear actuator could be moved to a lower position, farther from the beam patch; this creates more room in the system for other components, such as the detectors. The linear actuator itself was also switched to a smaller, more precise model; once again a possibility because the binding effects were no longer present. Mounting the linear actuator was then simplified because of the new mounting apparatus. The last improvement, but also a significant one, was that the wire-mesh-mirrors were mounted with a new technique that ensured their flatness. The flat mirrors ensures that the FPI has a narrow line-width with less noise in the scan results.

Design shortcomings or problems

The linear-bearing based FPI improved on some significant areas of weakness, but there were still two problems large enough to merit a nearly immediate redesign (shown next). The first problem was minor in comparison to the second, there was still

some leaning present in the stationary FPI mirror mounting plate. Despite the stationary plate being very robust, it was still connected to the workbench with an optical post. The point at which the optical post connected to the mirror plate served as a weak point and the fulcrum for the leaning. So a fix for this was still needed.

The second, and more serious problem came from a fundamental design flaw in the mesh-tensioning system; the tensioner ring pressed the wire mesh into the inside of the mounting plate. So even when the two FPI plates were in contact with each other there was a large gap (~6 mm) between the actual mesh mirrors themselves (Fig. 82). This meant that the fundamental mode band-pass feature could not be measured because the mirrors could not get close enough. Measuring the fundamental mode was an important part of the FPI spectrum analyzer concept, therefore the mesh mounting system needed to be re-evaluated.

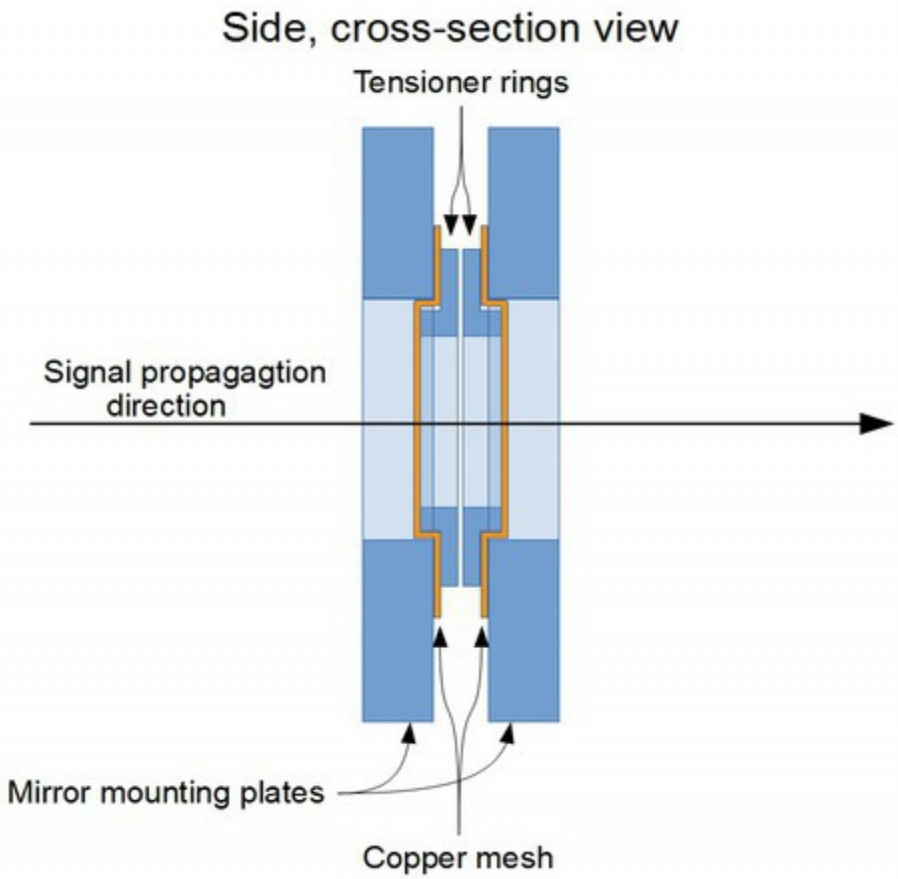

Figure 82: FPI mirror mounting plate and tensioner ring design. With this design, the wire-mesh mirrors can not come together thus not allowing fundamental mode spectroscopy.

Additional design 2: Ball-bearing based Fabry-Perot plates with new mesh tensioner design

The THz FPI was redesigned with two goals: making a wire-mesh mirror mounting system that would keep both meshes very flat, but also allow them to come into contact, thus resolving the fundamental bandpass features of a THz signal, and to stop the stationary FPI mirror plate from "leaning." Aside from these two changes, the rest of the

FPI would remain unchanged. To accomplish the first goal the tensioner ring design was inverted. Instead of having the tensioner ring push the wire-mesh inside of the mirror mounting plate, the mirror mounting plate would push the wire-mesh into and out the other side of the tensioner ring, thus leaving the mesh on the outermost surface of the mounting plate. The design layout of the mounting plate is shown in figure 83. The lip that was on the tensioner ring in the previous design is now on the mounting plate, and the tensioner ring is flat with an inside diameter 1 mm larger than the outside diameter of the lip. This design again proved to create a very flat wire-mesh mirror surface.

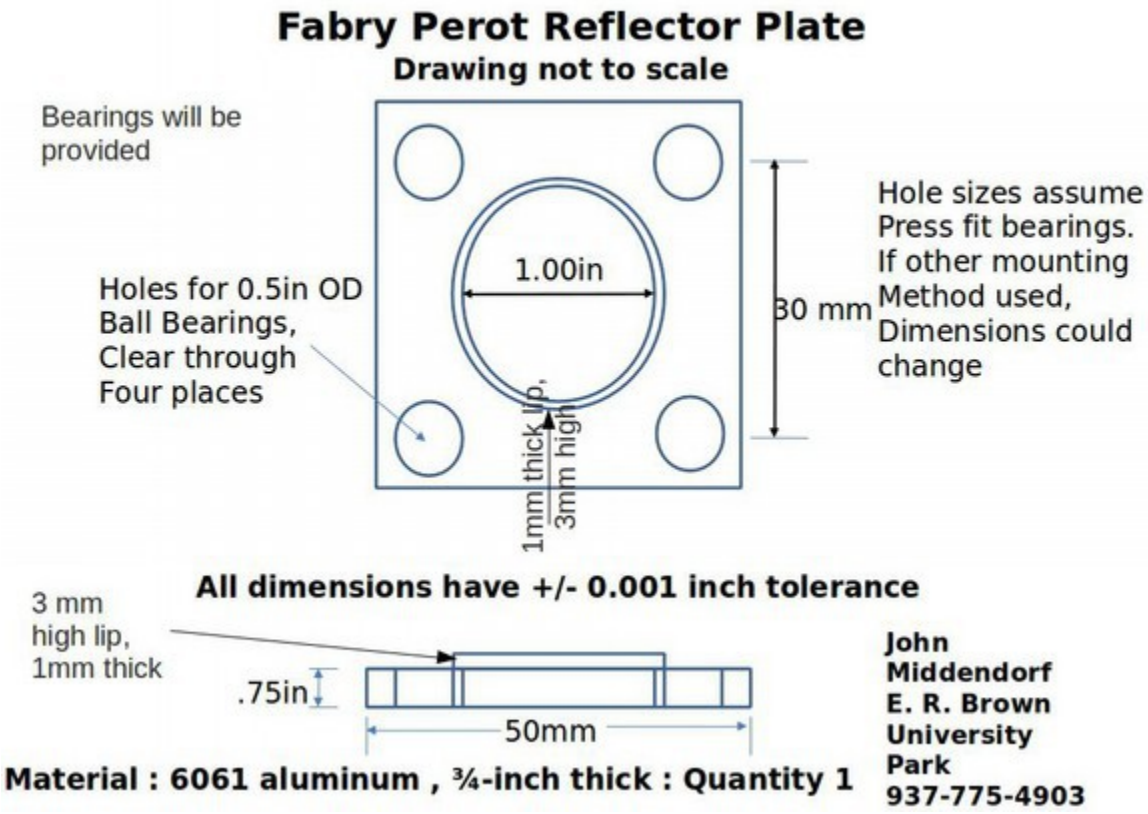

Figure 83: The redesigned FPI mirror mounting plates with the wire-mesh mirror stretched outside of the plate, instead of inside.

The second goal of this design was to eliminate the leaning problem associated

with the stationary FPI mirror plate. To accomplish this lateral bracing was added to the mirror plate using optical posts. Prior to this bracing there was essentially no lateral support in the design except for torsional resistance at the mounting point of the stationary mirror plate. The additional optical posts provided a much needed lateral brace, with a structural member directly opposing lateral movement of the stationary plate itself. Figure 84 shows the new design fully assembled, in this figure both changes are visible. The design of the new tensioner ring can be seen here too, it is simple a flat piece of aluminum that is screwed onto the FPI mirror plates. Other notable items shown here include the front side of the motor mount and the screws that hold the linear actuator to the mount, a better angle for seeing the L-bracket used to transfer force from the linear actuator to the tunable FPI mirror, a cage-rod mounting system for holding small THz Schottky diode detectors, and an example of how a THz lens could be added to the FPI to increase signal power.

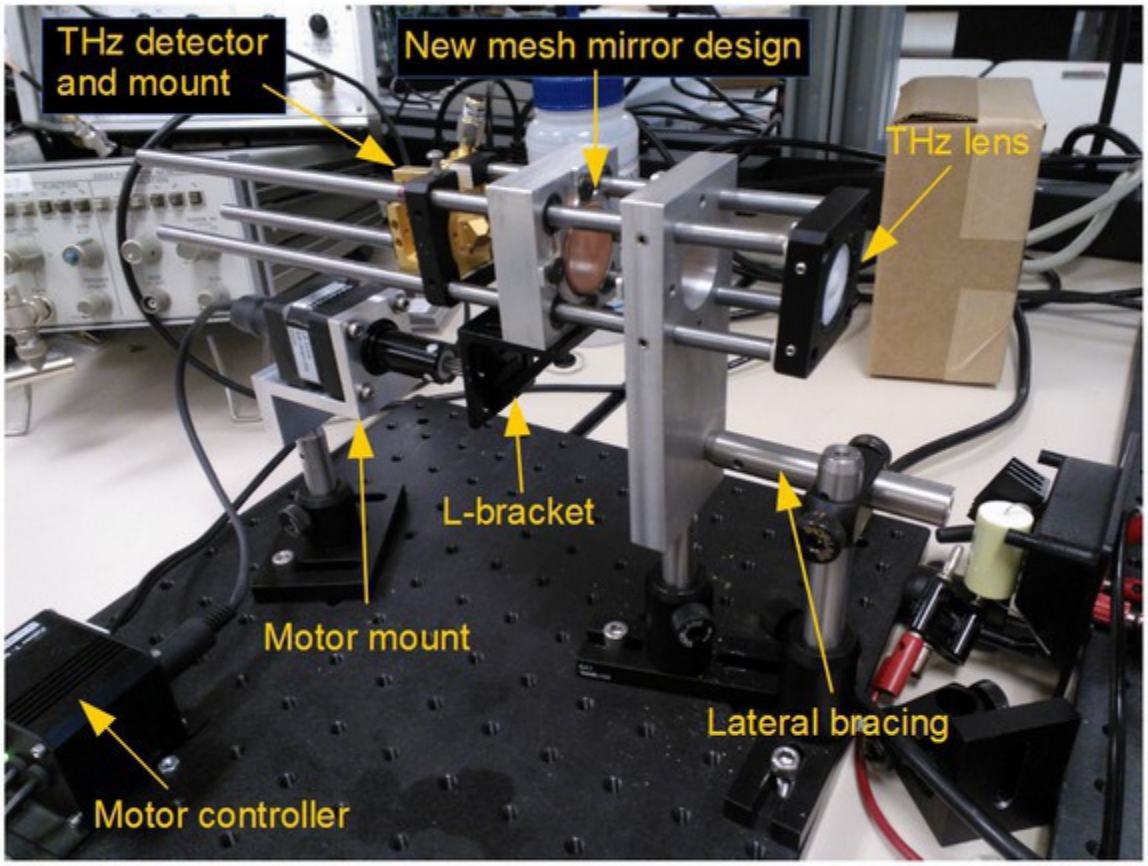

Figure 84: The final wire-mesh mirror, tunable THz FPI design. The new mesh mirror mounting system is shown here, with this design the mirrors can comee fully into contact, thereby allowing fundamental mode spectroscopy. The lateral bracing for the stationary mirror is also shown.

Design advances

Initial testing with this FPI design shows that the problems present in the two previous designs were largely eliminated. This FPI provides steady, consistent scans. The FPI mirrors are very flat and maintain a very parallel orientation, and could come into contact with each other. Additionally, the stationary mirror gained enough lateral bracing to maintain its position without leaning. For the wire-mesh-mirror based FPI this design iteration was the final and best design. However it was not without flaw.

Design shortcomings or problems

Some shortcomings were still present in this design. The linear ball-bearings tend to wear out rather quickly with time, just a few months. This is particularly true when the tunable mirror is removed from the cage-rods, because every time it is put back on the cage-rods, some of the steel balls in the linear-bearings fall out. This appears to be a design flaw with the bearings themselves. Eventually the bearings do not slide well on the cage-rods anymore, this is one reason the larger, more powerful linear actuator is installed in figure 84. Another consequence of the bearings wearing out is that more lateral forces are exerted on the stationary FPI mirror, so if any leaning problems persist, this issue magnifies those problems.

Appendix B

MATLAB code for the THz FPI spectrum analyzer

entryToBits()

```
%%%%%%%%%%%%%%%%%%%%%%%%%%%%%%%%%%%%%%%%%%%%%%%%%%%%%%%%%%%%%%%%%%%%%%%%
% Programmer: John Middendorf
% Organization: Wright State University
%
% Data bit format provided by Zaber Technologies
%
% This function will convert a data entry into 4 data packets needed for
% zaber controllers.
%%%%%%%%%%%%%%%%%%%%%%%%%%%%%%%%%%%%%%%%%%%%%%%%%%%%%%%%%%%%%%%%%%%%%%%%
function [d3 d4 d5 d6] = entryToBits(data)
% Convert negative numbers...
if data<0
    data = 256^4 + data;
end

% d6 is the last bit (data must be larger than 256^3 to have a value
here)
d6 = floor(data / 256^3);
data   = (data) - 256^3 * d6;

% d5 is the next largest bit... d5 = (0:256)*256^2
d5 = floor(data / 256^2);
if d5>256
    d5 = 256;
end

% d4 is the second smallest bit... d4 = (0:256)*256
data   = data - 256^2 * d5;
d4 = floor(data / 256);
if d4>256
    d4 = 256;
end

% d3 is the smallest bit, values are 0:256
d3 = floor(mod(data,256));
if d3>256
    d3 = 256;
end
```

bitsToNumber()

```
%%%%%%%%%%%%%%%%%%%%%%%%%%%%%%%%%%%%%%%%%%%%%%%%%%%%%%%%%%%%%%%%%%%%%%%%%%%%
% This function will convert data bits back into a number
% Written by John Middendorf, Wright State University
%%%%%%%%%%%%%%%%%%%%%%%%%%%%%%%%%%%%%%%%%%%%%%%%%%%%%%%%%%%%%%%%%%%%%%%%%%%%
function [data] = bitsToNumber(d3,d4,d5,d6)

% Just sum the values...
data = (d6*256^3)+(d5*256^2)+(d4*256)+d3;

end
```

slowScan()

```
%%%%%%%%%%%%%%%%%%%%%%%%%%%%%%%%%%%%%%%%%%%%%%%%%%%%%%%%%%%%%%%%%%%%%%%%%%%%

% Programmer: John Middendorf
% Organization: Wright State University
%
% This program will move the Fabry-Perot, and stream voltage readings
%%%%%%%%%%%%%%%%%%%%%%%%%%%%%%%%%%%%%%%%%%%%%%%%%%%%%%%%%%%%%%%%%%%%%%%%%%%%

function [magnitudes] = slowScan(motor,start,time,distance)
% motor == 1 is the NA14D30
% motor == 2 is the NA08B30

%% Initialize the LabJack
ljud_LoadDriver  %%load driver
ljud_Constants   %%constants

[Error ljHandle] = ljud_OpenLabJack(LJ_dtU6,LJ_ctUSB,'1',1);  %%request
handle
[Error] = ljud_ePut(ljHandle, LJ_ioPIN_CONFIGURATION_RESET, 0, 0, 0);  %
% reset
Error_Message(Error)

if motor == 1
    motorStep  = .000381;
    motorSpeed = .00371;
else
    motorStep  = .0000925;
    motorSpeed = .000893;
end

% Variable list
Loops = 1;
num_channels = 1;
ScanRate = 3; % Set scan rate
buffer = 100; % 5 second buffer time
Scans = (ScanRate/1000) * (time*1000)*2;
global final_array;

% Configure for 12-bit resolution
```

```
Error =
ljud_AddRequest(ljHandle,LJ_ioPUT_CONFIG,LJ_chAIN_RESOLUTION,12,0,0);
Error_Message(Error)

% Configure AIN0 with Bipolar ±10 volt range
Error = ljud_AddRequest(ljHandle,LJ_ioPUT_AIN_RANGE,0,LJ_rgBIP10V,0,0);
Error_Message(Error)

% Configure Scan Rate
Error =
ljud_AddRequest(ljHandle,LJ_ioPUT_CONFIG,LJ_chSTREAM_SCAN_FREQUENCY,Scan
Rate,0,0);
Error_Message(Error)

% Give the driver a 5 second buffer (ScanRate * 4 Channels * 5 Seconds)
Error =
ljud_AddRequest(ljHandle,LJ_ioPUT_CONFIG,LJ_chSTREAM_BUFFER_SIZE,ScanRat
e*num_channels*buffer,0,0);
Error_Message(Error)

% Configure reads to retrieve whatever data is available without waiting
Error =
ljud_AddRequest(ljHandle,LJ_ioPUT_CONFIG,LJ_chSTREAM_WAIT_MODE,LJ_swNONE
,0,0);
Error_Message(Error)

% Clear stream channels
Error = ljud_AddRequest(ljHandle,LJ_ioCLEAR_STREAM_CHANNELS,0,0,0,0);
Error_Message(Error)

% Define the scan list as AIN0, AIN1, AIN2, and AIN3
Error = ljud_AddRequest(ljHandle,LJ_ioADD_STREAM_CHANNEL,0,0,0,0);
Error_Message(Error)

% Execute list of above requests
Error = ljud_GoOne(ljHandle);
Error_Message(Error)

%--------------------------------------------------------------------------
---
% Get all results just to check for errors
Error = ljud_GetFirstResult(ljHandle,0,0,0,0,0);
Error_Message (Error)

% Run while loop until Error 1006 is returned to ensure that the device
has
% fully configured its channels before continuing.
while (Error ~= 1006) % 1006 Equates to LJE_NO_MORE_DATA_AVAILABLE
    Error = ljud_GetNextResult(ljHandle,0,0,0,0,0);
    if ((Error ~= 0) && (Error ~= 1006))
        Error_Message (Error)
        break
    end
end
```

```
%% Start Fabry-Perot move operation

%input file name
%filename=input('enter name of file for saving data\n', 's');
%fid = fopen(filename,'r+');

% Get speed, distance, and serial port inputs
speed = distance/time %handles.speed
usb = serial('com11');%handles.usb;
fopen(usb);

[a b c d] = entryToBits(start/motorStep);

fwrite(usb,[0 42 91 59 0 0]);
%fwrite(usb,[0 47 100 0 0 0]);
fwrite(usb,[0 20 a b c d]);
pause(0.5);
fwrite(usb,[0 20 a b c d]);
fread(usb,6);
fread(usb,6);

% Put the speed in terms of steps/second
speed = (speed)/(motorSpeed);

% Ask for position and read data packets until the correct response
 fwrite(usb,[0 60 0 0 0 0]);
 while ans(2) ~= 60
 fread(usb,6)
 end

% Scan movement
[d3 d4 d5 d6] = entryToBits(speed)
fwrite(usb,[0 42 d3 d4 d5 d6]); %write operation for movement speed
pause(0.1);
fread(usb,6)
% Put distance in terms of mm/step...
distance2 = (-distance)/(motorStep);
% This is the oscillation distance
[d3 d4 d5 d6] = entryToBits(distance2(1));
[d7 d8 d9 d0] = entryToBits(-distance2(1));

% dummy vars
a = 1;
test = 0

% DAQ recording parameters
recording_time = distance/(speed*motorSpeed);
DAQ = 130;
timeFinal = 0;
counter = 0;
dis = 0;
finalMag = 0;
magnitudes = 0;
final_array =0;
```

```
while counter<1
count = 0;
fwrite(usb,[0 21 d3 d4 d5 d6]);
%pause(0.0);

%% Start the Stream
Error = ljud_ePut(ljHandle,LJ_ioSTART_STREAM,0,0,0);
Error_Message(Error)
for n = 0:Loops

    % Set the number of scans to read. We will request twice the number
we
    % expect, to make sure we get everything that is available. Note the
array
    % we pass must be sized to hold enough SAMPLES, and the Value we
pass
    % specifies the number of SCANS to read.
    Scans = (ScanRate/1000) * (time*1000)* 2;

    % Initialize an array to store data
    array(Scans*num_channels) = double(0);

    % Wait a little then read however much data is available
    pause (time-(time*.4))

    % Get the Streamed Data. Here the special ljud_eGet_array function
must be used
    % for array handling. The function ljud_eGet_array calls from a
    % different library where the eGet function has been modified to
handle
    % arrays. The difference between the regular ljud_eGet and this
modified
    % ljud_eGet_array is the last input argument data type. In the
regular ljud_eGet it is
    % specified as an int32. In the modified ljud_eGet_array the last
input
    % argument is specified as a doublePtr. This modified function
returns
    % a single column array. If you have streamed from more than one
    % channel the data has to be parsed as in this sample.
    [Error Scans return_array] =
ljud_eGet_array(ljHandle,LJ_ioGET_STREAM_DATA,LJ_chALL_CHANNELS,Scans,ar
ray);
    Error_Message(Error)

    final_array =
horzcat(final_array,return_array(1:Scans*num_channels));

    clear return_array
    clear array

end
counter = counter+1; % early versions of the software used a loop to
```

```
take multiple scans
end
%% Stop the stream
[Error] = ljud_ePut(ljHandle,LJ_ioSTOP_STREAM,0,0,0);
Error_Message(Error)

test;
magnitudes = final_array
times = 0:1/DAQ:recording_time;
dis = (time-0.1).*(speed*motorSpeed);
clear final_array

ans = [0 0];
 fwrite(usb,[0 60 0 0 0 0]);
 while ans(2) ~= 60
 fread(usb,6)
 end

fclose(usb);
delete(usb);
clear usb;
```

oscillate5()
(this name is a historical artifact, a more appropriate name would be fastScan())

```
%%%%%%%%%%%%%%%%%%%%%%%%%%%%%%%%%%%%%%%%%%%%%%%%%%%%%%%%%%%%%%%%%%%%%%%%%%%%%%%%

% Programmer: John Middendorf
% Organization: Wright State University
%
% This program will move the Fabry-Perot, and stream voltage readings
%%%%%%%%%%%%%%%%%%%%%%%%%%%%%%%%%%%%%%%%%%%%%%%%%%%%%%%%%%%%%%%%%%%%%%%%%%%%%%%%

function [magnitudes] = oscillate5(motor,start,time,distance)
% motor == 1 is the NA14D30
% motor == 2 is the NA08B30

%% Initialize the LabJack
ljud_LoadDriver  %%load driver
ljud_Constants   %%constants

[Error ljHandle] = ljud_OpenLabJack(LJ_dtU6,LJ_ctUSB,'1',1);  %%request
handle
[Error] = ljud_ePut(ljHandle, LJ_ioPIN_CONFIGURATION_RESET, 0, 0, 0);  %
% reset
Error_Message(Error)

if motor == 1
    motorStep  = .000381; %in mm
    motorSpeed = .00371;  %in mm/s (minimum speed)
else
    motorStep  = .0000925;
    motorSpeed = .000893;
end
```

```
% Variable list
Loops = 1;
num_channels = 1;
ScanRate = 6000; % Set scan rate
buffer = 1; % 5 second buffer time
Scans = (ScanRate/1000) * (time*1000)*2;
global final_array;

% Configure for 12-bit resolution
Error =
ljud_AddRequest(ljHandle,LJ_ioPUT_CONFIG,LJ_chAIN_RESOLUTION,12,0,0);
Error_Message(Error)

% Configure AIN0 with Bipolar ±10 volt range
Error = ljud_AddRequest(ljHandle,LJ_ioPUT_AIN_RANGE,0,LJ_rgBIP10V,0,0);
Error_Message(Error)

% Configure Scan Rate
Error =
ljud_AddRequest(ljHandle,LJ_ioPUT_CONFIG,LJ_chSTREAM_SCAN_FREQUENCY,Scan
Rate,0,0);
Error_Message(Error)

% Give the driver a 5 second buffer (ScanRate * 4 Channels * 5 Seconds)
Error =
ljud_AddRequest(ljHandle,LJ_ioPUT_CONFIG,LJ_chSTREAM_BUFFER_SIZE,ScanRat
e*num_channels*buffer,0,0);
Error_Message(Error)

% Configure reads to retrieve whatever data is available without waiting
Error =
ljud_AddRequest(ljHandle,LJ_ioPUT_CONFIG,LJ_chSTREAM_WAIT_MODE,LJ_swNONE
,0,0);
Error_Message(Error)

% Clear stream channels
Error = ljud_AddRequest(ljHandle,LJ_ioCLEAR_STREAM_CHANNELS,0,0,0,0);
Error_Message(Error)

% Define the scan list as AIN0, AIN1, AIN2, and AIN3
Error = ljud_AddRequest(ljHandle,LJ_ioADD_STREAM_CHANNEL,0,0,0,0);
Error_Message(Error)

% Execute list of above requests
Error = ljud_GoOne(ljHandle);
Error_Message(Error)

%-------------------------------------------------------------------------
---
% Get all results just to check for errors
Error = ljud_GetFirstResult(ljHandle,0,0,0,0,0);
Error_Message (Error)
```

```
% Run while loop until Error 1006 is returned to ensure that the device
has
% fully configured its channels before continuing.
while (Error ~= 1006) % 1006 Equates to LJE_NO_MORE_DATA_AVAILABLE
    Error = ljud_GetNextResult(ljHandle,0,0,0,0,0);
    if ((Error ~= 0) && (Error ~= 1006))
        Error_Message (Error)
        break
    end
end
%% Start Fabry-Perot move operation

% Get speed, distance, and serial port inputs
%distance = 0.5 %handles.distance
speed = distance/time%2.5 %handles.speed
usb = serial('com11');%handles.usb;
fopen(usb);

[a b c d] = entryToBits(start/motorStep);

fwrite(usb,[0 42 91 59 0 0]);
%fwrite(usb,[0 47 100 0 0 0]);
fwrite(usb,[0 20 a/1.5 b/1.5 c/1.5 d/1.5]);
pause(0.5);
fwrite(usb,[0 20 a/1.5 b/1.5 c/1.5 d/1.5]);
fread(usb,12);
if ans(8) ~= 20
    fread(usb,6);
end

% move to the position... twice.  Sometimes the first command doesn't
work
fwrite(usb,[0 20 a b c d]);
pause(0.5);
fwrite(usb,[0 20 a b c d]);
fread(usb,6);
pause(3);
% Put the speed in terms of steps/second
speed = (speed)/(motorSpeed);

% Ask for position and read data packets until the correct response
 fwrite(usb,[0 60 0 0 0 0]);
 while ans(2) ~= 60
 fread(usb,6)
 end

% Start fast scan movement
[d3 d4 d5 d6] = entryToBits(speed)
fwrite(usb,[0 42 d3 d4 d5 d6]); %write operation for movement speed
pause(0.1);
fread(usb,6)
% Put distance in terms of mm/step...
distance2 = distance/(motorStep);
% This is the oscillation distance
```

```
[d3 d4 d5 d6] = entryToBits(distance2(1));
[d7 d8 d9 d0] = entryToBits(-distance2(1));

% dummy vars
a = 1;
test = 0
% DAQ parameters
recording_time = distance/(speed*motorSpeed);
DAQ = 130;
timeFinal = 0;
counter = 0;
dis = 0;
finalMag = 0;
magnitudes = 0;
final_array =0;

while counter<1
count = 0;
fwrite(usb,[0 21 d3 d4 d5 d6]);
%pause(0.0);

%% Start the Stream
Error = ljud_ePut(ljHandle,LJ_ioSTART_STREAM,0,0,0);
Error_Message(Error)
for n = 0:Loops

    % Set the number of scans to read. We will request twice the number
we
    % expect, to make sure we get everything that is available. Note the
array
    % we pass must be sized to hold enough SAMPLES, and the Value we
pass
    % specifies the number of SCANS to read.
    Scans = (ScanRate/1000) * (time*1000)* 2;

    % Initialize an array to store data
    array(Scans*num_channels) = double(0);

    % Wait a little then read however much data is available
    pause (time-(time*.4))

    % Get the Streamed Data. Here the special ljud_eGet_array function
must be used
    % for array handling. The function ljud_eGet_array calls from a
    % different library where the eGet function has been modified to
handle
    % arrays. The difference between the regular ljud_eGet and this
modified
    % ljud_eGet_array is the last input argument data type. In the
regular ljud_eGet it is
    % specified as an int32. In the modified ljud_eGet_array the last
input
    % argument is specified as a doublePtr. This modified function
returns
```

```
    % a single column array. If you have streamed from more than one
    % channel the data has to be parsed as in this sample.
    [Error Scans return_array] =
ljud_eGet_array(ljHandle,LJ_ioGET_STREAM_DATA,LJ_chALL_CHANNELS,Scans,ar
ray);
    Error_Message(Error)

    final_array =
horzcat(final_array,return_array(1:Scans*num_channels));

    clear return_array
    clear array

end
counter = counter+1; % This loop can be modified to perform multiple
scans
end
%% Stop the stream
[Error] = ljud_ePut(ljHandle,LJ_ioSTOP_STREAM,0,0,0);
Error_Message(Error)

test;
magnitudes = final_array
times = 0:1/DAQ:recording_time;
dis = (time-0.1).*(speed*motorSpeed);

figure;
plot(linspace(0,distance,length(magnitudes)),magnitudes);
ans = [0 0];
 fwrite(usb,[0 60 0 0 0 0]);
 while ans(2) ~= 60
 fread(usb,6)
 end

fclose(usb);
delete(usb);
clear usb;
```

Appendix C

CAD part designs used for the final THz FPI design

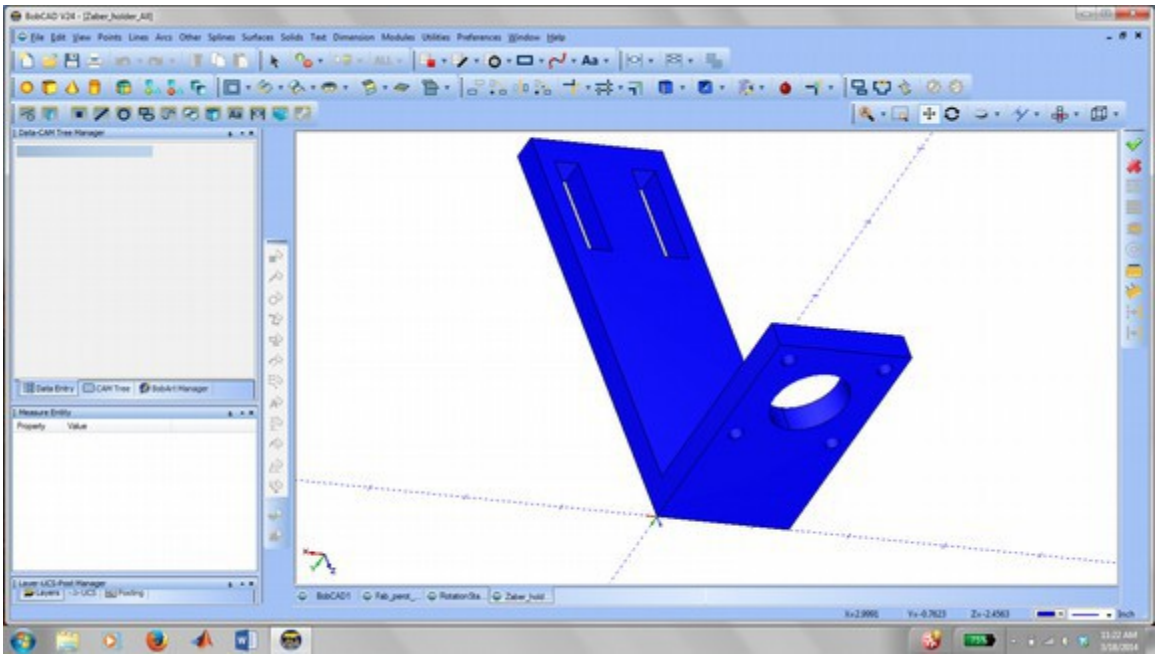

Figure 85: Mount for the Zaber linear actuator. The slots on the long side are where the mount is attached to the base-plate. The holes on the short side are where the linear actuator is mounted.

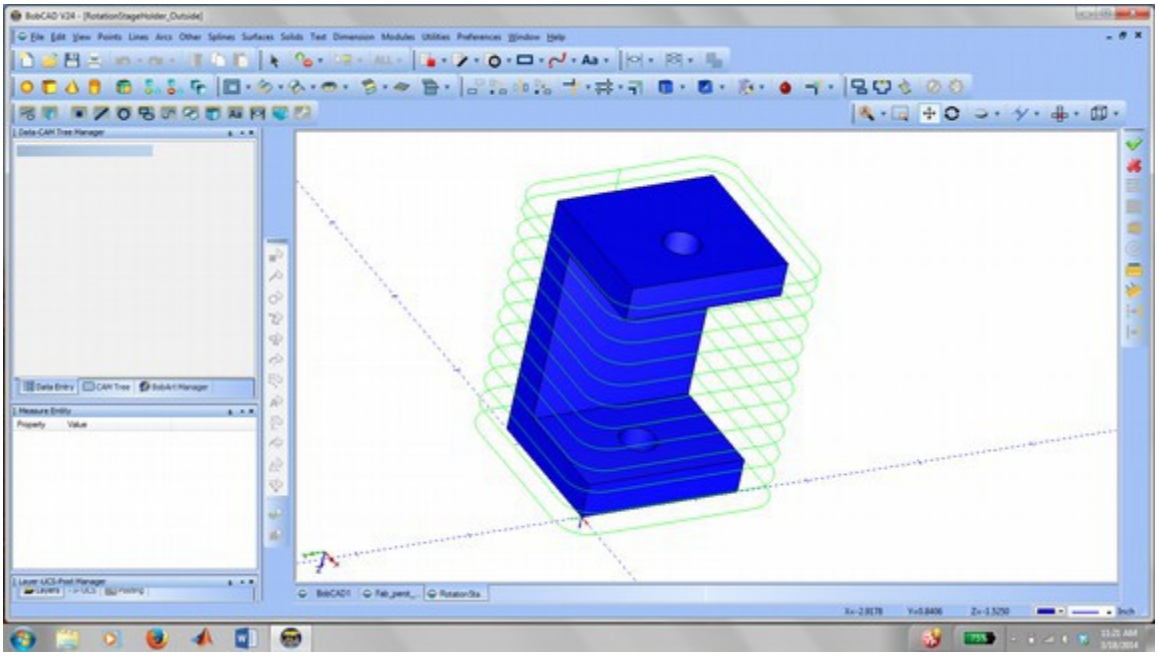

Figure 86: Mount for the stationary FPI mirror (polarizer in a rotation stage). One screw hole is to mount this peice to the baseplate, the other is for mounting the mirror.

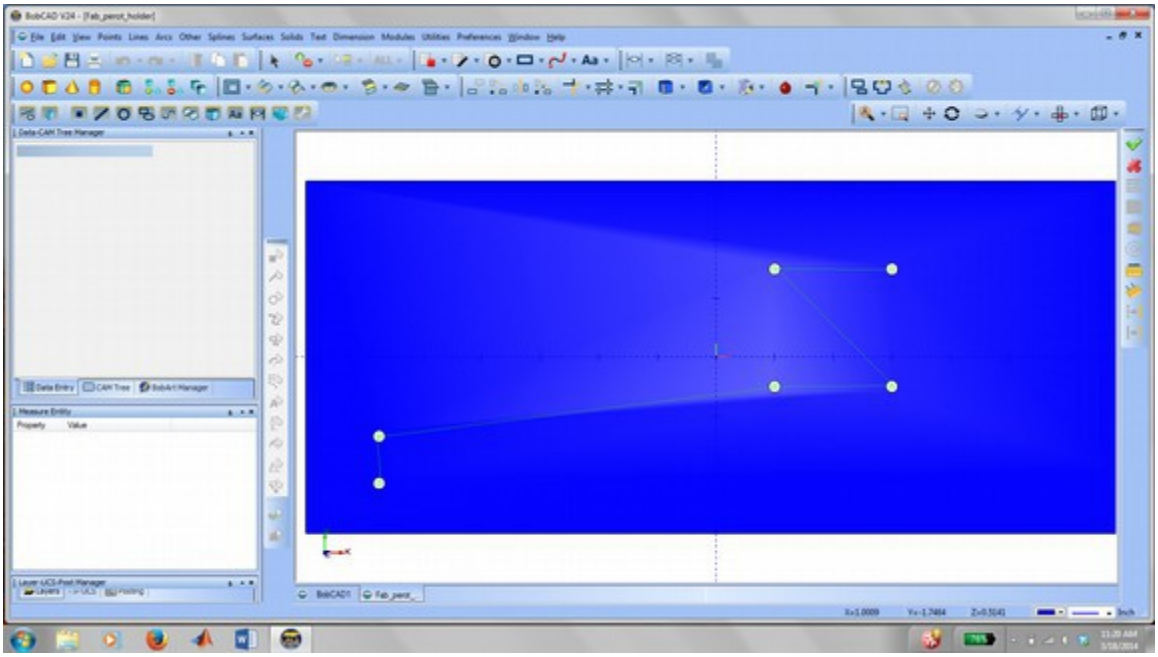

Figure 87: The base-plate. This is simply a metal plate with precisely drilled holes. The FPI parts all mount to this plate, this way the system is easily transportable.

7. References

[1] M. A. Omar, *Elementary Solid State Physics*, 1st ed. New Delhi, India: Pearson, 1999.

[2] B. G. Streetman and S. K. Banerjee, *Solid State Electronic Devices*, Sixth. Upper Saddle River, NJ: Pearson, 2006.

[3] J. F. O'Hara, J. M. O. Zide, a. C. Gossard, a. J. Taylor, and R. D. Averitt, "Enhanced terahertz detection via ErAs:GaAs nanoisland superlattices," *Appl. Phys. Lett.*, vol. 88, no. 25, p. 251119, 2006.

[4] E. R. Brown, *Solid State Engineering*, 1st ed. Wiley - Not yet published, 2014.

[5] J. R. Middendorf and E. R. Brown, "THz generation using extrinsic photoconductivity at 1550 nm," *Opt. Express*, vol. 20, no. 15, pp. 16504–16509, 2012.

[6] Z. D. Taylor, E. R. Brown, J. E. Bjarnason, M. P. Hanson, and a C. Gossard, "Resonant-optical-cavity photoconductive switch with 0.5% conversion efficiency and 1.0 W peak power.," *Opt. Lett.*, vol. 31, no. 11, pp. 1729–31, Jun. 2006.

[7] E. R. Brown, "Advancements in Photomixing and Photoconductive Switching for THz Spectroscopy and Imaging," *SPIE Proc.*, vol. 7938, pp. 793802–793802–16, Feb. 2011.

[8] C. Zhang and K. Mu, "Applications of Terahertz spectroscopy and imaging," *SPIE Proc.*, vol. 7385, no. 10, pp. 738504–738504–8, Jul. 2009.

[9] J. E. Bjarnason, T. L. J. Chan, a. W. M. Lee, M. a. Celis, and E. R. Brown, "Millimeter-wave, terahertz, and mid-infrared transmission through common clothing," *Appl. Phys. Lett.*, vol. 85, no. 4, p. 519, 2004.

[10] W. L. Chan, J. Deibel, and D. M. Mittleman, "Imaging with terahertz radiation," *Reports Prog. Phys.*, vol. 70, no. 8, pp. 1325–1379, Aug. 2007.

[11] C. A. Balanis, *Antenna Theory Analysis and Design*, Third. Hoboken, NJ: John Wiley & Sons, Inc., 2005.

[12] J. B.-Y. Tsui, *Microwave Receivers with Electronic Warfare Applications*. New York: John Wiley & Sons, Inc.

[13] *Electro-Optics Handbook*, 2nd ed. Lancaster, PA: RCA, 1974.

[14] A. E. Seigman, *Lasers*. Mill Valley, Ca: University Science Books, 1986.

[15] D. L. Woolard, R. Brown, M. Pepper, and M. Kemp, "Terahertz Frequency Sensing and Imaging: A Time of Reckoning Future Applications?," *Proc. IEEE*, vol. 93, no. 10, pp. 1722–1743, Oct. 2005.

[16] D. M. Mittleman, M. Gupta, R. Neelamani, R. G. Baraniuk, J. V Rudd, and M. Koch, "Recent advances in terahertz imaging," *Appl. Phys. B*, vol. 1094, pp. 1085–1094, 1999.

[17] D. T. Petkie, C. Casto, F. C. De Lucia, S. R. Murrill, B. Redman, R. L. Espinola, C. C. Franck, E. L. Jacobs, S. T. Griffin, C. E. Halford, J. Reynolds, S. O'Brien, and D. Tofsted, "Active and passive imaging in the THz spectral region: phenomenology, dynamic range, modes, and illumination," *J. Opt. Soc. Am. B*, vol. 25, no. 9, p. 1523, Aug. 2008.

[18] D. Sheen, D. McMakin, and T. Hall, "Active millimeter-wave and sub-millimeter-wave imaging for security applications," *IRMMW*, no. October, pp. 28–31, 2011.

[19] J. A. Zeitler and Y. Shen, "Industrial Applications of Terahertz Imaging," in *Terahertz Spectroscopy and Imaging*, vol. 171, K.-E. Peiponen, A. Zeitler, and M. Kuwata-Gonokami, Eds. Berlin, Heidelberg: Springer Berlin Heidelberg, 2013, pp. 451–489.

[20] D. T. Petkie, I. V. Kemp, C. Benton, C. Boyer, L. Owens, J. a. Deibel, C. D. Stoik, and M. J. Bohn, "Nondestructive terahertz imaging for aerospace applications," in *SPIE proceedings*, 2009, vol. 7485, p. 74850D–74850D–9.

[21] D. Bennett, "Hydration Sensing in Biological Tissues with the Terahertz Band," University of California, Santa Barbara, 2011.

[22] D. B. Bennett, Z. D. Taylor, P. Tewari, R. S. Singh, M. O. Culjat, W. S. Grundfest, D. J. Sassoon, R. D. Johnson, J.-P. Hubschman, and E. R. Brown, "Terahertz sensing in corneal tissues.," *J. Biomed. Opt.*, vol. 16, no. 5, p. 057003, May 2011.

[23] Z. D. Taylor, R. S. Singh, M. O. Culjat, J. Y. Suen, W. S. Grundfest, H. Lee, and E. R. Brown, "Reflective terahertz imaging of porcine skin burns.," *Opt. Lett.*, vol. 33, no. 11, pp. 1258–60, Jun. 2008.

[24] M. Brun, F. Formanek, a Yasuda, M. Sekine, N. Ando, and Y. Eishii, "Terahertz imaging applied to cancer diagnosis.," *Phys. Med. Biol.*, vol. 55, no. 16, pp. 4615–23, Aug. 2010.

[25] S. L. Dexheimer, *Terahertz Spectroscopy: Principles and Applications*. 2007, p. 360.

[26] R. G. Mathew, J. R. Middendorf, E. R. Brown, C. Koneka, J. Wilkinson, O. Esenturkb, E. Heilweilb, and M. Kemp, "Database of all THz Signatures measured on Solids and Liquids in the range 100 GHz to 10 THz," 2011.

[27] E. R. Brown, J. E. Bjarnason, a. M. Fedor, and T. M. Korter, "On the strong and narrow absorption signature in lactose at 0.53 THz," *Appl. Phys. Lett.*, vol. 90, no. 6, p. 061908, 2007.

[28] J. S. Melinger, N. Laman, and D. Grischkowsky, "The underlying terahertz vibrational spectrum of explosives solids," *Appl. Phys. Lett.*, vol. 93, no. 1, p. 011102, 2008.

[29] I. Virginia Diodes, "Millimeter-Wave & THz Systems." [Online]. Available: http://vadiodes.com/index.php?option=com_content&view=article&id=180:systems&catid=21&Itemid=16.

[30] M. squared Lasers, "Firefly-THz," no. 0. p. 766300, 2012.

[31] E. R. Brown, F. W. Smith, and K. a. McIntosh, “Coherent millimeter-wave generation by heterodyne conversion in low-temperature-grown GaAs photoconductors,” *J. Appl. Phys.*, vol. 73, no. 3, p. 1480, 1993.

[32] D. Auston, K. Cheung, J. Valdmanis, and D. Kleinman, “Cherenkov Radiation from Femtosecond Optical Pulses in Electro-Optic Media,” *Phys. Rev. Lett.*, vol. 53, no. 16, pp. 1555–1558, Oct. 1984.

[33] A. Johnson and D. Auston, “Microwave switching by picosecond photoconductivity,” *IEEE J. Quantum Electron.*, vol. 11, no. 6, pp. 283–287, Jun. 1975.

[34] M. C. Young, H. N. Prinson, R. J. Blum, and B. R. Tripp, “A Nanosecond X-Band Switch,” *IEEE Proc. Lett.*, vol. MIL, 1967.

[35] G. Tempea, a Scrinzi, F. Krausz, and T. Brabec, “Comment on ‘Observation of attosecond light localization in higher order harmonic generation’.,” *Phys. Rev. Lett.*, vol. 87, no. 10, p. 109401, Sep. 2001.

[36] M. Systems, “T-Light datasheet.” Menlo, pp. 0–1.

[37] 1 E. R. Brown, 1 A. W. M. Lee, 2 B. S. Navi, and J. E. Bjarnason1, “Characterization of a Planar Self-Complimentary Square-Sprial Antenna in the THz Region,” *Microw. Opt. Technol. Lett.*, vol. 48, no. 3, pp. 524–529, 2006.

[38] E. R. Brown, K. a. McIntosh, K. B. Nichols, and C. L. Dennis, “Photomixing up to 3.8 THz in low-temperature-grown GaAs,” *Appl. Phys. Lett.*, vol. 66, no. 3, p. 285, 1995.

[39] C. W. Berry, M. Unlu, M. R. Hashemi, M. Jarrahi, C. Science, and A. Arbor, “Use of Plasmonic Gratings for Enhancing the Quantum Efficiency of Photoconductive Terahertz Sources *,” pp. 5–6, 2012.

[40] Polaronyx, “Price List of Standard Products,” no. 408. Polaronyx, p. 95131, 2014.

[41] J. L. Hudgins, S. Member, G. S. Simin, E. Santi, and M. A. Khan, “An Assessment of Wide Bandgap Semiconductors for Power Devices,” *IEEE Trans. power Electron.*, vol. 18, no. 3, pp. 907–914, 2003.

[42] M. squared Lasers, “Sprite-XT.” 2012.

[43] P. M. Downey and B. Schwartz, “Picosecond photoresponse in 3He+ bombarded InP photoconductors,” *Appl. Phys. Lett.*, vol. 44, no. 2, p. 207, 1984.

[44] A. R. Frankel, Michael Y., Whitaker, John F., Mourou, Gerard A., Smith, Frank W., Calawa, “High-Voltage Picosecond Photoconductor Switch Based on Low-Temperature-Grown GaAs,” *IEEE Trans. Electron Devices*, vol. 37, no. 12, pp. 2493–2498, 1990.

[45] K. E. Singer, P. Rutter, a. R. Peaker, and a. C. Wright, “Self-organizing growth of erbium arsenide quantum dots and wires in gallium arsenide by molecular beam epitaxy,” *Appl. Phys. Lett.*, vol. 64, no. 6, p. 707, 1994.

[46] I. Poole, K. E. Singer, a. R. Peaker, and a. C. Wright, “Growth and structural characterization of molecular beam epitaxial erbium-doped GaAs,” *J. Cryst. Growth*, vol. 121, no. 1–2, pp. 121–131, Jun. 1992.

[47] J. E. Bjarnason, T. L. J. Chan, a. W. M. Lee, E. R. Brown, D. C. Driscoll, M. Hanson, a. C. Gossard, and R. E. Muller, “ErAs:GaAs photomixer with two-decade tunability and 12 μW peak output power,” *Appl. Phys. Lett.*, vol. 85, no. 18, p. 3983, 2004.

[48] A. Takazato, M. Kamakura, T. Matsui, J. Kitagawa, and Y. Kadoya, “Terahertz wave emission and detection using photoconductive antennas made on low-temperature-grown InGaAs with 1.56 μm pulse excitation,” *Appl. Phys. Lett.*, vol. 91, no. 1, p. 011102, 2007.

[49] C. Carmody, H. H. Tan, C. Jagadish, A. Gaarder, and S. Marcinkevičius, “Ion-implanted In0.53Ga0.47As for ultrafast optoelectronic applications,” *Appl. Phys. Lett.*, vol. 82, no. 22, p. 3913, 2003.

[50] D. C. Driscoll, M. P. Hanson, a. C. Gossard, and E. R. Brown, “Ultrafast photoresponse at 1.55 μm in InGaAs with embedded semimetallic ErAs nanoparticles,” *Appl. Phys. Lett.*, vol. 86, no. 5, p. 051908, 2005.

[51] N. Chimot, J. Mangeney, L. Joulaud, P. Crozat, H. Bernas, K. Blary, and J. F. Lampin, “Terahertz radiation from heavy-ion-irradiated In0.53Ga0.47As photoconductive antenna excited at 1.55 μm,” *Appl. Phys. Lett.*, vol. 87, no. 19, p. 193510, 2005.

[52] B. Sartorius, H. Roehle, H. Künzel, J. Böttcher, M. Schlak, D. Stanze, H. Venghaus, and M. Schell, “operating at 1 . 5 μm telecom wavelengths,” vol. 16, no. 13, pp. 9565–9570, 2008.

[53] A. Fekecs, M. Bernier, D. Morris, M. Chicoine, F. Schiettekatte, P. Charette, and R. Arès, “Fabrication of high resistivity cold-implanted InGaAsP photoconductors for efficient pulsed terahertz devices,” *Opt. Mater. Express*, vol. 1, no. 7, p. 1165, Oct. 2011.

[54] T. Gobel, D. Stanze, R. J. B. Dietz, B. Globisch, H. Roehle, and M. Schell, “1.5μm cw THz photomixing system with 105 dB signal-to-noise ratio,” *2013 38th Int. Conf. Infrared, Millimeter, Terahertz Waves*, pp. 1–2, Sep. 2013.

[55] J. Yuan, W. Xie, H. Liu, J. Liu, and H. Li, “High-Power Semi-Insulating GaAs Photoconductive Semiconductor Switch Employing Extrinsic Photoconductivity,” *IEEE Trans. Plasma Sci.*, vol. 37, no. 10, pp. 1959–1963, 2009.

[56] L. E. Kingsley, “A Study of Picosecond , High-Voltage Photoconductive Switching Using Electro-Optic Diagnostics and Conputer-Aided,” University of Rochester, 1991.

[57] H. Erlig, S. Wang, T. Azfar, A. Udupa, H. R. Fetterman, and D. C. Streit, “LT-GaAs detector with 451 fs response at 1.55-μm via two-photon absorption,” *Electron. Lett.*, vol. 35, no. 2, pp. 173–174, 1999.

[58] S. Adachi, *Properties of Group-IV, III-V, and II-VI Semiconductors*, 1st ed. Wiley, 2005, pp. 309–311.

[59] S. Jayaraman, “Observation of Two-Photon Conductivity in GaAs with Nanosecond and Picosecond Light Pulses,” *Appl. Phys. Lett.*, vol. 20, no. 10, p. 392, 1972.

[60] E. R. Brown, A. Bacher, D. Driscoll, M. Hanson, C. Kadow, and A. Gossard, “Evidence for a Strong Surface-Plasmon Resonance on ErAs Nanoparticles in GaAs,” *Phys. Rev. Lett.*, vol. 90, no. 7, p. 077403, Feb. 2003.

[61] D. T. Tongue and D. E. R. Brown, “Private correspondance.” Zomega Terahertz Corp., 15 Tech Valley Dr., Suite 102, East Greenbush, NY 12061, 2011.

[62] J. R. Middendorf and E. R. Brown, “Extrinsic photoconductivity at 1550 nm and 1030 nm for THz Generation,” *2012 37th Int. Conf. Infrared, Millimeter, Terahertz Waves*, vol. 2, Sep. 2012.

[63] J. R. Middendorf and E. R. Brown, “The effect of Er fraction on THz power generated by extrinsic photoconductive in ErAs:GaAs switches driven at 1550,” *IRMMW Proc.*, 2013.

[64] J. R. Middendorf and E. R. Brown, “A study of ultrafast extrinsic photoconductivity vs wavelength in ErAs:GaAs photoconductive switches,” *2013 38th Int. Conf. Infrared, Millimeter, Terahertz Waves*, Sep. 2013.

[65] J. W. Goodman, *Introduction to Fourier Optics*, 3rd ed. Englewood, CO: Roberts & Company, 2005.

[66] M. Systems, “THz Time Domain Solutions,” 2014. [Online]. Available: http://www.menlosystems.com/index.php/products/?families=78.

[67] TeraView, “Terahertz Equipment for Imaging and Spectroscopy.” [Online]. Available: http://www.teraview.com/products/index.html.

[68] P. R. Trebino, “Optics - Interference.” pp. 13–17, 2013.

[69] “THz Detectors,” 2014. [Online]. Available: https://www.gentec-eo.com/products/thz-detectors.

[70] J. Middendorf and E. Brown, “High speed THz spectroscopy using fast scanning Fabry-Perot,” in *IRMMW*, 2011.

[71] D. J. Griffiths, *Introduction to Electrodynamics*, 3rd ed., vol. 73. Upper Saddle River, NJ: Pearson, 2005.

[72] M. Exter, C. Fattinger, and D. Grischkowsky, “Terahertz time-domain spectroscopy of water vapor.,” *Opt. Lett.*, vol. 14, no. 20, pp. 1128–30, Oct. 1989.

[73] Z. T. Inc., “Linear Slides, Linear Actuators, Stepper Motor Controllers,” 2014. .

[74] K. D. Moller, *Optics*, Second. New York, NY: Springer, 2007.

[75] L. Corp., “LabJack U6,” 2014. [Online]. Available: http://labjack.com/u6.

[76] G. Hernandez, *Fabry-Perot Interferometers*. Cambridge: Cambridge University

Press, 1986, pp. 23–31.

[77] Z. T. Inc., “software/MATLAB,” 2014. [Online]. Available: http://www.zaber.com/wiki/Software/MATLAB.

[78] A. V Oppenheim, R. W. Schafer, and J. R. Buck, *Discrete Time Signal Processing*, 3rd ed., vol. 1999. Upper Saddle River, NJ: Pearson, 1999, p. 870.

[79] M. Systems, “Menlo Tera k15.” pp. 1–2, 2014.

[80] P. Y. Han, M. Tani, M. Usami, S. Kono, R. Kersting, and X.-C. Zhang, “A direct comparison between terahertz time-domain spectroscopy and far-infrared Fourier transform spectroscopy,” *J. Appl. Phys.*, vol. 89, no. 4, p. 2357, 2001.

[81] D. Faklis and G. M. Morris, “Spectral properties of multiorder diffractive lenses.,” *Appl. Opt.*, vol. 34, no. 14, pp. 2462–2468, 1995.

[82] A. Brückner, R. Leitel, A. Oberdörster, P. Dannberg, F. Wippermann, and A. Bräuer, “Multi-aperture optics for wafer-level cameras,” *J. Micro/Nanolithography, MEMS MOEMS*, vol. 10, no. 4, p. 043010, 2011.

[83] J. R. Middendorf, D. LeMaster, M. Zarepour, and E. R. Brown, “Design of Multi-order Diffractive THz Lenses,” in *IRMMW*, 2012.

[84] I. a. Tzibizov, A. K. Kaveev, G. I. Kropotov, D. I. Tsypishka, A. I. Zhdanov, and A. a. Ivanov, “Novel conception of the terahertz-range spectrometer based on Fabry-Perot interferometer,” *2013 38th Int. Conf. Infrared, Millimeter, Terahertz Waves*, Sep. 2013.

[85] M. Instruments, “Polarizer datasheet.” 2014.

[86] Millitech, “Polarizer datasheet,” no. 413. 2014.

[87] Specac, “Free Standing Wire Grids.” 2014.

[88] L. Martín-Moreno, F. J. García-Vidal, H. J. Lezec, K. M. Pellerin, T. Thio, J. B. Pendry, and T. W. Ebbesen, “Extraordinary optical transmission through subwavelength hole arrays.,” *Phys. Rev. Lett.*, vol. 86, no. 6, pp. 1114–7, Feb. 2001.

[89] K. Shiraishi, S. Member, and S. Oyama, “A Polarizer Using Thin Metallic-Film Subwavelength Grating for Infrared to Terahertz Region,” *J. Light. Technol.*, vol. 29, no. 5, pp. 670–676, 2011.

[90] L. Y. Deng, J. H. Teng, L. Zhang, Q. Y. Wu, H. Liu, X. H. Zhang, and S. J. Chua, “Extremely high extinction ratio terahertz broadband polarizer using bilayer subwavelength metal wire-grid structure,” *Appl. Phys. Lett.*, vol. 101, no. 1, p. 011101, 2012.

[91] N. Yu, Q. J. Wang, M. a Kats, J. a Fan, S. P. Khanna, L. Li, a G. Davies, E. H. Linfield, and F. Capasso, “Designer spoof surface plasmon structures collimate terahertz laser beams.,” *Nat. Mater.*, vol. 9, no. 9, pp. 730–5, Sep. 2010.

[92] I. Yamada, K. Takano, M. Hangyo, M. Saito, and W. Watanabe, “Terahertz wire-grid polarizers with micrometer-pitch Al gratings.,” *Opt. Lett.*, vol. 34, no. 3, pp. 274–6, Feb. 2009.

[93] J. Homola, “Surface plasmon resonance sensors for detection of chemical and biological species.,” *Chem. Rev.*, vol. 108, no. 2, pp. 462–93, Feb. 2008.

[94] J. S. Cetnar, J. R. Middendorf, and E. R. Brown, “Extraordinary optical transmission and extinction in a Terahertz wire-grid polarizer,” *Appl. Phys. Lett.*, vol. 100, no. 23, p. 231912, 2012.

[95] H. R. Philipp, “Silicon Dioxide (SiO2), Type alpha (Crystalline),” in *Handbook of Optical Constants of Solids*, E. D. Palik, Ed. Orlando, Fl: Academic Press Inc., 1985, pp. 746–747.

[96] R. D. M. Company, “Thin film evaporation source reference,” 2014. [Online]. Available: http://www.rdmathis.com/PDF/Thin-Film-Evaporation-Source-Ref-Guide-watermark.pdf.

[97] J. T. Baker, “Aluminum Etch 16-1-1-2 CMOS,” 2014. [Online]. Available: http://app.avantormaterials.com/DistributorRedirect/DistributorRedirect.aspx?a=avantor&b=B&c=5427&d=s.

[98] J. S. Cetnar, J. R. Middendorf, and E. R. Brown, “Effective Fill-Factor Design Results in Extraordinary Optical Transmission in a THz Wire-Grid Polarizer,” in *IRMMW proceedings*, 2013.

[99] J. R. Middendorf, J. S. Cetnar, S. Member, J. Owsley, and E. R. Brown, “High Fill-Factor Substrate-Based Wire-Grid Polarizers with High Extinction Ratios,” *IEEE Trans.*, 2014.

[100] R. M. Hendrix, J. R. Middendorf, J. S. Cetnar, J. A. Deibel, and E. R. Brown, “High Fill-Factor Substrate-Based Wire-Grid Polarizers with High Extinction Ratios,” in *IRMMW-THz*, 2014.

[101] M. Lu, W. Li, and E. R. Brown, “High-Order THz Bandpass Filters Achieved by Multilayer Complementary Metamaterial Structures,” in *IRMMW*, 2010.

[102] S. Labs, “DW-2 Broadband Detector,” vol. 10, no. 805. 2011.

[103] J. R. Middendorf and E. R. Brown, “Fast-Scanning Fabry-Perot Spectrum Analyzer with Continuously Tunable Resolution,” in *IRMMW-THz*, 2014, vol. 20, no. 15.